การจำลองแบบความต่างศักย์ตกคร่อมรอยร้าวในชิ้นงาน ด้วยระเบียบวิธีไฟไนต์วอลุ่ม 2 มิติ

นายนิอัสรี เจ๊ะปูเต๊ะ

วิทยานิพนธ์นี้เป็นส่วนหนึ่งของการศึกษาตามหลักสูตรปริญญาวิศวกรรมศาสตรมหาบัณฑิต
สาขาวิชาวิศวกรรมเครื่องกล ภาควิชาวิศวกรรมเครื่องกล
คณะวิศวกรรมศาสตร์ จุฬาลงกรณ์มหาวิทยาลัย
ปีการศึกษา 2558

A 2D FINITE VOLUME SIMULATION OF ELECTRICAL POTENTIAL DROP IN CRACKED PLATES

Mr. Ni-Asri Cheputeh

A Thesis Submitted in Partial Fulfillment of the Requirements
for the Degree of Master of Engineering Program in Mechanical Engineering
Department of Mechanical Engineering
Faculty of Engineering
Chulalongkorn University
Academic Year 2015

Thesis Title	A 2D FINITE VOLUME SIMULATION OF ELECTRICAL POTENTIAL DROP IN CRACKED PLATES
By	Mr. Ni-Asri Cheputeh
Field of Study	Mechanical Engineering
Thesis Advisor	Associate Professor Kuntinee Maneeratana
Thesis Co-Advisor	Assistant Professor Jirapong Kasivitamnuay

Accepted by the Faculty of Engineering, Chulalongkorn University in Partial Fulfillment of the Requirements for the Master's Degree

....Dean of the Faculty of Engineering
(Professor Bundhit Eua-arporn)

THESIS COMMITTEE

....Chairman
(Associate Professor Pairod Singhatanadgid)
....Thesis Advisor
(Associate Professor Kuntinee Maneeratana)
....Thesis Co-Advisor
(Assistant Professor Jirapong Kasivitamnuay)
....Examiner
(Assistant Professor Sompong Putivisutisak)
....External Examiner
(Anchalee Manonukul)

นิอัสรี เจ๊ะปูเต๊ะ : การจำลองแบบความต่างศักย์ตกคร่อมรอยร้าวในชิ้นงาน ด้วยระเบียบวิธีไฟไนต์วอลุ่ม 2 มิติ (A 2D FINITE VOLUME SIMULATION OF ELECTRICAL POTENTIAL DROP IN CRACKED PLATES) อ.ที่ปรึกษาวิทยานิพนธ์หลัก: รศ. ดร. กุณฑินี มณีรัตน์, อ.ที่ปรึกษาวิทยานิพนธ์ร่วม: ผศ. ดร. จิรพงศ์ กสิวิทย์อำนวย, 84 หน้า.

วิธีวัดความต่างศักย์ตกคร่อมเป็นวิธีหนึ่งในการหาความยาวรอยร้าวในแผ่นโลหะ โดยเฉพาะในสภาพแวดล้อมที่อันตราย เช่น มีอุณหภูมิหรืออัตราการแผ่รังสีสูง ฯลฯ วิธีนี้อาศัยเส้นโค้งสอบเทียบซึ่งเป็นกราฟความสัมพันธ์ระหว่างความต่างศักย์ตกคร่อมรอยร้าวและความยาวรอยร้าวเพื่อคำนวณหาลักษณะรอยร้าวที่เกิดขึ้นในชิ้นงาน วิทยานิพนธ์นี้ได้ประยุกต์ใช้ระเบียบวิธีไฟไนต์วอลุ่มแบบกริดสี่เหลี่ยมด้านไม่เท่าเพื่อสร้างแบบจำลองการกระจายตัวของศักย์ไฟฟ้าภายในชิ้นงานที่มีรอยร้าว และคำนวณโดยโปรแกรมคอมพิวเตอร์ที่เขียนขึ้นด้วยภาษา C++ ผลการจำลองแบบที่ได้ถูกทดสอบผ่านการคำนวณเส้นโค้งสอบเทียบของชิ้นงานที่มีรอยร้าวที่ขอบและชิ้นงานที่มีรอยร้าวตรงกลางที่มีอัตราส่วนของความยาวรอยร้าวต่อความกว้างชิ้นงานตั้งแต่ 0.1 ถึง 0.8 ทุกช่วงอัตรา 0.1 พบว่าเส้นโค้งสอบเทียบที่ได้จากการคำนวณมีความแม่นยำเมื่อเปรียบเทียบกับผลเฉลยของจอห์นสัน โดยมีค่าเปอร์เซ็นความผิดพลาดสูงสุดเท่ากับ 1.15% สำหรับรอยร้าวที่ขอบและ 1.69% สำหรับรอยร้าวตรงกลาง

วิทยานิพนธ์นี้ได้ใช้ผลการจำลองแบบมาสอบเทียบรอยร้าวเอียงที่ขอบ ที่มีค่าความยาวรอยร้าวต่อความกว้างชิ้นงานตั้งแต่ 0.1 ถึง 0.8 และมุมเอียงของรอยร้าวตั้งแต่ 7.5 ถึง 45 องศา ทุก 7.5 องศา โดยใช้การวัดความต่างศักย์เพิ่มบริเวณรอบข้างตำแหน่งของรอยร้าวและสร้างเส้นโค้งสอบเทียบของอัตราส่วนของความต่างศักย์ข้างรอยร้าว การสอบเทียบความต่างศักย์ที่วัดได้กับเส้นโค้งสอบเทียบทั้งสองทำให้สามารถระบุลักษณะรอยร้าวเอียงได้ วิธีการนี้ถูกนำมาตรวจสอบความถูกต้องกับกรณีศึกษา 2 กรณี คือกรณีที่ชิ้นงานมีรอยร้าวเอียงที่ความยาวรอยร้าวต่อความกว้างชิ้นงานเท่ากับ 0.55 มุมเอียงเท่ากับ 40 องศา ได้ความผิดพลาดสำหรับการหาค่าความยาวรอยร้าวเท่ากับ 0.11% และสำหรับมุมเอียงเท่ากับ 0.25% ส่วนกรณีที่ชิ้นงานมีรอยร้าวเอียงที่ความยาวรอยร้าวต่อความกว้างชิ้นงานเท่ากับ 0.35 มุมเอียงเท่ากับ 10 องศา ได้ความผิดพลาดสำหรับการหาค่าความยาวรอยร้าวเท่ากับ 0.34% และสำหรับมุมเอียงเท่ากับ 4.5%

ภาควิชา วิศวกรรมเครื่องกล ลายมือชื่อนิสิต ....
สาขาวิชา วิศวกรรมเครื่องกล ลายมือชื่อ อ.ที่ปรึกษาหลัก ....
ปีการศึกษา 2558 ลายมือชื่อ อ.ที่ปรึกษาร่วม ....

5670468521 : MAJOR MECHANICAL ENGINEERING

KEYWORDS: ELECTRIC POTENTIAL DROP, FINITE VOLUME METHOD, CRACK MONITORING, CALIBRATION CURVE, INCLINED CRACK

NI-ASRI CHEPUTEH: A 2D FINITE VOLUME SIMULATION OF ELECTRICAL POTENTIAL DROP IN CRACKED PLATES. ADVISOR: ASSOC. PROF. KUNTINEE MANEERATANA, CO-ADVISOR: ASST. PROF. JIRAPONG KASIVITAMNUAY, 84 pp.

The electric potential drop technique is an effective crack monitoring method, especially in harsh environment conditions such as high-temperature and high-radiation, etc. In this method, the calibration curve - the relationship between potential drop across the crack and the crack sizes - is needed. This work employed a cell-centered finite volume discretization with unstructured quadrilateral mesh to model the potential distribution within cracked specimens. The numerical model is implemented via a C++ program. The program was used to calculate calibration curves of the single edge cracked and central cracked specimen with the crack length to specimen width ratios from 0.1 to 0.8 at 0.1 intervals. The numerical calibration curve conforms well with Johnson's analytical solutions with the maximum error of 1.15% in the single edge crack cases and 1.69% in the central cracked cases.

This thesis also uses the obtained model to determine the inclined edge crack shape with crack length to specimen width ratios varies from 0.1 to 0.8 and cracked angle from 7.5° to 45° at every 7.5° interval. The adjacent potential measured positions are added to establish another calibration curve of the adjacent potential ratio. With those two curves, the inclined crack shape can be identified. This method is verified by 2 case studies. The first specimen has an inclined crack with crack length to specimen width ratio of 0.55 and inclined angle of 40°. The predicted crack length error is 0.11% and cracked angle error is 0.25%. The second specimen has an inclined crack with crack length to specimen width ratio of 0.35 and inclined angle of 10°. The predicted crack length error is 0.34% and cracked angle error is 4.5%.

Department:	Mechanical Engineering	Student's Signature	....
Field of Study:	Mechanical Engineering	Advisor's Signature	....
Academic Year:	2015	Co-Advisor's Signature	....

ACKNOWLEDGEMENTS

I would like to sincerely thank my advisor, Assoc. Prof. Kuntinee Maneeratana for her teachings and excellent suggestions throughout this thesis. I feel very grateful to my co-advisor, Asst. Prof. Jirapong Kasivitamnuay who gives me the interesting idea for this work including to the extended research related to this topic. I am very thankful to the thesis committee, Assoc. Prof. Pairod Singhatanadgid, Asst. Prof. Sompong Putivisutisak and Dr. Anchalee Manonukul who give me the great comments to improve my work.

I want to express my heartfelt thanks to my schoolmates for their friendship, kindness helps and suggestions for a long time in the duration of master's degree programmes. Not to forget, every staff in administrative office of mechanical engineering department who help to make this work run smoothly.

Finally, I wholeheartedly appreciate my parents who give me one of the most valuable present, the education, and encourage me all the time.

CONTENTS

Page

Page

LIST OF TABLES

LIST OF FIGURES

Chapter 1

Introduction

1.1 Background and Signification

A structural component which has been subjected to cyclic loads may experience damages that lead to fatigue. The crack size increases with the number of load cycles and the catastrophic failure will occurs if the crack size reaches the critical value. For example, the accidents of Aloha-airline's plane in 1988 and the tanker Erika in 1999 were results of such damage [1].

Repairing a cracked component is expensive and often unproductive [2]. Prediction of a component's remaining service lifetime that the component can be safely used is a more economical approach. The service lifetime of a component is the time duration or the number of load cycles for the crack to grow from the initial size to the maximum allowable size which is then divided by a safety factor. The accuracy of service life prediction depends on the accuracy of the crack growth behavior determination. Thus, the monitoring of crack growth plays an important role in measuring the crack length and crack growth behavior of tested bodies or structures.

The monitoring of crack growth can be divided into two types, direct and indirect measurements. For the direct measurement, it is usually done by employing a traveling microscope. This technique requires manpower to examine crack length and the equipment must be able to access the structure during the testing. Therefore, it is not suitable for harsh environments, e.g. high-temperature and high-radiation, etc. In those cases, the indirect measurement has to be employed. The compliance method and the electric potential drop technique are popular indirect measurement types as they are reliable and stand the test of time.

The electric potential drop technique relies on the principle that the existence of crack or discontinuity in a conductive material causes the disturbance in the electric potential field. For a test specimen of width W, length L, and thickness t, the extension of crack disturbs the current flow across cross-sectional area A and causes the resistance R to increase. If the electric current I is constant throughout the test piece, the crack extension will raise the potential difference between two sides of the crack from the reference value V_0 at initial crack size a_0 to V_a at the crack length a. By monitoring the relationship between V_a and a, the calibration curve for this geometry can be established.

The reliability of both direct current (DC) and alternating current (AC) in the potential drop technique is equally accepted. The AC potential systems provide much greater sensitivity and better precision [3]. But the AC equipment is more specialized, relatively expensive and connecting wires must be carefully attached. Meanwhile, it may suffer the 'skin effect' problem, the non-uniformity of the current density through the thickness of a conducting material which affect the current's flow area and resistance. The DC potential system is simpler and less expensive [4]. When the these techniques are compared in details, it can be concluded that the DC method is more suitable to study crack growth, whereas the AC method is better for non-destructive testing (NDT) tool [5].

The calibration curve is the relationship between the normalized potential changed V_a/V_0 and the crack length to specimen width ratio a/W. Calibration curves can be determined experimentally, analytically or numerically. The experimental determination provides straightforward results for most problems but it requires equipment and complicated procedures for circuit setting. The analytical method can be employed for test pieces and cracks of simple geometries such as single edge cracked, central cracked and compact tension specimens [6] but cannot be applied for complex crack types or multi-physics problems. Thus, this analytical method is often used to verify a written computational program for basic cases. Lastly, although the numerical method is quite sophisticated and requires understanding of computer programming, this method has many distinctive advantages as it is inexpensive, quick and convenient for computing a reasonably accurate calibration curves. Thus, numerical procedure is utilized in this work.

In the past, researchers successfully employed the finite element method (FEM) to determine the calibration curves [7-14]. As this FEM was initially developed for structural analyses, it is certainly a very powerful tool. However, it was not as good as the finite volume method (FVM) in coping with extreme nonlinearities that are commonly found in thermos-fluid problems. Interestingly, the distribution of electric potential within conductive material in some operating situations should be considered nonlinear as the non-uniform temperature within a test specimen directly affects the changes of the electric resistivity ρ [15]. Although it is unclear whether the plastic deformation around a crack tip influences the changes of the electric resistivity, Ritchie & Bath [7] and Doremus *et al.* [12] concluded in their works that it might be able to disrupt the electric potential drop.

As the discretization process of the finite volume method ensures physical conservation of every control volume [16], this numerical technique is quite stable for nonlinear problems. Due to the similarity of governing equations of the electric potential distribution and heat conduction problems, the finite volume technique is an interesting alternative numerical method to solve the distribution of electric potential and is, thus, chosen for this thesis.

With the aim of obtaining refined and complex nonlinear electric potential distribution problems in the future, this work starts with utilizing the finite volume method with unstructured grids to solve basic crack problems, i.e. single edge cracked and central cracked specimens as well as a more complex cracked plane, the inclined edge cracked specimen. In the near future, the computer program will be further developed to solve the other complex crack types, surfaced cracks or multiple cracks with various specimen geometries.

1.2 Objectives

This thesis aims to develop a finite volume C++ code with unstructured quadrilateral mesh to solve the equation of electric distribution in cracked specimens.

1.3 Scope of the Research

The determination of electric potential distribution of this thesis is limited to two dimensional rectangular plates with through-thickness cracks. The studied crack types are single edge crack, center crack and inclined edge crack. The position of crack mouth is assumed to be known before the potential drops across cracks are simulated to establish the calibration curve.

1.4 Research Schedule

1) Study the principle and related theory of electric potential drop techniques for crack growth monitoring.

2) Study the finite volume technique for unstructured mesh and an existing unstructured quadrilateral grid generating program.

3) Write a C++ computer program for simulating the distribution of electric potential throughout uncrack plates and validate the results with analytical solution.

4) Write a C++ computer program for simulating the distribution of electric potential throughout basic cracked specimens. Then, plot the calibration curves and validate them with analytical solutions and existing experimental data.

5) Write a C++ computer program for simulating the distribution of electric potential throughout the inclined cracked specimen. Then, develop the methodology to characterize the inclined crack shape and validate it with case studies.

6) Conclude and discuss the obtained results.

1.5 Expected Benefit

This work develops a computer program for simulating the potential drops in cracked specimens to generate calibration curves for the electric potential drop technique for crack monitoring in specimens with simple geometry. In the future, there will probably be a further development of this program to support more complex problems such as the multiple cracks problems, round-shaped crack problems or non-linear materials.

Chapter 2

Literature Review

Fracture mechanics always play an important role in an assessment of the failure of structural components. This chapter presents the importance of the crack monitoring techniques in lifetime assessment of structural components and the means to monitor cracks as well as the advantages and disadvantages of each method. The obtained information is used to make a decision in choosing the proper method for this thesis.

2.1 Degradation of Structured Component

Unexpected loads and environmental conditions such as high temperature and corrosive etc., during operation are main factors that gradually destroy a component. Firstly, the damage causes a failure in microscopic scale. This failure would grow into a macroscopic flaw before becoming the catastrophic failure. The degradation of materials can affect directly the performance and lifetime of a structure component.

In the past, the degradation of materials might lead to catastrophic incidents. Vessels, pipelines, aircrafts, railway, ships and vehicles are some of structured components which always experience the degradation that might lead to the serious accidents [1, 17, 18]. The example of failures likes the Westland Lynx SH14D helicopter in 1998 [19], the tanker Erika in 1999 and Prestige in 2002 [1].

2.2 Service Life Time Assessment

Defected structures are expensive to repair and often unnecessary [2]; fracture mechanics play a role to provide a rational basis service life time assessment of components. Commonly, the objective of the service life time assessment is to provide the appropriate interval inspection, repair and maintenance as well as ensuring that the failure would not occur during the operating periods.

For cracked materials under cyclic loads, the service life time assessment is the determination of the time t which crack size propagates from cyclic loads from an initial a_0 to the critical size a_c which causes a catastrophic failure. Thus, to predict the remaining life of crack materials, it is unavoidable to determine the crack growth rate of the test specimen da/dt which can be calculated by employing crack monitoring technique.

2.3 Crack Monitoring Technique

Crack monitoring techniques are utilized to investigate the crack growth information of test structures. It is often conducted in a laboratory under a real component's operating conditions, i.e. environment, geometry and load etc. The laboratory testing information can be used as reference for calculating the service life time assessment of a real structure. Crack monitoring techniques can be divided into direct and indirect measurements.

The direct measurements method relies on direct access of the crack. The crack growth is monitored by a travelling microscope with a magnification of 20-50x [4]. This method is simple, inexpensive and calibration is not required. However, this method required a lot of time, an automate system is expensive and the examined material must be able to access the structure during the test. Moreover, the measured crack length is usually underestimated because the sub-surface crack size is generally longer than the surface crack and a sub-surface crack length cannot be examined with this technique.

In a harsh environment, i.e. high temperature, high radiation, corrosive environment etc., the examiner cannot gain access to the test specimen. The indirect measurement techniques are developed to counter that problem. According to ASTM E647-08, there are 2 indirect measurement, compliance method and electric potential method [20].

The compliance method relies on the changes of material compliance as crack grows. The gauge is used to measure the changes of strain or crack mount opening displacement under load. This method is simple, convenient to automate and can be used for various material geometry and in aggressive environment. However, this method is inappropriate for ductile materials because the occurrence of plastic zone during crack growth may decrease the accuracy of the prediction. [4, 11, 21].

The electric potential drop technique uses the fact that a crack interrupts an electric potential field when a constant current passes through a body. The changing of electric potential around the crack used to interpret the geometry of the crack. This method is simple, inexpensive, stable, can be automated and amenable for long-term high-temperature testing [4]. The distinctive limitation for this method is the requirement of proper calibration curve in order to interpret the measured potential drop to crack size. In addition, the underestimation of the crack depth may occur if crack faces come into contact creating a short circuit situation [11].

2.4 Electric Potential Drop Technique

The chosen technique is the direct current potential drop method. This technique is widely used in fracture testing and can be used for any crack geometries. However, a proper calibration curve, required for each specimen geometry and crack types, are complicated to determine.

The electric potential drop technique relies on the principle that the existence of a crack or discontinuity in conductive material causes the disturbance in the electric potential field. Consider a cracked body in Fig. 2.1, the extension of the crack decreases the current flow across the cross-sectional area A which then causes the resistance R to increase. If the electric current I is constant throughout the test piece, the potential difference between two sides of crack V_a rises. By monitoring the relationship between the potential increase V_a and the crack length a, the calibration curve for each geometry can be established.

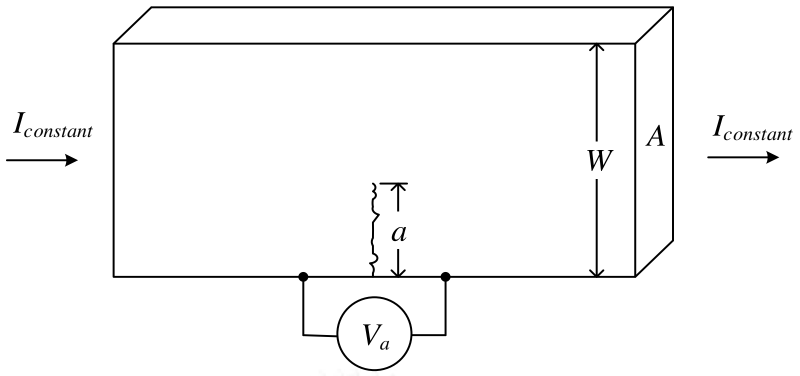

Fig. 2.1 A cracked specimen in an electric potential drop testing

Typically, a calibration curve is the relationship between the ratio of potential change and a reference potential V_a/V_0 against the ratio of crack length to specimen width a/W (Fig. 2.2). This relationship can be calculated by analytical [6], experimental [6-12] and numerical methods [7-14].

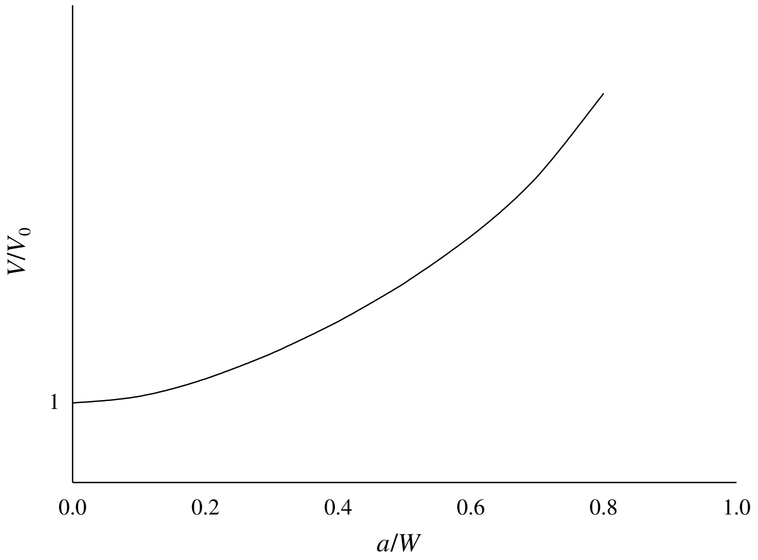

Fig. 2.2 An example of a calibration curve

The analytical method provides an convenient mean to generate a calibration curve. However, its application is limited only for basic cracked specimen, i.e. compact tension specimens, single edge crack specimens and central crack specimens [6]. Thus, this method is usually used to verify results from another method.

The experimental method is used to determine calibration curves of specimens with more complex geometries. As the actual operating condition can be exactly duplicated with this method, the most straightforward results can be obtained. But this method requires experimental equipment, which certainly increases the expenses, and the circuit setting procedure is complicated and involves the difficulty of crack evolution measurement for the surface crack growth [12, 22].

Although the numerical method is sophisticated, however it is a convenient and inexpensive technique to determine the distribution of potential within cracked specimen and generate a calibration curve. It can simulate various complex geometry and environment duplicated from actual operating condition. Thus, with many attractive advantages, this method is chosen for this work.

2.5 Inclined Crack Detection

Characterization of an inclined crack is more complicated than that of the basic cracks, i.e. compact tension, single edge crack and central crack. Not only the crack size but also inclination of the crack must be known. This crack type can be commonly found in railway track which is occurred by mixed mode loading such as rolling contact fatigue.

In the past, the researchers proposed many specific methods to detect the inclined crack. Some researchers applied the calibration curves technique and some of them created their specific ways to characterize the crack as follows.

2.5.1 Calibration Curves Method

As described before, a single calibration curve across the crack is not enough to accurately determine this inclined crack type, especially the inclination angle of crack. The different inclination angle of crack disturbs the electric potential field over the specimen in different ways. Kornchamruskul (2005) [13] and Spitas *et al.* (2010) [14] proposed additional measured points in order to monitor the changes in electric potential drop due to crack shape, especially the inclination angle and, thus, establishing another calibration curve. By measuring the potential drops across monitoring point pairs, the inclined crack shape can be predicted.

2.5.1.1 The I_y-V_y; I_y-V_x and I_y-V_y; I_x-V_x Method

Kornchamruskul [13] proposed two methodology for characterizing an inclined central crack. The first method is called the I_y-V_y; I_y-V_x method; the current is induced in *y*-direction, then, the potential across the crack is measured in *y*-axis and *x*-axis as shown in Fig. 2.3(a). The second is called the I_y-V_y; I_x-V_x, which is similar to the first, except that the current is induced in the *x*-direction while the potential across the crack in the *x*-axis is being measured as shown in Fig. 2.3(b). Each method requires two calibration curves from their two specific cases.

For example, the I_y-V_y; I_y-V_x method (Fig. 2.3(a)) requires the calibration curves from the I_y-V_y case and the I_y-V_x case. The calibration curves of the I_y-V_y case is the relationship between the ratio of potential change across the crack in *y*-axis and a reference potential V_y/V_0 against the ratio of crack length to specimen width a/W at different inclined angle θ as shown in Fig. 2.4(a). For the I_y-V_x case, the calibration curve is the relationship between the potential change across the crack in *x*-axis V_x against the ratio of crack length to specimen width a/W at different inclined angle θ as shown in Fig. 2.4(b). The electric current is induced in *y*-direction for both cases.

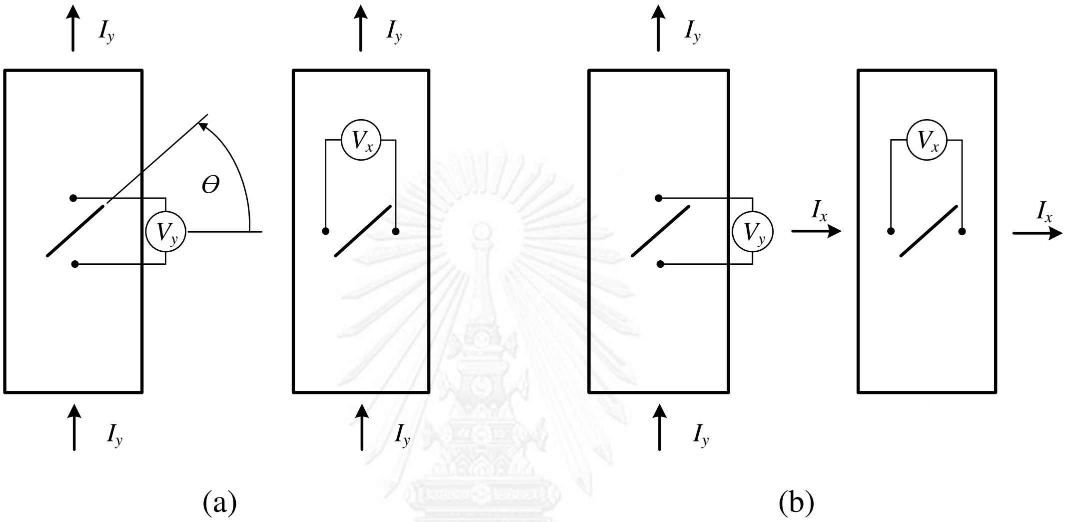

Fig. 2.3 The method for characterizing an inclined central crack:
(a) The I_y-V_y ; I_y-V_x method, (b) The I_y-V_y; I_x-V_x method [13]

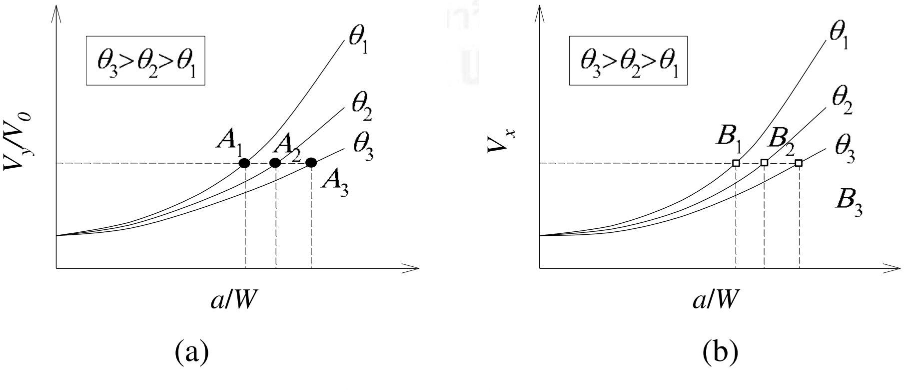

Fig. 2.4 Two calibration curves from the I_y-V_y ; I_y-V_x method:
(a) the I_y-V_y case and (b) the I_y-V_x case [13]

The procedure to characterizing an inclined crack begins with measuring the potential across the crack V_y and V_x. Then, the corresponding values of a/W and θ are determined as points A_1, A_2 and A_3 in Fig. 2.4(a) for the I_y-V_y case and points B_1, B_2 and B_3 in Fig. 2.4(b) for the I_y-V_x case. Finally, the corresponding values of a/W and θ from each case are plotted in the same graph and a best fit curve is determined as shown in Fig. 2.5. The intersection from these two curves represents the information of inclined crack.

The limitation of this method is that the center of the inclined central crack must be known before measuring the potential difference. Thus, this methodology is hard to apply with real structures.

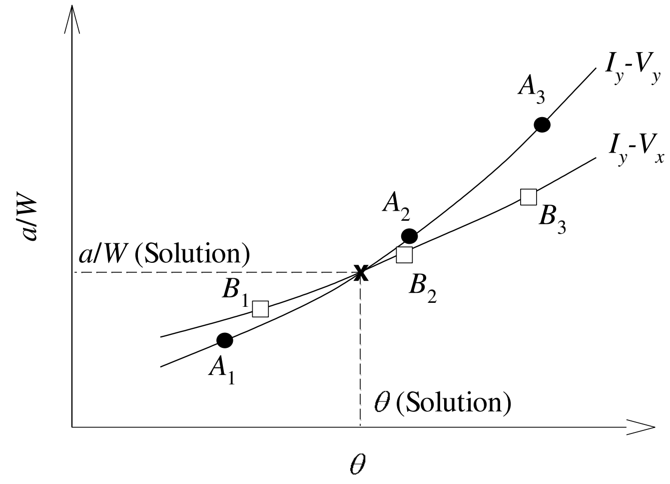

Fig. 2.5 Inclined crack characterizing from the intersection [13]

2.5.1.2 A Three-Point Electrical Potential Difference Method

In 2010, Spitas *et al.* [14] presented a technique for assessment an inclined edge crack in a specially designed specimen as shown in Fig. 2.6 at crack length from 1 to 6 mm at 1 mm intervals and the crack angles θ of 0° to 40° at 10° intervals.

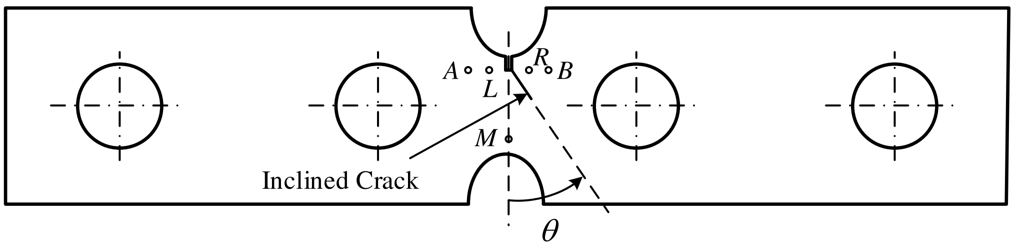

Fig. 2.6 The inclined edge crack in a designed specimen of Spitas *et al.* [14]

A constant current passes from point A to point B and creates a distribution of electrical potential within the specimen. By calibrating the normalized potential difference across the crack between points L and R, $(V/V_0)_{LR}$, where V_0 is the initial measurement of the same points at zero crack length, with the calibration curve of the normalized potential difference across the crack as shown in Fig. 2.7, crack length is obtained.

The measurement at point *M* in Fig. 2.6 is added in order to monitor a non-symmetric potential field creating from the inclined crack in different degree levels. The inclination angle θ can be found by determining the normalized potential drop between points *L-M* and *R-M*, $(V/V_0)_{LM}$ and $(V/V_0)_{RM}$ respectively, and then, calibrating with the plot of $(V/V_0)_{LM}$ and $(V/V_0)_{RM}$ in Fig. 2.8. The coordinates of $(V/V_0)_{LM}$ and $(V/V_0)_{RM}$ is represented by point *A*. The crack angle θ can be determined by interpolating the inclination angle θ at point *A* with two adjacent curves.

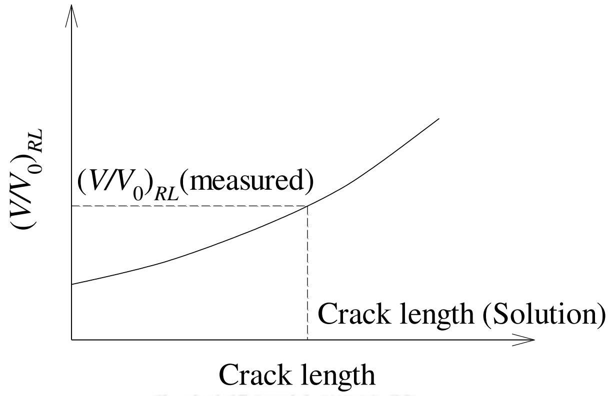

Fig. 2.7 Calibration curve of the normalized potential across the crack $(V/V_0)_{LR}$ for all crack angle [14]

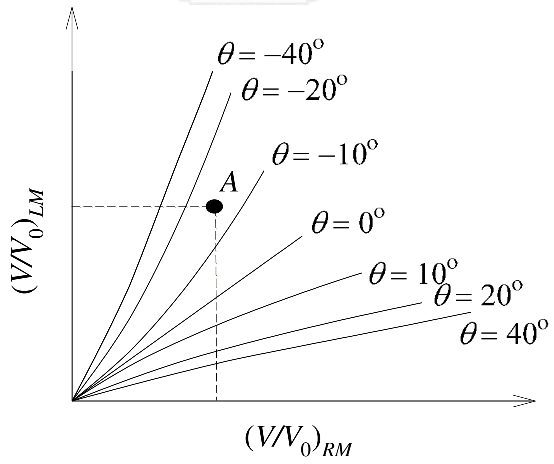

Fig. 2.8 The plot of $(V/V_0)_{LM}$ and $(V/V_0)_{RM}$ for different crack angle θ [14]

The period of crack length in this work is quite shot at crack length to specimen width ratio less than 0.4 and the inclination angle is only up to 40° to the transverse axis of symmetry of the specimen. The orientation of crack within this range may not cause the obvious change in potential drop between points *L* and *R* such that the authors can calibrate the crack length by only measuring the potential drop between points *L-R*. However for longer cracks, the change in inclination angle certainly affects the change in potential drops across the crack. Thus, this methodology may not extend to detect long inclined cracks.

2.5.2 Back Wall Measurement Method

In 1990, Abe and Kanoh [23] presented a technique to determine the location, size and inclination of crack in the cracked infinite strip. The infinite strip of which both upper and lower surfaces are insulated except for the current input and current output positions is shown in Fig. 2.9.

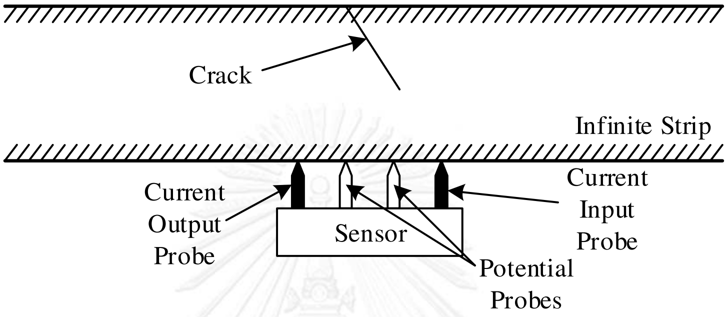

Fig. 2.9 The inclined crack detection method of Abe and Kanoh [23]

Firstly, the sensor is moved to measure the electric potential along the measuring surface. The approximate crack position is estimated as the position of the maximum value of potential difference between two probes is detected. Then, the detailed measurements are conducted on a number of points on the surface near the approximate crack position. The location, size and inclination of crack are determined by means of the optimization procedure which is conducted by comparing the measurement values with the analytical results of the authors.

The limitation of this approach besides the complication of the mathematical process in finding the analytical equations is that the inclined crack detection is limited in infinite strip. Thus, it is difficult to apply this method for other finite cracked specimen.

2.5.3 Defect Influence Factor Method

In 2002, Chen *et al.* [24] proposed a method to detect crack in a pipe by depicting the contour of defect influence factor which is the ratio of the electric potential of the defective pipe divided by that of the perfect one. By analyzing this contour, the position, shape and length of the crack can be predicted. However, the potential must be measured throughout the specimen and the accuracy of the predicted crack is constrained by the potential measured density.

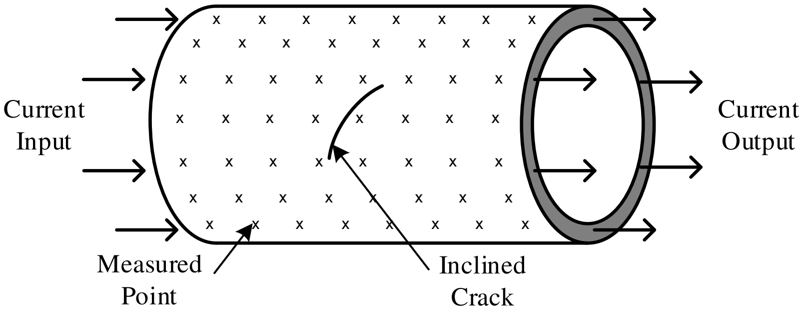

Fig. 2.10 The inclined crack detection method in a pipe by Chen *et al.* [24]

2.6 Numerical Method for Electric Potential Drop Technique

The numerical technique is a popular method for simulating the distribution of electric potential within specimens in order to establish a calibration curve for the crack monitoring by the electric potential drop technique. This method involves finding solutions of Laplace's equation under boundary conditions of the test piece. The steady state electric potential equation is given by

$$\nabla^2 V = 0 \tag{2.1}$$

where V represents the electric potential.

As describe above, it is difficult and sometimes impossible to solve this Laplace's equation under complex condition directly. So, numerical method comes to play a role in solving this equation. There are 2 popular numerical techniques, the finite element and the finite volume method that can be used to solve this Laplace's equation.

2.6.1 The Finite Element Method

In the past, the finite element method had been employed by many researchers to solve electric potential distribution problems. The various computer programs had been used such as ABAQUS [11, 12]. This technique had been utilized to generate the calibration curves in various geometry from the through-thickness crack problems [7-11, 13, 14] to crack growth from surface flaw problems [12].

For basic through-thickness crack problems, like compact tension specimens, single edge crack specimens and central crack specimens, the numerical calibration curves can be verified by comparing with both experiment and Johnson's equations [7, 9, 10]. These basic 2D geometries can be applied for monitoring the crack growth of 3D hollow cylinder [11]. The numerical method, moreover, had been utilized to examine the optimum location of current input and potential measurement leads according to its accuracy, sensitivity, reproducibility and measurability.

For more complex crack geometries, Pulle [8] emloyed a finite element technique to study the influence of asymmetrical crack growth. His study revealed that the underestimation of crack length prediction could occurr if electric potential probes were placed close to the asymmetrical crack.

Kornchamruskul [13] and Spitas *et al.* [14] both used the finite element method to establish 2 calibration curves in order to characterize the inclined crack of their works as described before in section 2.8.1.

Recently, Doremus *et al.* (2015) [12] used a finite element method to determine the calibration curve of crack growths from surface anomalies. This research tried to establish a calibration curve in terms of crack depth and potential drop measurement. However, the scatter of experimental measurement was large. The author concluded that errors occur from the complexity of crack propagation geometry and the effect of plastic deformation during the process.

The grid arrangement is a factor that affects the accuracy of results due to differences in discretized simultaneous algebraic equations. Therefore, the suitable grid would provide convenient determination procedure and acceptable results. In the finite element method, the grid within domain comprised of elements. Each of them is connected at nodal points and the values at the points are used to calculate the values within boundary.

For 2D problems, the triangular element has been usually employed because of the ease for generating and coping with complex geometry. Basically, there are 3 nodes at 3 element vertices. The interpolation within an element is linear polynomial. However, this element type can be improved by placing more nodes at the edge of element sides to improve its approximation accuracy. The use of this grid type includes the work of Kornchamruskul (2005) which 3-noded linear elements as well as Pulle (1986) and Spitas

et al. (2010) in which 6-noded isoparametric triangular elements was employed.

The unstructured quadrilateral element has been used often. Normally, 4 nodes are placed at the vertices of each element. This element type uses nonlinear approximation within element. Therefore, at the same node numbers, the quadrilateral element can provide more complex interpolation, comparing with the triangular element. Similarly there are higher-order elements of 8-noded isoparametric quadrilateral element of Ritchie and Bathe (1979) and 4-noded linear element of Gandossi *et al.* (2001).

In 1983, Wilson [9] took the advantages of each element type and combined them together. The ordinary regions of specimen are modelled with quadrilateral elements while the near crack tip area is modelled with very fine triangles elements. This method helps to reduce time consumption in computation due to less nodal points and equations from using quadrilateral elements and, on the other hand, improves accuracy of the results because very fine meshes of triangular elements are used only in high gradient regions.

2.6.2 The Finite Volume Method

This technique has never been employed to solve the steady state electric potential problems. Nevertheless, finite volume is one of a most widely used technique to solve heat conduction problems of which the governing equation is similar to the electric potential problems. Because the heat conduction problem is held to be a simple heat transfer problem and typically, the analytical solution can be determined. Therefore, this problem has been always used to verify the quality of refined grids [25, 26] or approximation methods [27, 28].

By applying the Fourier's law of heat conduction for an isotropic material without internal heat source in thermal equilibrium, the governing equation is

$$\nabla^2 T = 0 \tag{2.2}$$

where T is temperature.

The structured and unstructured control volumes have been both employed to represent the domain. For a structured control volume, the discretization procedure can be conducted conveniently. Because of the certain alignment of this grid type, more accurate results can be obtained if the grid is aligned with the predominant flow direction of that problem. The example of a use of structured control volumes likes Prapainop and Maneeratana [27] in simulating the formation of ice.

For complex geometries, the unstructured modelling is unavoidable. This control volume has a high flexibility to fit a complex geometry. It can reduce computational costs and increase accuracy because this grid type can be refined for particular area where finer meshes are needed. However, the grid generation and discretization procedure for the unstructured grids are quite complicated. Furthermore, the grid non-orthogonality would cause to the error of the results which is called the skewness error [29]. The example of unstructured control volumes use likes the use of Delaunay triangular control volumes of Lertsurayut and Maneeratana [25] and the refined rectangular control volumes of Wattananukulchai and Maneeratana [26].

2.7 Conclusion

This chapter points out the importance of remaining-life assessment procedure; determination of crack growth behavior within bodies is needed. To know crack growth behavior, a reliable technique for measuring crack size should be employed. For a test material which cannot be accessed by the examiner, the indirect method, such as the compliance method and the electric potential drop method, are better means to monitoring crack growth in material in that situation.

This thesis chooses the electric potential drop technique which required a proper calibration curve to predict crack size or crack angle. This technique can be applied to characterize the inclined crack which previous works are discussed in this chapter.

The numerical technique has always been employed to calculate the calibration curve. Previous researches reveal that the finite element technique is popular for determining a calibration curve with various crack shapes and geometries.

Although the finite volume method has never been employ to solve the electric potential distribution problems but this method has been employed to solve heat conduction problems which the governing equation is similar to the potential distribution problems.

Thus, this thesis tries to introduce an alternative way by using the finite volume technique to solve the electric potential distribution problem and generate the calibration curves of cracked specimen with an unstructured quadrilateral grid. Although the discretization procedure with an unstructured quadrilateral grid is quite complicated, but this grid shape can be conveniently generated for complex geometry, such as the domain of inclined cracked specimens.

Chapter 3

Basic Electrical Theory

To determine the crack size and crack growth rate in the specimen by the method of potential drop measurement, the main governing equation in this work is the partial differential equation for the steady electric potential. To deeply understanding this equation, this chapter describes equations about basic electrical theory [30] and conservation of charge [31]. In addition, this chapter gives a description of how the material geometry affects the resistance that causes the electric potential difference under a crack influence.

3.1 Electric Potential

When a point charge q_0 moves in the electric field with magnitude $\mathbf{E}$ from a point a to a point b (Fig. 3.1), the force $\mathbf{F} = q_0\mathbf{E}$ are exerted on the point charge. The work done from points a to b by that force, $W_{a\to b}$, is given by a line integral

$$W_{a\to b} = q_0 \int_a^b \mathbf{E}\cdot d\mathbf{l} \tag{3.1}$$

where $d\mathbf{l}$ is infinitesimal displacement of the point charge's motion.

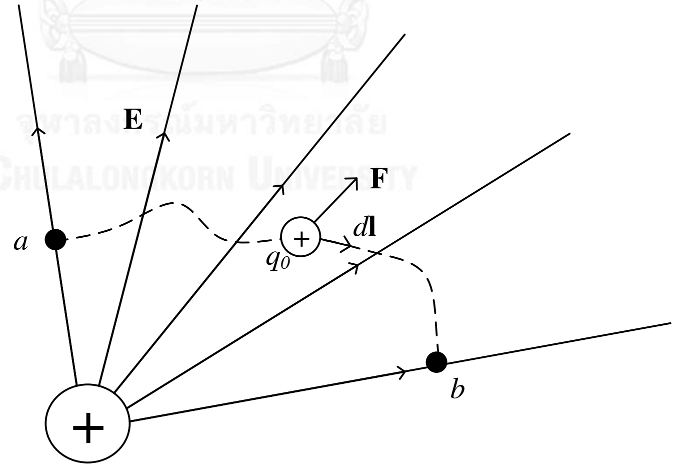

Fig. 3.1 The movement of point charge q_0 in the electric field $\mathbf{E}$

This work done by the electric force $\mathbf{F}$ can be expressed in terms of a potential energy U. When U_a is potential energy of point charge at the point a and U_b is potential energy of point charge at the point b, the work done $W_{a\to b}$ by this force can be written as

$$W_{a\to b} = U_a - U_b \tag{3.2}$$

The potential energy U per unit charge is defined as a potential V which is a scalar quantity. The potential of point charge q_0 at a position of the potential energy U is

$$V = \frac{U}{q_0} \tag{3.3}$$

Eq.(3.3) can be substituted into Eq.(3.2) to find work done in terms of potential as

$$W_{a\to b} = q_0(V_a - V_b) \tag{3.4}$$

V_a and V_b are electric potential at point a and b respectively. The difference of potential $V_{ab} = V_a - V_b$ is the potential of a with respect to b. From Eq.(3.1) and (3.4)

$$V_a - V_b = -\int_a^b dV = \int_a^b \mathbf{E}\cdot d\mathbf{l} \tag{3.5}$$

From Eq.(3.5)

$$-dV = \mathbf{E}\cdot d\mathbf{l} = E_x dx + E_y dy + E_z dz \tag{3.6}$$

where E_x, E_y and E_z are the magnitude of electric field in x, y and z axis respectively while dx, dy and dz are the infinitesimal displacement in each axis x, y and z. Suppose that a charge moves parallel to x-axis, so $dy = dz = 0$, then $-dV = E_x dx$ or $E_x = -(dV/dx)_{y,z\ \text{constant}}$ or in partial derivative form $E_x = -\partial V/\partial x$. Similarly, for a charge moving parallels to y-axis and z-axis.

Thus, the **E** can be re-written in vector form

$$\mathbf{E} = -\left(\hat{\mathbf{i}}\frac{\partial V}{\partial x} + \hat{\mathbf{j}}\frac{\partial V}{\partial y} + \hat{\mathbf{k}}\frac{\partial V}{\partial z}\right) \tag{3.7}$$

or can write in the gradient form as

$$\mathbf{E} = -\nabla V \tag{3.8}$$

where the quantity ∇V is called the potential gradient.

3.2 Electric Current

If an electric field is present inside a conductor, a charge particle inside the material is forced to move with drift velocity, $\mathbf{v}_d$. Suppose during the small time dt, there is n moving charges per unit volume through the cross-sectional area A and each particle has a charge q (Fig. 3.2). The charge dQ which flows during the time dt is

$$dQ = nqv_d A dt \tag{3.9}$$

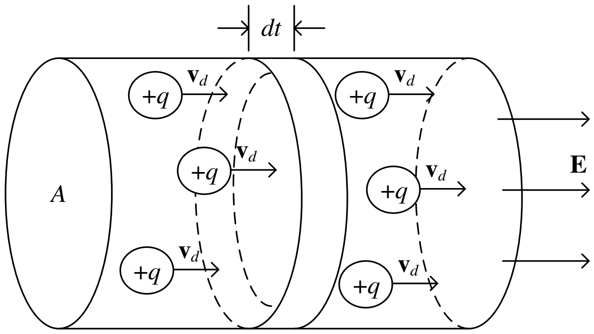

Fig. 3.2 Flow of the particle charges inside a conductor

The definition of current is the net charge flowing through the area per unit time. Thus, current I can be written as

$$I = \frac{dQ}{dt} = nqv_d A \tag{3.10}$$

The current per unit cross-sectional area is called the current density $\mathbf{J}$ which its direction is the same as electric field

$$\mathbf{J} = \frac{I}{A}\hat{\mathbf{n}}_{\mathbf{E}} \tag{3.11}$$

where $\hat{\mathbf{n}}_{\mathbf{E}}$ is the unit vector of electric field, $\hat{\mathbf{n}}_{\mathbf{E}} = \mathbf{E}/E$, or the total current I through a surface A is

$$I = \int_A \mathbf{J} \cdot d\mathbf{A} \tag{3.12}$$

Due to the current density is a vector quantity, so the current density $\mathbf{J}$ can be expressed in term that include the direction of drift velocity $\mathbf{v}_d$ as

$$\mathbf{J} = nqv_d \tag{3.13}$$

3.3 Resistivity

The resistivity ρ depends upon the property of each material. In general, this variable could be calculated with complex equation, but for some type of materials, especially metals, at the constant temperature, the resistivity ρ can be defined by the ratio of the magnitude of electric field and current density

$$\rho = \frac{E}{J} \tag{3.14}$$

Due to the same direction of electric field $\mathbf{E}$ and current density $\mathbf{J}$, the Eq.(3.14) can be written as

$$\mathbf{E} = \rho\mathbf{J} \tag{3.15}$$

In practice, the potential difference V and total current I are of higher interest and much easier to measure than electric field **E** and current density **J**. Suppose the magnitude of electric field **E** and current density **J** are uniform throughout the conductor with uniform cross-sectional area A and Length L, the potential difference V is given by Eq.(3.5) that is $V = EL$ or $E = V/L$ and the total current I is applied from Eq.(3.12) to be $I = JA$ or $J = I/A$. Then, substitute these two results in Eq.(3.15),

$$\frac{V}{L} = \rho\frac{I}{A} \quad \text{or} \quad V = \frac{\rho L}{A} I \tag{3.16}$$

From the Ohm's law, the ratio of potential difference V and total current I is called resistance R

$$R = \frac{V}{I} \tag{3.17}$$

Comparing this equation with Eq.(3.16) , the relationship between resistance and resistivity is

$$R = \rho\frac{L}{A} \tag{3.18}$$

3.4 Conservation of Charge

If the net current I flowing out of volume V, which is enclosed by closed surface **S**, is non-zero as Fig. 3.3, the total charge Q should decrease in accordance with the principles of conservation of charge , i.e.,

$$I = -\frac{dQ}{dt} = -\frac{d}{dt}\int_V \rho_V dV = \int_V \left(-\frac{d\rho_V}{dt}\right) dV \tag{3.19}$$

where ρ_V is the density of charge per volume. Consider Eq.(3.12), current I flowing thought the closed surface **S** is

$$I = \oint_S \mathbf{J} \cdot d\mathbf{S} \tag{3.20}$$

With use of the divergence theorem, Eq.(3.20) becomes to

$$I = \int_V (\nabla \cdot \mathbf{J}) dV \tag{3.21}$$

Comparing Eq.(3.19) and (3.21) leads to

$$\nabla \cdot \mathbf{J} = -\frac{d\rho_V}{dt} \tag{3.22}$$

Combinating Eq.(3.8) and (3.15) to obtain current density $\mathbf{J} = -\nabla V/\rho$ and substituting this into Eq.(3.22)

$$\frac{\nabla^2 V}{\rho} = \frac{d\rho_V}{dt} \tag{3.23}$$

Under static condition, the charge density ρ_V is independent of time or $d\rho_V/dt = 0$. Thus, the final equation is

$$\frac{\nabla^2 V}{\rho} = 0 \text{ or } \sigma(\nabla^2 V) = 0 \tag{3.24}$$

where σ is the reciprocal of resistivity ρ or conductivity $\sigma = 1/\rho$.

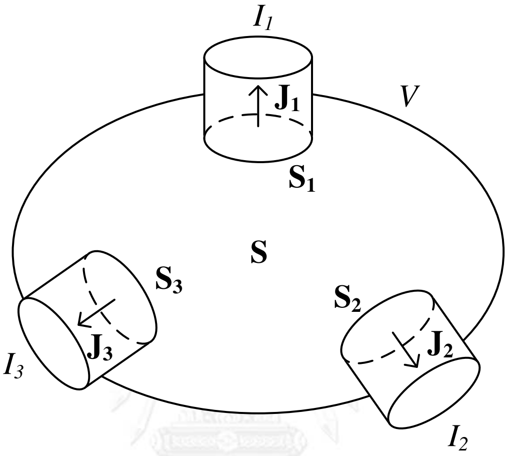

Fig. 3.3 Net current I flowing out of volume V

3.5 Conclusion

This chapter gives descriptions of basic electrical theory. In the beginning, the necessary electrical variables are introduced, i.e. electric potential, electric current and resistivity. Then, the conservation of charge is employed to prove the Laplace's equation is the governing equation for determining the distribution of potential within cracked specimens.

The electric resistance is also mentioned in this chapter. Consider Eq.(3.18), it is shown how cross-sectional area A affects the resistance of the specimen. Similarly to the occurrence of crack within specimen, it decreases the current flow cross-section area which causes the resistance increase. This also disturbs the distribution of electric potential field within defected material.

Chapter 4

Finite Volume Method

To build a mathematical model to simulate the potential distribution in any cracked bodies by the finite volume method, the discretization of partial differential equations in the form of algebraic equations is the first procedure that is extremely important. Then, the discretized simultaneous equations had to be assembled, load and boundary condition set and solved. The type and size of grid influences the accuracy of obtained results. This chapter gives the description of the grid and discretized procedure of the governing equation and the solving procedures.

4.1 Spatial Discretization

The shape of the employed grid is unstructured quadrilateral with node positioned at the centroid in the cell-centered grid arrangement as shown in Fig. 4.1 [26]. There are also boundary nodes at external cell face for the specification of boundary conditions. The grids that are used in this study are generated conveniently by a free mesh generator program, Automesh2D [32].

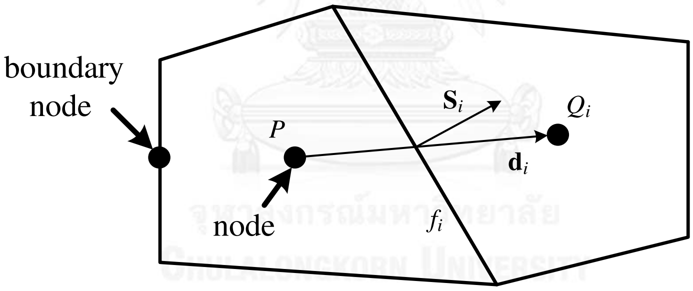

Fig. 4.1 Typical unstructured quadrilateral cells [26]

Consider a typical cell *P* in Fig. 4.1, a node *P* is located at the center of the cell. Subscript i = 1..4 represents the four sequence of adjacent cells. The S_i are surface vectors which are perpendicular to faces f_i and point toward the surrounded control volumes. The $\mathbf{d}_i$ are distance vectors from center, point *P* to points Q_i at the center of adjacent cells. The boundary cell served as a dummy node for the specification of the boundary condition.

4.2 Governing Equation

The main governing equation for this problem is the Laplace's equation of electric potential that was described in Chapter 3. The basic principles of electricity and electric continuity equation in Eq.(3.24) is $\sigma(\nabla^2 V) = 0$.

In the finite volume discretization procedure, this second order partial differential equation must be transformed into simultaneous algebraic equations to calculate the potential for every computational nodes. The procedure approximate the variables at cell faces so that the fluxes crossing the cells can be found for the conservation equation. The procedure follows the study by Muzaferija [33].

4.2.1 Spatial Distribution of Variables

For linear distribution problem, the value of assumed spatial variable ϕ_r at position vector **r** can be determined by truncating the Taylor series. Given the value of variable at position vector $\mathbf{r}_P$ is ϕ_P, the spatial variable ϕ_r is calculated according to

$$\phi_r = \phi_P + (\nabla\phi)_P \cdot (\mathbf{r} - \mathbf{r}_P) \tag{4.1}$$

where $(\nabla\phi)_P$ is the gradient of ϕ at point P.

The gradient vector at any cell $(\nabla\phi)_P$ can be calculated by ensuring a least square fit of ϕ through node P and neighboring node Q_i using the relationship between a matrix **G** and vector **h** as follow,

$$\mathbf{G} \cdot (\nabla\phi)_P = \mathbf{h} \tag{4.2}$$

where

$$\mathbf{G} = \sum_{i=1}^{nb} \frac{\mathbf{d}_i \otimes \mathbf{d}_i}{|\mathbf{d}_i|^3} \tag{4.3}$$

and

$$\mathbf{h} = \sum_{i=1}^{nb} \frac{(\phi_P - \phi_{Q_i})\mathbf{d}_i}{|\mathbf{d}_i|^3}. \tag{4.4}$$

The value of face gradient $(\nabla\phi)_{fi}$ of control volume can be determined through Eq.(4.1). By averaging the gradients from node P and node Q_i, the relationship is

$$(\nabla\phi)_{f_i} = \frac{(\nabla\phi_P + \nabla\phi_{Q_i})}{2} + \frac{(\nabla^2\phi)_P \cdot (\mathbf{r}_i - \mathbf{r}_P) + (\nabla^2\phi)_{Q_i} \cdot (\mathbf{r}_i - \mathbf{r}_{Q_i})}{2}. \tag{4.5}$$

4.2.2 Equation Discretization

The governing equation is $\sigma(\nabla^2 V) = 0$ from which the discretization process transforms into algebraic equation with primary unknowns ϕ. Consider the node P which represents the control volume V_P, the Eq.(3.24) is integrated over that control volume

$$\int_{V_P} \sigma(\nabla^2\phi)dV = 0. \tag{4.6}$$

With the divergence theorem, Eq.(4.6) becomes

$$\oint_{\mathrm{S}} \sigma(\nabla\phi) d\mathbf{S} = 0. \tag{4.7}$$

Eq.(4.7) can be approximated into a sum of integrals over all faces as,

$$\sum_{i=1}^{nb} \sigma(\nabla\phi)_{f_i} \mathbf{S}_i = 0 \tag{4.8}$$

where *nb* is the number of total surfaces which adjacent to considered control volume V_P which is equal to 4 in this study. $(\nabla\phi)_{fi}$ stands for variable gradient of face f_i .

If the surface vector, S_i, and displacement vector from point P to Q_i , $\mathbf{d}_i$, are parallel (Fig. 4.2). The value of surface gradient $(\nabla\phi)_{fi}$ in Eq.(4.8) could be approximated as

$$(\nabla\phi)_{f_i} \cdot \mathbf{S}_i \approx (\phi_{f_i} - \phi_P)\frac{|\mathbf{S}_i|}{|\mathbf{d}_i|}. \tag{4.9}$$

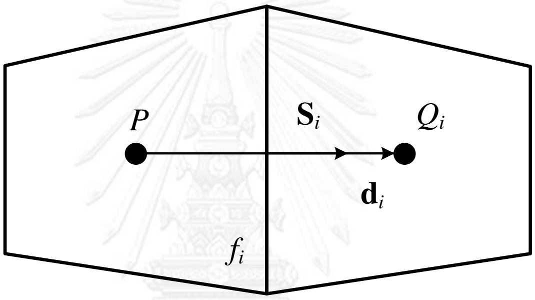

Fig. 4.2 A control volume with parallel vector $\mathbf{S}_i$ and $\mathbf{d}_i$

However, for an unstructured quadrilateral mesh, the vector $\mathbf{S}_i$ and displacement vector $\mathbf{d}_i$ in most control volumes are nonparallel (Fig. 4.3). To obtain more accurate result, the non-orthogonal correction is added [29]. The Eq.(4.9) becomes

$$(\nabla\phi)_{f_i} \cdot \mathbf{S}_i \approx (\phi_{Q_i} - \phi_P)\frac{|\mathbf{S}_i|}{|\mathbf{d}_i|} + (\nabla\phi)_f \cdot \left(\mathbf{S}_i - |\mathbf{S}_i|\frac{\mathbf{d}_i}{|\mathbf{d}_i|}\right). \tag{4.10}$$

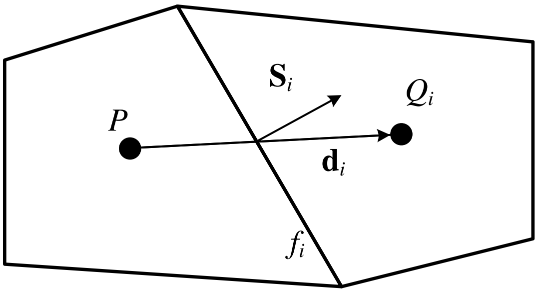

Fig. 4.3 A control volume with nonparallel vector $\mathbf{S}_i$ and $\mathbf{d}_i$

Substituting Eq.(4.10) into Eq.(4.8), the discretized equation is

$$\sum_{i=1}^{nb}\sigma(\phi_{Q_i}-\phi_P)\frac{|\mathbf{S}_i|}{|\mathbf{d}_i|}+\sum_{i=1}^{nb}\sigma(\nabla\phi)_{f_i}\cdot\left(\mathbf{S}_i-|\mathbf{S}_i|\frac{\mathbf{d}_i}{|\mathbf{d}_i|}\right)=0. \qquad (4.11)$$

4.2.3 Simultaneous Algebraic Equation

To determine the value of the primary unknowns ϕ at the central grid point, P, which is surrounded with neighbor control volume, Q_i, the resulting algebraic equation is arranged into a new form

$$a_P\phi_P=\sum_{i=1}^{nb}a_{Q_i}\phi_{Q_i}+b_\phi \qquad (4.12)$$

where a_P and a_{Qi} are the coefficients of ϕ_P and ϕ_{Qi} respectively and b_ϕ is the source term. By rearranging Eq.(4.11) into the form of Eq.(4.12), the coefficients definitions are

$$a_P=\sum_{i=1}^{nb}\sigma\frac{|\mathbf{S}_i|}{|\mathbf{d}_i|} \qquad (4.13)$$

$$a_{Q_i}=\sigma\frac{|\mathbf{S}_i|}{|\mathbf{d}_i|} \qquad (4.14)$$

and

$$b_\phi=\sum_{i=1}^{nb}\sigma(\nabla\phi)_{f_i}\left(\mathbf{S}_i-|\mathbf{S}_i|\frac{\mathbf{d}_i}{|\mathbf{d}_i|}\right). \qquad (4.15)$$

For each control volume, the values of a_P, a_{Qi} and b_ϕ of every individual cell are assembled into Eq.(4.12). Then, equations of all cells of domain form the system of algebraic equations which is used to determine and update the values of ϕ_P.

Typically, the value at a node inside the domain is the unknown variable. A discretized equation (4.12) can be written for every control volume. For example, the obtained algebraic equation of a control volume P in Fig. 4.4(a) is

$$a_P\phi_P=a_{Q_1}\phi_{Q_1}+a_{Q_2}\phi_{Q_2}+a_{Q_3}\phi_{Q_3}+a_{Q_4}\phi_{Q_4}+b_\phi \qquad (4.16)$$

where the coefficients can be determined from Eqs.(4.13) to (4.15).

4.3 Implementation of Boundary Conditions

For some control volumes of which some faces coincide with the domain boundary or the crack such as the control volume in Fig. 4.4(b), the algebraic equation of such boundary node is slightly different from the interior cells and depends on the specified boundary condition. In general, there are 2 main types of boundary conditions, Dirichlet or fixed value boundary condition and Neumann or fixed gradient boundary condition.

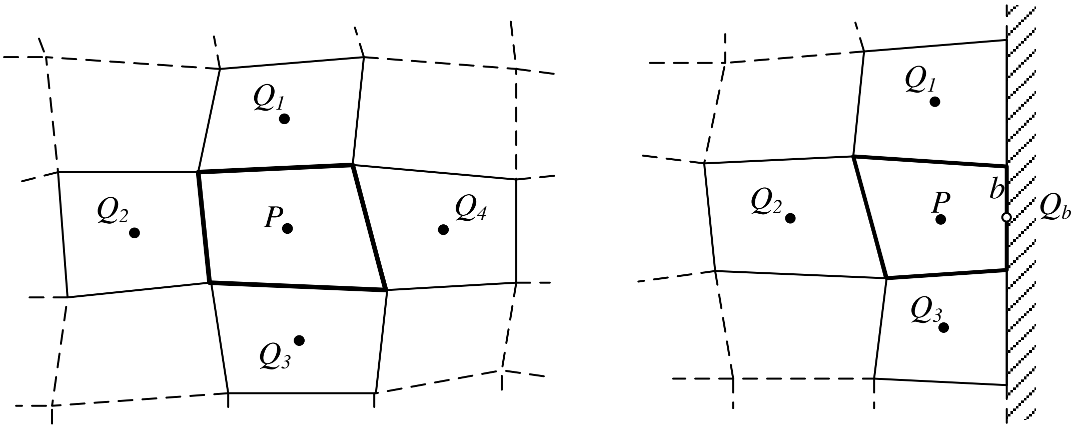

(a) (b)

Fig. 4.4 Types of control volumes: (a) internal control volume and (b) boundary control volume

4.3.1 Dirichlet Boundary Condition

This boundary condition prescribes the value of the unknown variable ϕ on the boundary node. If the value of variable at face b is given as ϕ_b, the algebraic equation of this control volume would be

$$a_P\phi_P = a_{Q_1}\phi_{Q_1} + a_{Q_2}\phi_{Q_2} + a_{Q_3}\phi_{Q_3} + a_b\phi_b + b_\phi \tag{4.17}$$

4.3.2 Neumann Boundary Condition

This boundary condition also known as the specified gradient boundary condition in which the gradient of variable, $\nabla\phi$, is defined for boundary node. Regarding to Fig. 4.4(b) with the gradient of variable at face b is $(\nabla\phi)_b$, this gradient value should be transformed into the value of unknown variable at face b, ϕ_b, by applying Eq.(4.1) as

$$\phi_b = \phi_P - (\nabla\phi)_b \cdot (\mathbf{r}_P - \mathbf{r}_b) \tag{4.18}$$

where $\mathbf{r}_b$ is the position vector at point b. Then, this value is taken to the algebraic equation as same as Dirichlet boundary condition.

4.4 Computational Procedure

To determine the distribution of electric potential, the domain of geometry and crack length must be defined. Then, the mesh for the studied domain is generated and the boundary condition, tolerance ε, and initial value of electric potential V are defined. With the discretized equation, the equations for every control volumes are set up. The Jacobi iteration method is utilized to solve the assembled equation system of the entire domain and after this process, a new value of V for every node is obtained.

These values are used to update the equation system for the calculation in the next iteration. This process continues until the percentage difference between the new value and the old value of V is less than the tolerance ε, which is equal to 0.000001% for this work, for every control volumes. The percentage difference is calculated by

$$\text{Percentage difference} = \frac{\left|V_{\text{NEW}} - V_{\text{OLD}}\right|}{\left(V_{\text{NEW}} + V_{\text{OLD}}\right)/2} \times 100\% \tag{4.19}$$

where V_{OLD} and V_{NEW} are the potential value before update and after update respectively. The detail of this process is illustrated in Fig. 4.5.

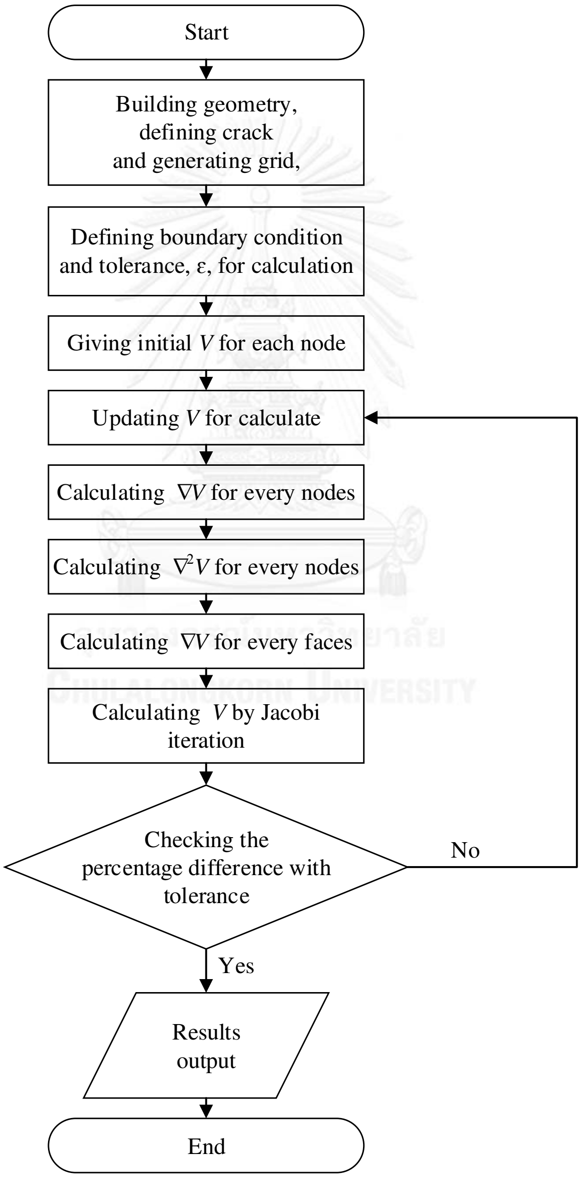

Fig. 4.5 Flowchart of calculating process

4.5 Conclusion

This chapter explains the procedure that transforms the governing equation in the form of partial differential equation into sets of algebraic equations by the finite volume technique. Taylor’s series approximation method in Eq.(4.1), a least square fit method in Eq.(4.2) and non-orthogonal correction technique in Eq.(4.10) are used to discretize the governing equation. This chapter also shows how to set up the equation for boundary node which is slightly difference from typical node. The different types of boundary conditions, Dirichlet and Neumann boundary conditions, affect directly to the obtained equation for each node. The final form of discretized equation is shown with the coefficient definitions in Eq.(4.12). The iterated process of calculation is explained and illustrated in detail with flowchart in the last part of the chapter.

Chapter 5

Program Verification

In general, a numerical computer program requires the verification procedure to check the accuracy of written code and quality of grid generating. Thus, the electric potential distribution problem within simple cracked plates, i.e. single edge cracked and central cracked specimens, are examined in this chapter. Then the calibration curves are calculated and compared against the analytical solutions and existing experimental data. Simulations with refining grids are also conducted in order to ensure that the obtained solution is grid independent.

5.1 Single Edge Cracked Specimen

The single edge crack and central crack are one of the most common crack types in fracture mechanics [6]. The test specimen is made from AISI 304 stainless steel which electric conductivity σ at 20°C is $1.39 \times 10^6\ \Omega^{-1}\cdot\text{m}^{-1}$ [34] with width W = 20 mm, length L = 100 mm and thickness t = 4 mm. The magnitude of electric current induced is constant throughout the specimen at 10 A. Fig. 5.1 shows the geometry of specimen with single edge crack type under constant electric current passing throughout the specimen where y represents the potential measured distance from crack. The boundary conditions are depicted in Fig. 5.2 which **J** represents the electric current density.

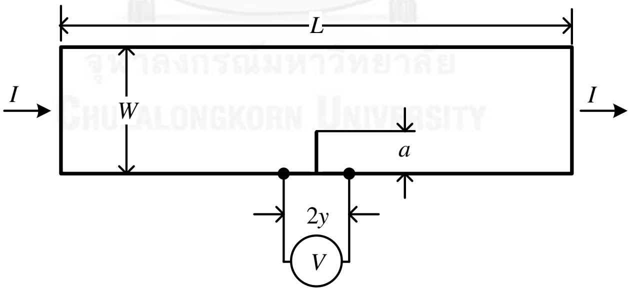

Fig. 5.1 Geometry of single edge cracked specimen under constant current

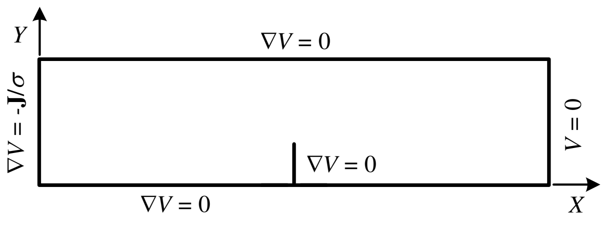

Fig. 5.2 Boundary conditions of single edge cracked specimen

The analytical calibration curve for both single edge cracked and central cracked specimen can be obtained from Johnson's equation [6].

$$\frac{V}{V_0}=\frac{\cosh^{-1}[\cosh(\pi y/2W)/\cos(\pi a/2W)]}{\cosh^{-1}[\cosh(\pi y/2W)/\cos(\pi a_0/2W)]} \tag{5.1}$$

where a_0 is the reference crack size which equals to zero for this thesis and V_0 represents the measured voltage corresponding to a_0. Eq.(5.*1*) can be used with any conductive materials if its electric resistivity is constant throughout the specimen. The magnitude of an electric current is independent from this analytical solution as well.

The process of grid independent test is shown in Appendix A. With the grid independent meshes, the results of electric potential *V* of every control volumes are used to draw the contour graph of electric potential distribution within cracked domain. The contour results of every crack length to specimen width ratio *a*/*W* are shown in Fig. 5.3 to Fig. 5.10.

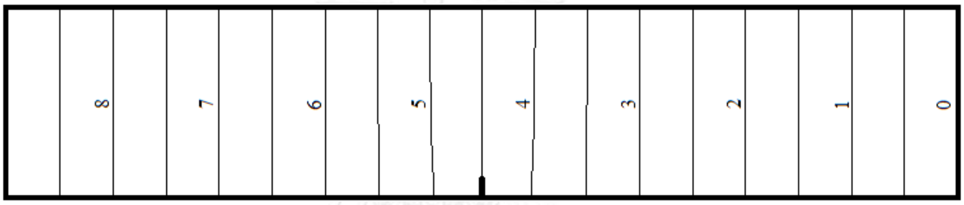

Fig. 5.3 The contour plot of potential distribution in the unit of millivolt (mV) in single edge cracked plane with crack length to specimen width ratio *a*/*W* = 0.1

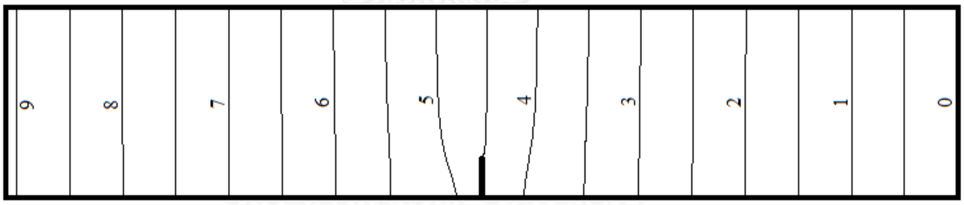

Fig. 5.4 The contour plot of potential distribution in the unit of millivolt (mV) in single edge cracked plane with crack length to specimen width ratio *a*/*W* = 0.2

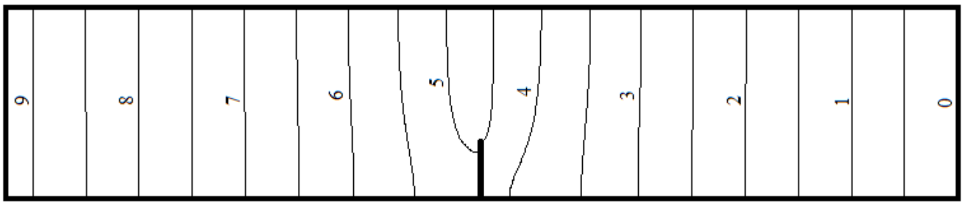

Fig. 5.5 The contour plot of potential distribution in the unit of millivolt (mV) in single edge cracked plane with crack length to specimen width ratio *a*/*W* = 0.3

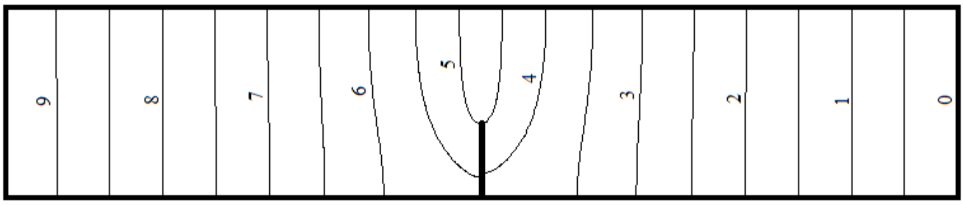

Fig. 5.6 The contour plot of potential distribution in the unit of millivolt (mV) in single edge cracked plane with crack length to specimen width ratio $a/W = 0.4$

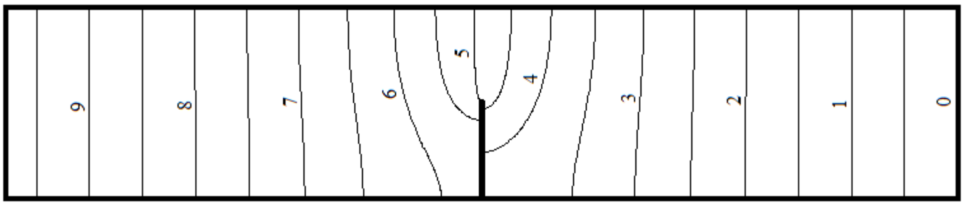

Fig. 5.7 The contour plot of potential distribution in the unit of millivolt (mV) in single edge cracked plane with crack length to specimen width ratio $a/W = 0.5$

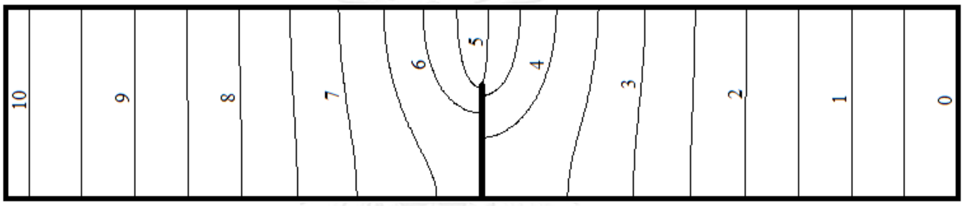

Fig. 5.8 The contour plot of potential distribution in the unit of millivolt (mV) in single edge cracked plane with crack length to specimen width ratio $a/W = 0.6$

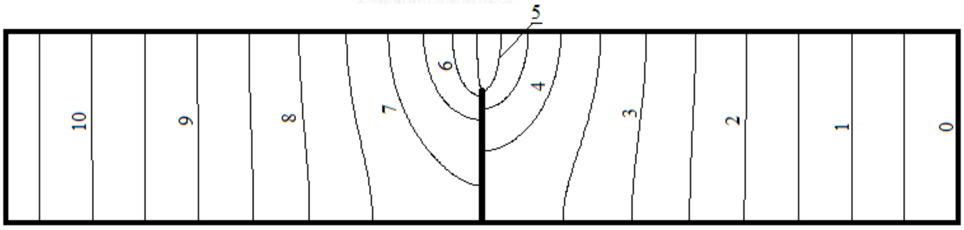

Fig. 5.9 The contour plot of potential distribution in the unit of millivolt (mV) in single edge cracked plane with crack length to specimen width ratio $a/W = 0.7$

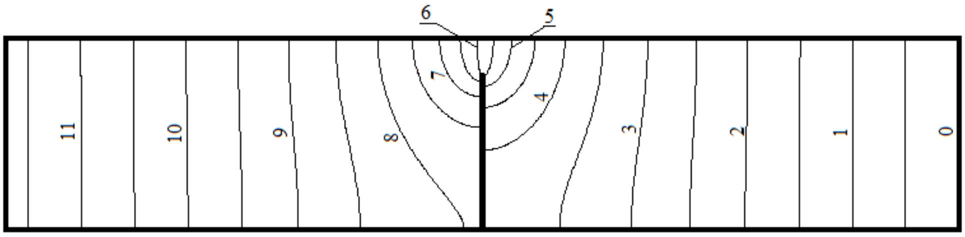

Fig. 5.10 The contour plot of potential distribution in the unit of millivolt (mV) in single edge cracked plane with crack length to specimen width ratio $a/W = 0.8$

The numerical calibration curves are plotted and compared with the analytical solution in Fig. 5.11. The distance of potential calculated position from crack y, is varied from $y = 5$ mm to 25 mm in order to verify the calibration curves and examine the changes of potential drop due to the extension of crack at different measured positions. The data of these calibration curves including to number of grids used are listed in Table A.1 to Table A.5 in Appendix A. The detail of percentage error for every potential calculated position at different crack size is illustrated in Fig. 5.12.

Fig. 5.11 shows that the slope of calibration curve is relatively high while the potential calculated point is near the crack, but it is flatter when the calculated position is farther apart. That is, the sensitivity, the ability to distinguish the small changes in crack length, is higher when the potential calculated points are closer to the crack.

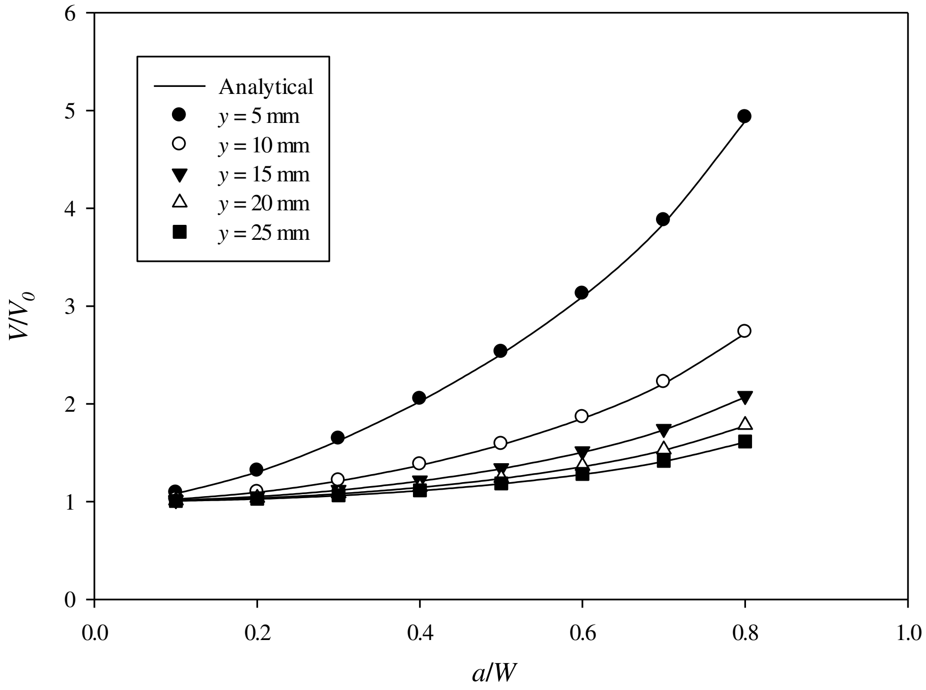

Fig. 5.11 Calibration curve of single edge cracked specimen with various potential calculated position

There is another observation in terms of percentage error in Fig. 5.12. When the potential calculated position is nearer to the crack (e.g. $y = 5$ mm), the percentage error of the numerical results raise to 0.82 – 1.15%. If y increases, the percentage error obviously reduces. At $y = 25$ mm, for example, it remains just only 0.07 – 0.62%.

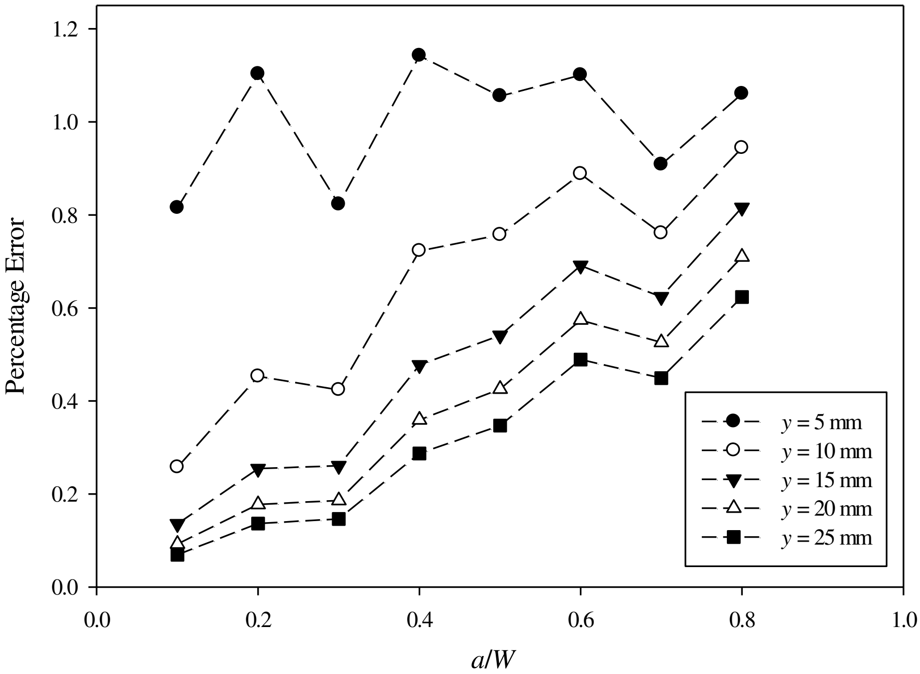

Fig. 5.12 Percentage errors of numerical calibration curve of single edge cracked specimen compared to Johnson's equation

The finite volume solutions compared to the other experimental solutions [6] are shown in Fig. 5.13. This experiment is conducted with 5 mm thickness and 50 mm width specimen. The initial value of crack length a_0 is 10 mm. The potential measured probe distance from crack y is 10 mm.

The calibration curve in Fig. 5.13 shows that the finite volume solution conforms very well with the analytical solution and lies consistently below the experimental normalized potential. The difference between numerical and experimental result grows with the increasing of crack length.

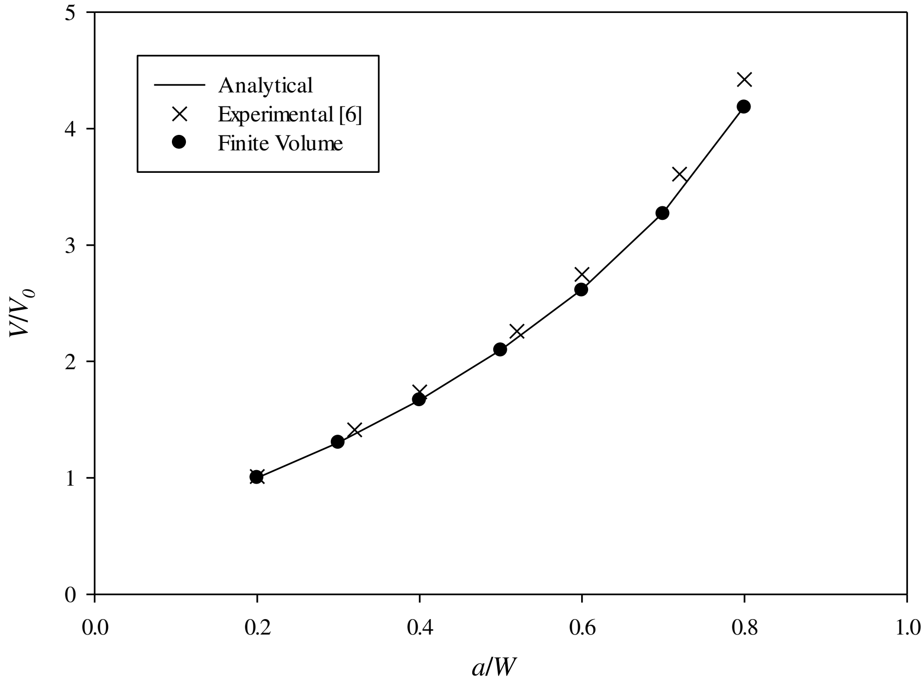

Fig. 5.13 The numerical calibration curve for single edge cracked specimens compared with the experiments [6]

5.2 Central Cracked Specimen

The central crack type is another common type of fracture appearance. The geometry and boundary conditions of central cracked specimen with the uniform current introduced at two ends is shown in Fig. 5.14 and Fig. 5.15, respectively. The studied specimen's size is W = 20 mm and L = 80 mm with the same thickness and material as the studied single edge crack specimen. The analytical calibration curve also can be calculated by Johnson's equation.

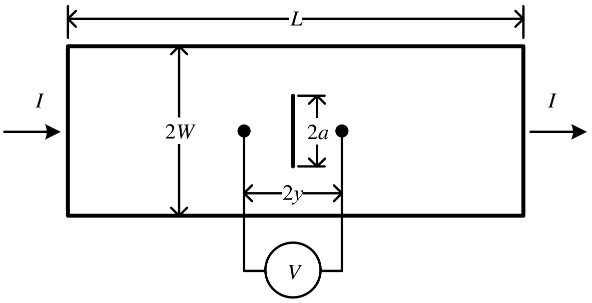

Fig. 5.14 The geometry of central cracked specimen under constant current

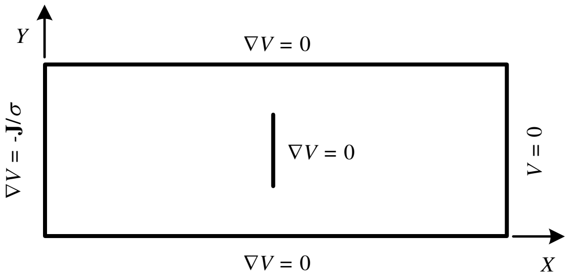

Fig. 5.15 Boundary conditions of central cracked specimen

After the process of grid independent test which is shown in Appendix A, the obtain contour results of electric potential distribution within central cracked domain for every crack length to specimen width ratio *a*/*W* are shown in Fig. 5.16 to Fig. 5.23.

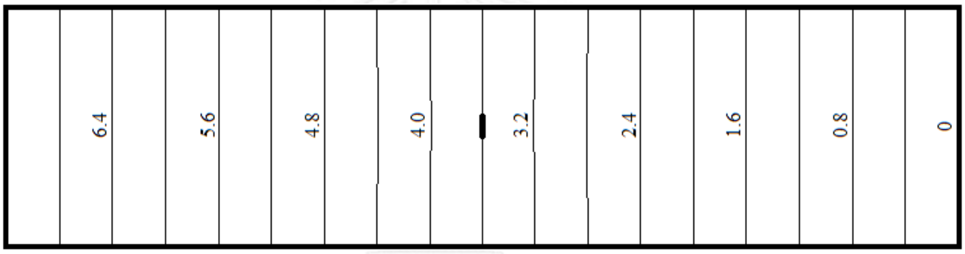

Fig. 5.16 The contour plot of potential distribution in the unit of millivolt (mV) in central cracked plane with crack length to specimen width ratio *a*/*W* = 0.1

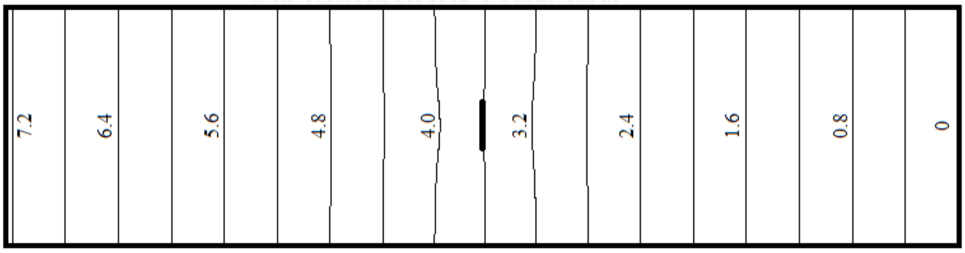

Fig. 5.17 The contour plot of potential distribution in the unit of millivolt (mV) in central cracked plane with crack length to specimen width ratio *a*/*W* = 0.2

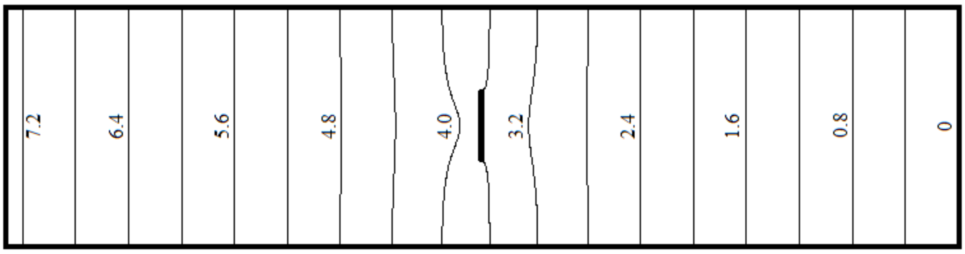

Fig. 5.18 The contour plot of potential distribution in the unit of millivolt (mV) in central cracked plane with crack length to specimen width ratio *a*/*W* = 0.3

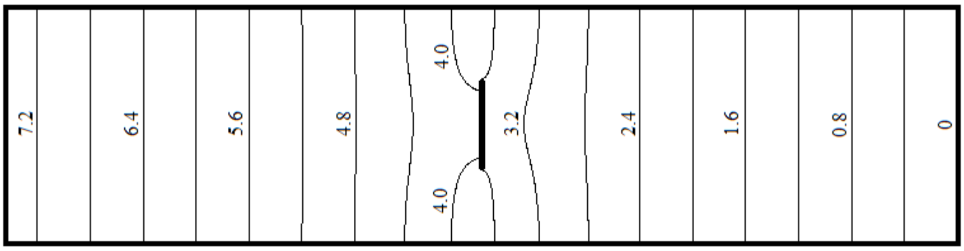

Fig. 5.19 The contour plot of potential distribution in the unit of millivolt (mV) in central cracked plane with crack length to specimen width ratio *a*/*W* = 0.4

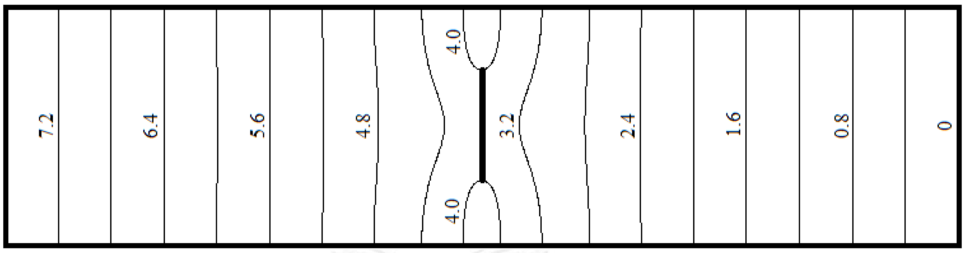

Fig. 5.20 The contour plot of potential distribution in the unit of millivolt (mV) in central cracked plane with crack length to specimen width ratio *a*/*W* = 0.5

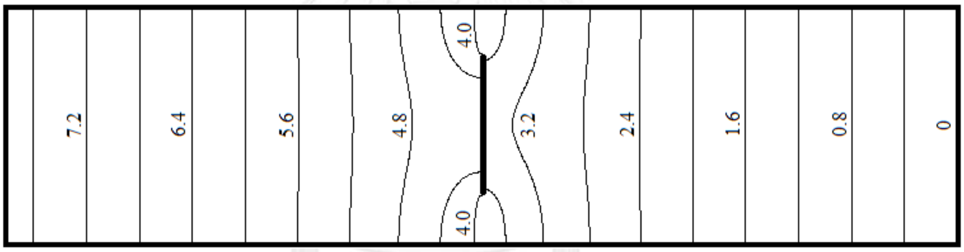

Fig. 5.21 The contour plot of potential distribution in the unit of millivolt (mV) in central cracked plane with crack length to specimen width ratio *a*/*W* = 0.6

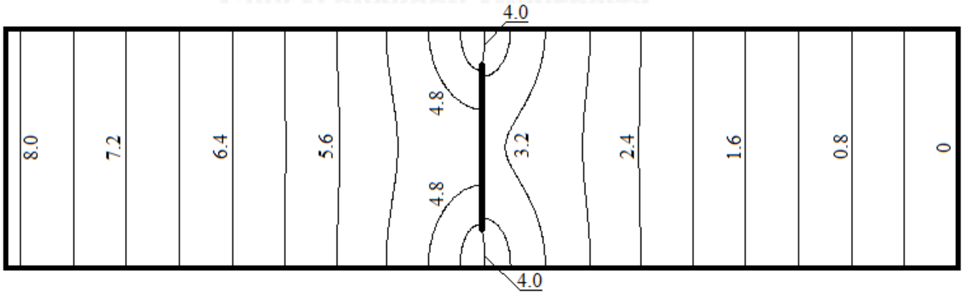

Fig. 5.22 The contour plot of potential distribution in the unit of millivolt (mV) in central cracked plane with crack length to specimen width ratio *a*/*W* = 0.7

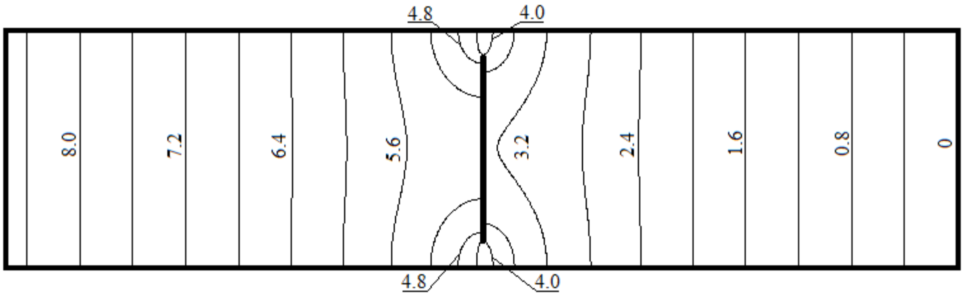

Fig. 5.23 The contour plot of potential distribution in the unit of millivolt (mV) in central cracked plane with crack length to specimen width ratio $a/W = 0.8$

The numerical calibration curves at calculated distance from crack $y = 4$ mm to $y = 20$ mm compared with Johnson's equation are shown in Fig. 5.24 while the percentage error is illustrated in Fig. 5.25. The data of calibration curve is concluded in Table A.6 to Table A.10.

Similarly to the single edge crack results, the finite volume method also provides the consistent prediction for this crack type. The percentage error is highest when $y = 4$ mm, the closest potential calculated position to the crack origin. The error at this calculated point is 0.60 – 1.69%. When the potential calculated points move away from crack, especially at $y = 20$ mm which is the farthest potential calculated distance, more accuracy results are obtain with the percentage error of 0.07 – 0.77%. However, there is minimum sensitivity at this measured point as well.

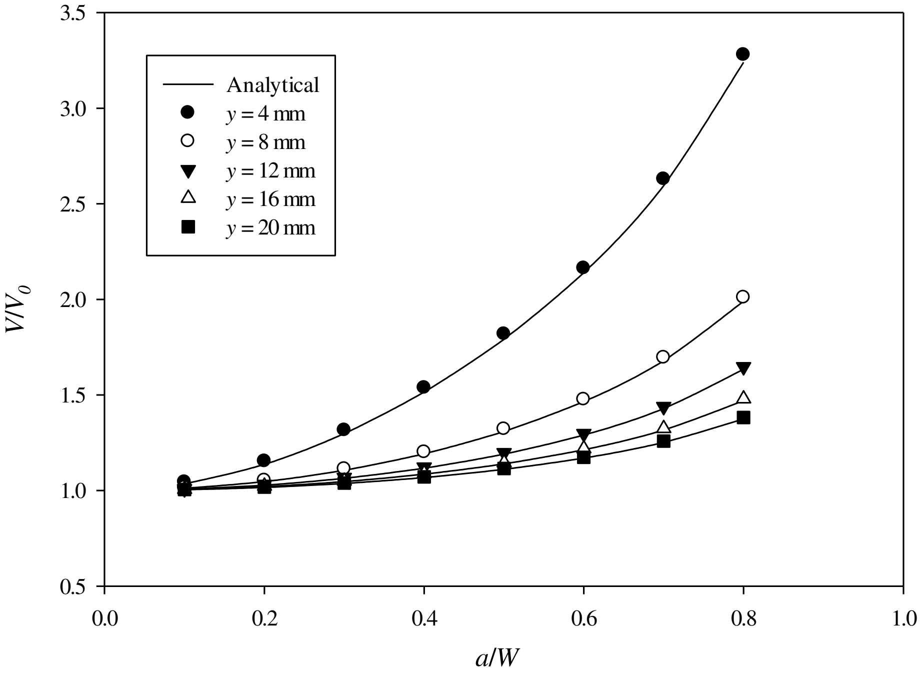

Fig. 5.24 Calibration curves of central cracked specimens with various distance of potential calculated position

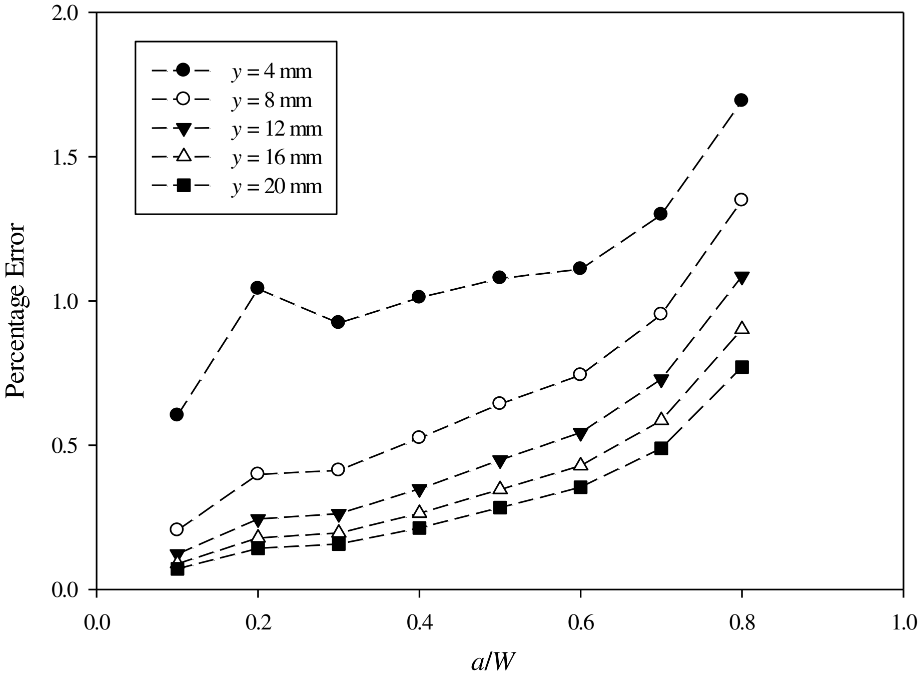

Fig. 5.25 Percentage errors of numerical calibration curve of central cracked specimen compared to Johnson's equation

Comparison of finite volume solution with the experimental solution [6] is displayed in Fig. 5.26. This experiment is conducted with 2 mm thickness and 300 mm width specimen. The initial value of central crack length $2a_0$ is 30 mm. The potential measured probe distance from crack y is 9 mm.

There is slight error between numerical and analytical solution because the potential calculated position is very near to the crack compared with specimen's size. However, there is more difference between numerical or analytical solution and the experimental solution. This gap is larger while crack size increases.

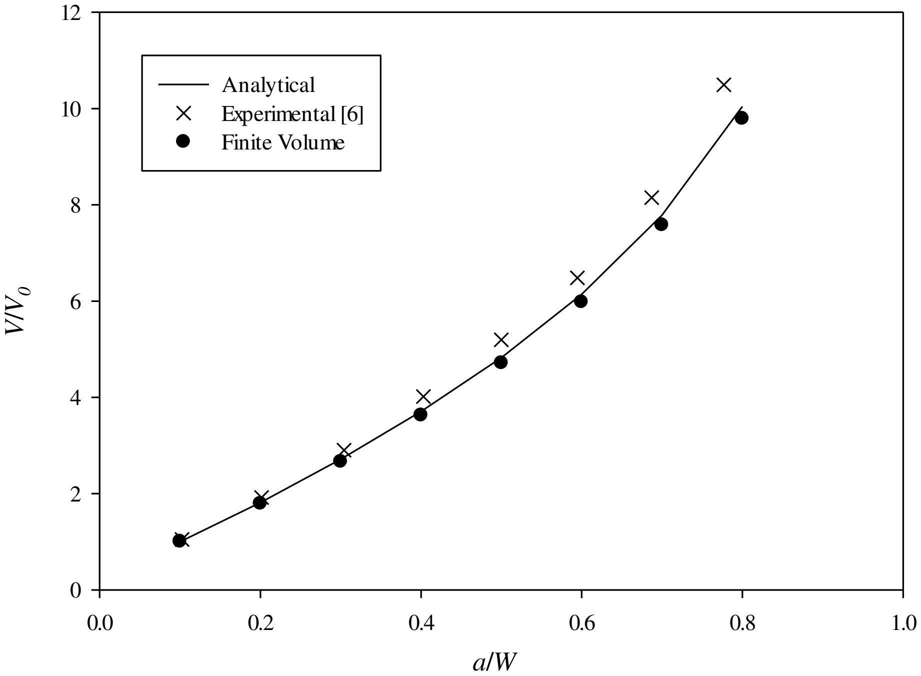

Fig. 5.26 The numerical calibration curves for central cracked specimens compared with the experiments [6]

5.3 Discussion

The finite volume results obtained in this chapter proves that the finite volume method is a convenient, inexpensive and reliable way to solve the distribution of electric potential in basic cracked plane problems. Finite volume also can establish a reasonable calibration curve for basic crack compared with the analytical calibration curve.

However, there are same differences between the numerical calibration curve and experimental data as shown in Fig. 5.13 and Fig. 5.26. For the experiment, the plastic deformation occurs around crack tip in specimen under load. The crack tip plasticity affects locally to the change of electric resistivity and hence alters the potential drop across the crack.

The study the effect of the plastic deformation on the calibration curves is the interesting topic for the future work. The electric distribution problem within the material which the electric resistivity is not constant throughout specimen should be considered as nonlinear problems. By developing this program to solve nonlinear problems, the effect of plasticity on the change of calibration curve can be achieved.

5.4 Conclusions

This chapter defined the basic crack problems to verify the written program. The distribution of electric potential within single edge cracked and central cracked specimens are examined and, then, used to calculate the calibration curves compared with the analytical calibration curves. The other experimental solutions are also used to verify the numerical results.

With the grid independent meshes, the calibration curve is generated. The numerical results are compared with the analytical solution. With crack length to specimen width ratio a/W from 0.1 to 0.8 intervals, the numerical calibration curves are very close to the analytical results with the error of 0.82 – 1.15% for the nearest potential measured position to crack $y = 5$ mm in the single edge cracked specimen and with the error of 0.60 – 1.69% for the nearest potential measured position to crack $y = 4$ mm in the central cracked specimen.

The finite volume solution also conforms well with the other experimental solution although there is slight difference due to the plastic deformation in experiment process. Thus, it can be concluded that the finite volume method can be utilized to calculate the reliable calibration curve for basic cracked specimen.

Chapter 6

Inclined Edge Crack Characterization

Characterization of an inclined edge crack is more complicate than the crack problem discussed in chapter 5 because not only the length but also its inclination angle must be found. This chapter presents the methodology to identify the characteristic of this crack type. The finite volume method is employed to simulate the electric potential distribution within a single edged inclined cracked specimen with different inclination angle and length. Then, the calibration curves, based on the proposed methodology, are established. Finally, two case studies of inclined edge crack characterization are presented in order to verify the proposed characterization methodology.

6.1 Concept of Inclined Crack Calibration

Fig. 6.1 shows an inclined edge cracked plate with a crack length *a* and angle of inclination θ to the vertical line. The positive angle of θ is measured clockwise. The boundary conditions are depicted in Fig. 6.2 in which the normal potential gradient on inclined crack faces is zero.

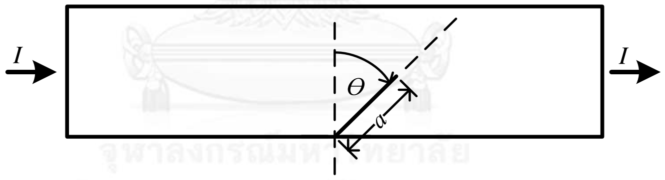

Fig. 6.1 Inclined edge cracked specimen under constant current

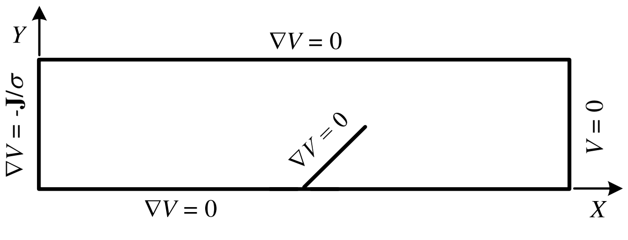

Fig. 6.2 Boundary conditions of inclined edge cracked specimen

The crack angle θ affects the change of electric potential drop across the crack resulting in the calibration curve as shown in Fig. 6.3. At the same crack size, the potential difference across the crack is lower while the inclination angle θ becomes larger. However, this single set of calibration curve is insufficient to find 2 unknowns, i.e. length *a* and inclination angle *θ*. Thus, an additional set of calibration curve is needed.

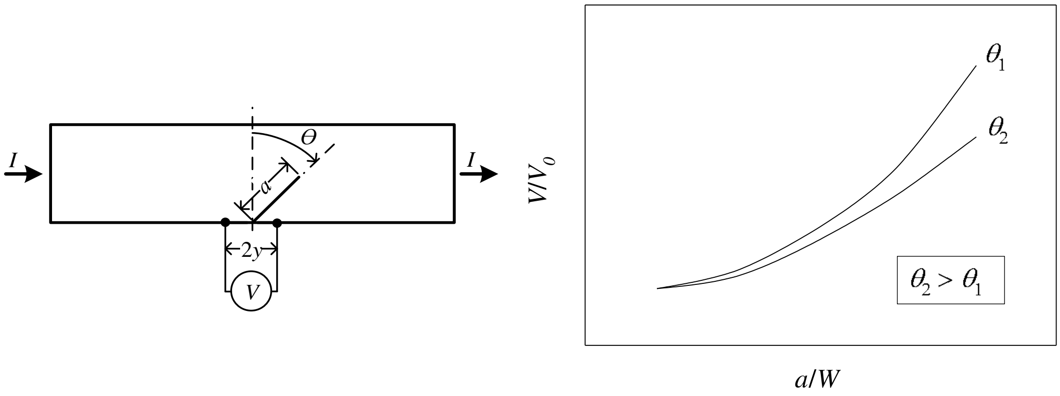

Fig. 6.3 The effect of inclined angle θ on the calibration curve

In order to find the additional potential measured positions, the potential at different positions within the uncracked, single edge cracked and inclined cracked specimens were examined first.

Within an uncracked plate, the potential ratio at any positions, V/V_0 is equal to 1. Fig. 6.4 illustrates this behavior. The potential V_1 to V_7 are measured at the average potential probes positions $\bar{X}_1$ to $\bar{X}_7$ respectively. The ratios of V_1/V_0 to V_7/V_0 are equal to 1 along this boundary.

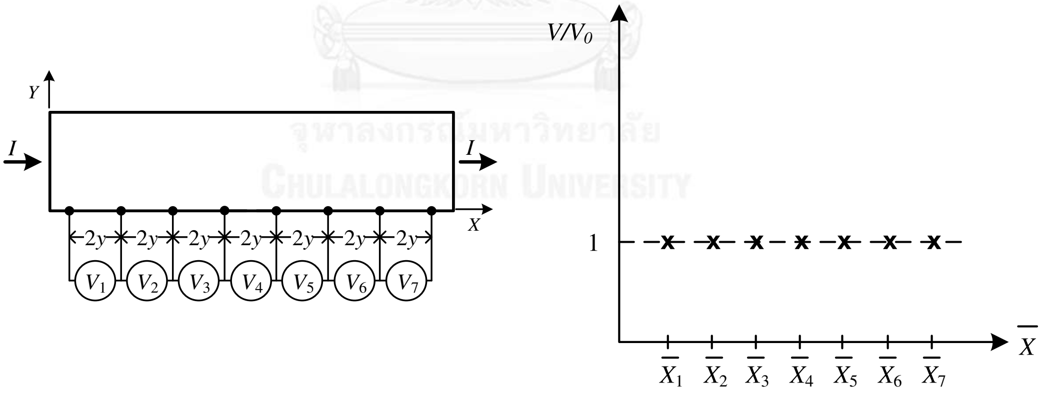

Fig. 6.4 Examination of potential different along
lower boundary of an uncracked body

Fig. 6.5 shows the case of single edge cracked specimen with a crack size a_1. In this figure, the potential ratio gradually decreases from 1 as the probe approaches a crack, then suddenly increases and reaches the maximum value as the probe symmetrically across the crack position. After that, the potential ratio suddenly drops and gradually increases to unity as the probe moves away from the crack.

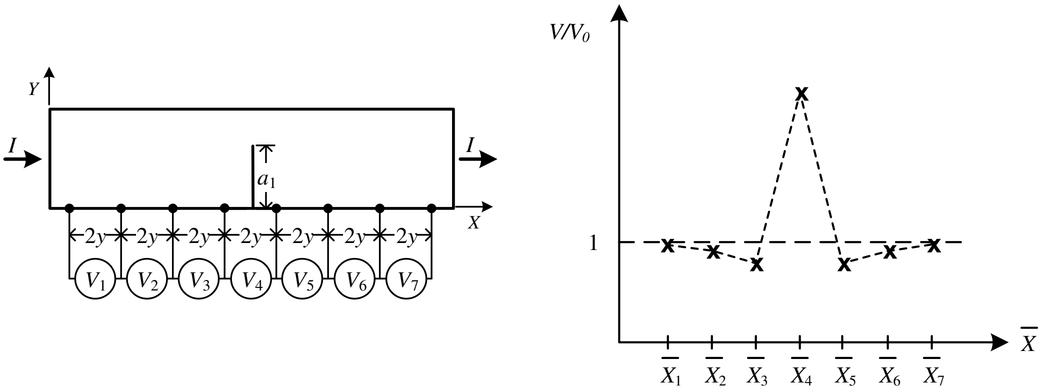

Fig. 6.5 Examination of potential different along
lower boundary of single edge cracked material

The behavior of a potential ratio for an inclined edge cracked specimen is illustrated in Fig. 6.6. The normalized potential across the crack mouth, V_4/V_0, is lower than that in the case of a single edge crack having the same crack length. It is interesting to note that the normalized potential at the positions adjacent to that symmetrically across the crack mouth, i.e. V_3/V_0 and V_5/V_0, are unsymmetrical. Therefore, it is worth to observe the effect of crack length and inclination angle on the potential ratio at these adjacent positions, i.e. V_3/V_5. If correlation does exist, it will be an additional set of calibration curve.

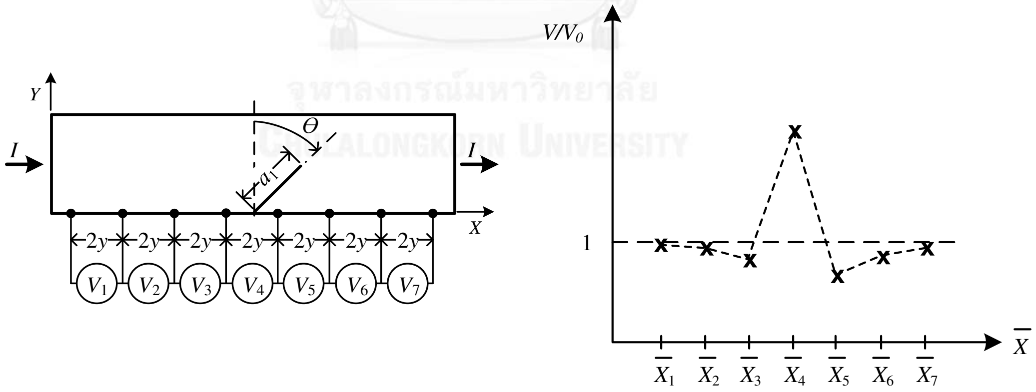

Fig. 6.6 Examination of potential different along
lower boundary of inclined edge cracked material

For convenience, the potential across the crack V_4 is replaced by V_C. The potential difference next to V_C on the left (V_3) and right (V_5) are represented as V_L and V_R, respectively. It will be shown later that the adjacent potential ratio V_L/V_R correlates with the crack length a and inclination angle θ as schematically shown in Fig. 6.7. When a crack angle θ is zero, this ratio is equal to 1 for any crack sizes. Thus, by employing the calibration curve of the normalized potential across the crack

V_C/V_0 at different inclination angles θ in Fig. 6.3 and the calibration curve of the adjacent potential ratio V_L/V_R at various crack angle θ in Fig. 6.7, the crack size a and the inclination angle θ of inclined edge crack can be determined.

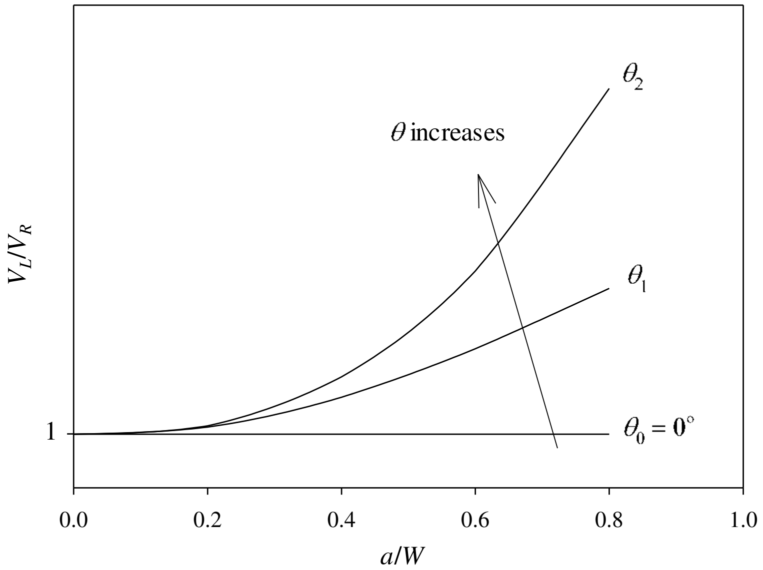

Fig. 6.7 The relationship between the adjacent potential ratio V_L/V_R and crack length to width ratio a/W at different inclined angle θ

The procedure to characterize an inclined edge crack begins with measuring the potential difference V_C, V_L and V_R as shown in Fig. 6.8. Next, V_C/V_0 and V_L/V_R are computed and determined the corresponding values of a/W and θ, i.e. intersection points, from calibration curves in Fig. 6.3 and Fig. 6.7, respectively. Then, the corresponding values of a/W and θ from each curve are plotted on the same graph and a best fit curve is determined. Finally, the intersection of best fit curves is obtained. This point represents the information of an inclined edge crack. This procedure is concluded in Fig. 6.9.

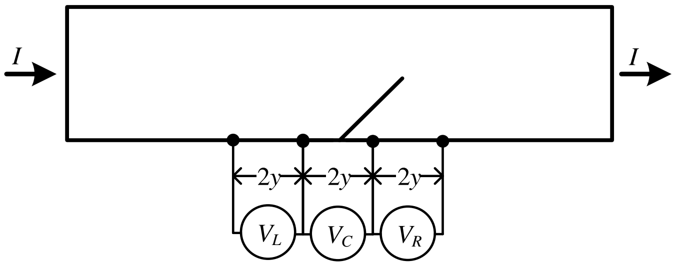

Fig. 6.8 Potential measured positions for inclined edge cracked identification

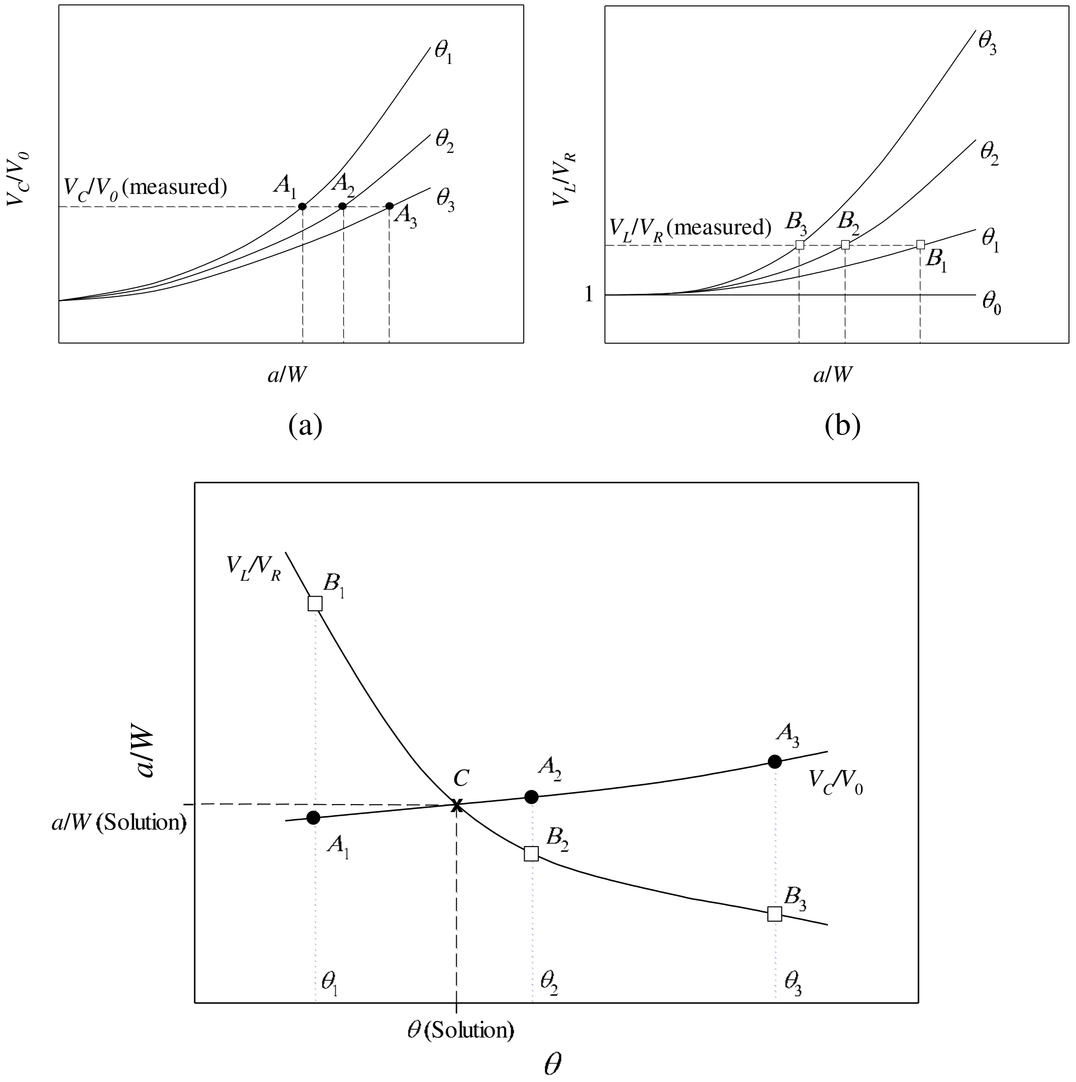

(a) (b)

(c)

Fig. 6.9 Methodology to identify inclined crack a/W and θ from (a) V_C/V_0 and (b) V_L/V_R and (c) the intersection finding process

6.2 Numerical Result

The test specimen is made from AISI 304 stainless steel with specimen's width W = 20 mm, length L = 100 mm and thickness t = 4 mm same as the studied single edge cracked specimen in chapter 5 including to the magnitude of electric current. The finite volume method is employed to determine the potential distribution within inclined edge cracked specimen with crack length to specimen width ratio a/W from 0.1 to 0.8 at 0.1 intervals and cracked angle θ from 7.5° to 45° at 7.5° intervals.

The calibration curves of the normalized potential across the crack V_C/V_0 and the calibration curves of the adjacent potential ratio V_L/V_R are calculated. The potential measured distance from the crack, y, used to calculate those curves is 5 mm according to the results of the sensitivity of single edge crack calibration curve from the last chapter.

6.2.1 Potential Distribution

Examples of electric distribution within inclined edge cracked specimen with crack length to specimen width ratio *a*/*W* 0.8 at various inclined angles are shown as contour plots in Fig. 6.10. These contours show the effect of crack angle θ on the potential distribution within a specimen.

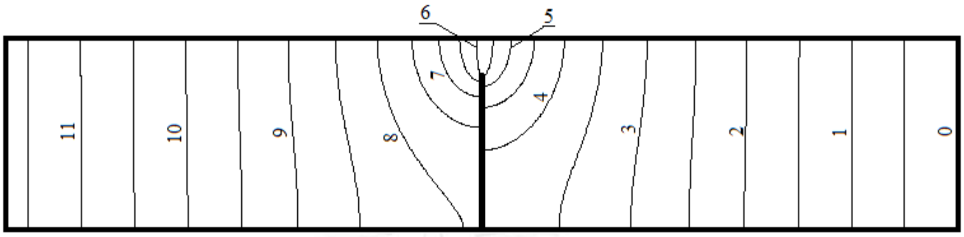

(a) $\theta = 0°$

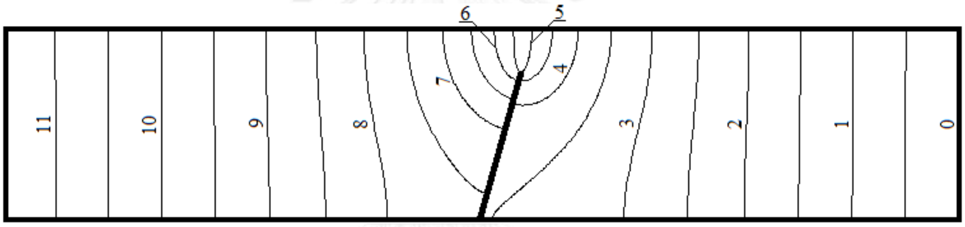

(b) $\theta = 15°$

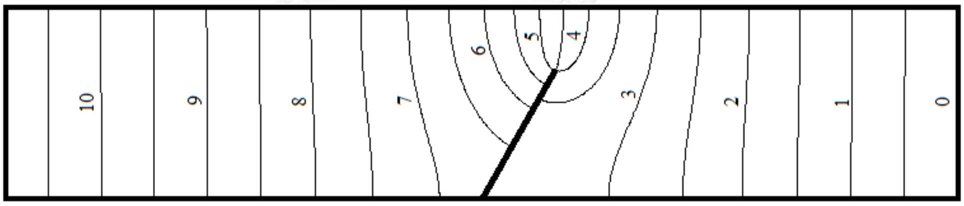

(c) $\theta = 30°$

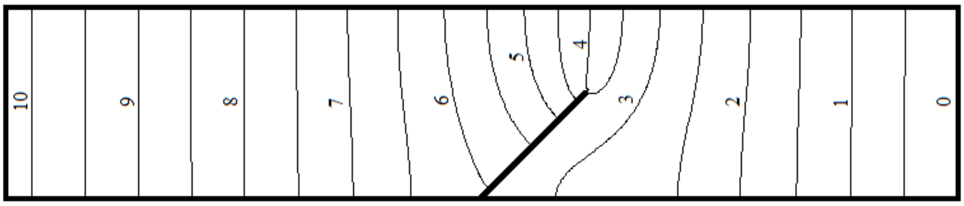

(d) $\theta = 45°$

Fig. 6.10 The potential distribution in the unit of millivolt (mV)
in inclined edge cracked plane with *a*/*W* = 0.8 and θ from 0 to 45°

6.2.2 Calibration Curve

The calibration curves of the normalized potential across the crack V_C/V_0 and the adjacent potential ratio V_L/V_R are shown in Fig. 6.11 and Fig. 6.12 respectively while the details data from the finite volume simulation is shown in Appendix B. According to ASTM E647-08 [20], the relationship between of the normalized potential across the crack V_C/V_0 and the crack length to specimen width ratio *a*/*W* can be established by polynomial interpolation. Thus, the calibration curve of each case is represented by fourth-order polynomial equations. The calibration curves of normalized potential across the crack V_C/V_0 is shown in Eq.(6.1) while the curves of the adjacent potential ratio V_L/V_R is given in Eq.(6.2). The coefficients for those equations at different crack angles θ are shown in Table 6.1 and Table 6.2.

According to the research by Spitas *et al.* [14] which the authors considered a short crack, it was concluded that the potential drop across the crack between point *L* and *R* in their specific specimen (Fig. 2.6) depends only from the crack size and not the orientation of the crack. However the numerical calibration curves of the normalized potential across the inclined crack V_C/V_0 at different degree levels in Fig. 6.11 indicates that the orientation of the crack also effects the potential drop across the crack, especially for longer crack length to specimen width ratio *a*/*W* more than 0.4.

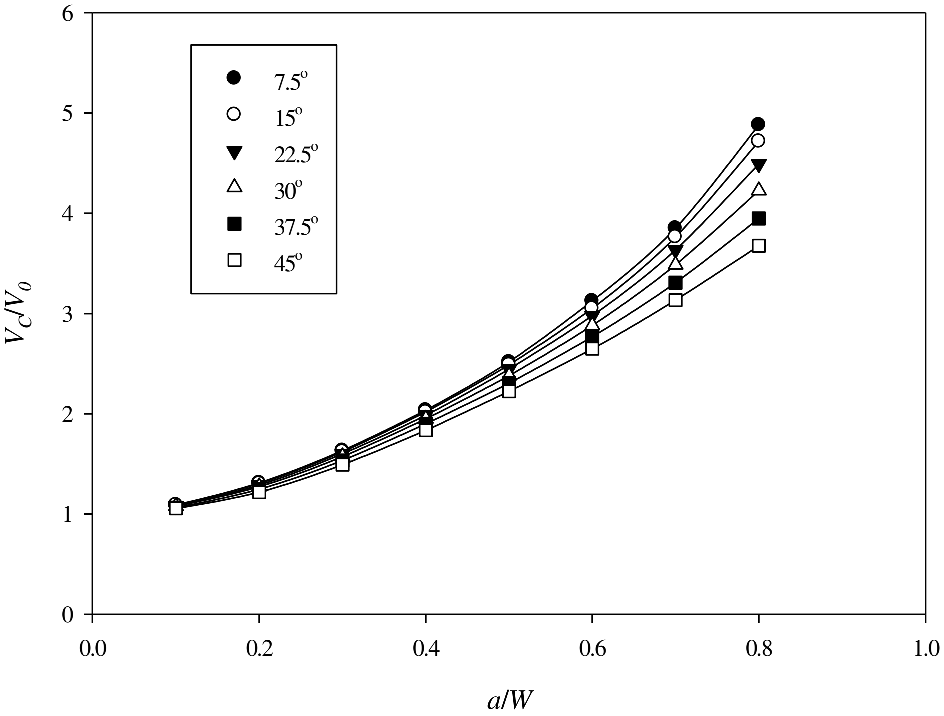

Fig. 6.11 Calibration curves of inclined cracked specimens of the normalized potential across the crack V_C/V_0

$$\frac{V_C}{V_0}=C_4\left(\frac{a}{W}\right)^4+C_3\left(\frac{a}{W}\right)^3+C_2\left(\frac{a}{W}\right)^2+C_1\left(\frac{a}{W}\right)+C_0 \tag{6.1}$$

Table 6.1 Coefficients of the calibration curve of the normalized potential across the crack V_C/V_0 in Eq.(6.1) at various crack angles θ.

θ	C_4	C_3	C_2	C_1	C_0
7.5°	12.971	-18.381	13.299	-0.725	1.045
15°	12.443	-18.167	13.282	-0.791	1.054
22.5°	10.608	-16.252	12.485	-0.705	1.040
30°	8.104	-13.278	11.145	-0.578	1.036
37.5°	7.450	-13.330	11.389	-0.755	1.037
45°	6.145	-12.319	11.215	-0.950	1.049

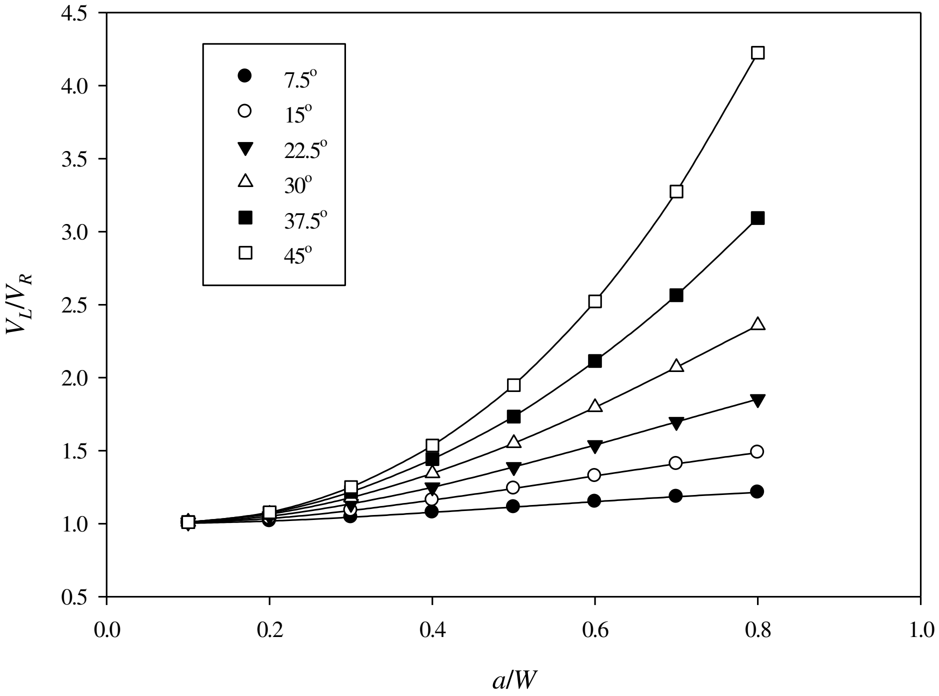

Fig. 6.12 Calibration curves of inclined cracked specimens of the adjacent potential ratio V_L/V_R

$$\frac{V_L}{V_R} = D_4\left(\frac{a}{W}\right)^4 + D_3\left(\frac{a}{W}\right)^3 + D_2\left(\frac{a}{W}\right)^2 + D_1\left(\frac{a}{W}\right) + D_0 \tag{6.2}$$

Table 6.2 Coefficient of the calibration curves of the adjacent potential ratio V_L/V_R in Eq.(6.2) at various crack angles θ.

θ	D_4	D_3	D_2	D_1	D_0
7.5°	0.260	-0.989	1.096	-0.114	1.005
15°	0.408	-1.758	2.204	-0.252	1.011
22.5°	0.098	-1.574	2.925	-0.335	1.014
30°	-0.593	-0.292	3.175	-0.373	1.017
37.5°	0.127	-0.289	4.092	-0.569	1.027
45°	0.784	2.061	3.463	-0.485	1.021

6.3 Validation of Crack Characterization Methodology

In this section, case studies are presented to show the applicability of a methodology described in a section 6.1. The specimen is made from AISI 304 stainless steel with width $W = 20$ mm, length $L = 100$ mm and thickness $t = 4$ mm with 10A constant current induced throughout the specimen.

For the first case, the specimen has an inclined crack with length to specimen width ratio $a/W = 0.55$ and inclined angle $\theta = 40°$. With finite volume method, the potential distribution is obtained as shown in Fig. 6.13. The potential differences V_C, V_L and V_R with a distance $2y$ of 10 mm are calculated. The V_C/V_0 and V_L/V_R from the computational results are 2.492 and 2.007 respectively.

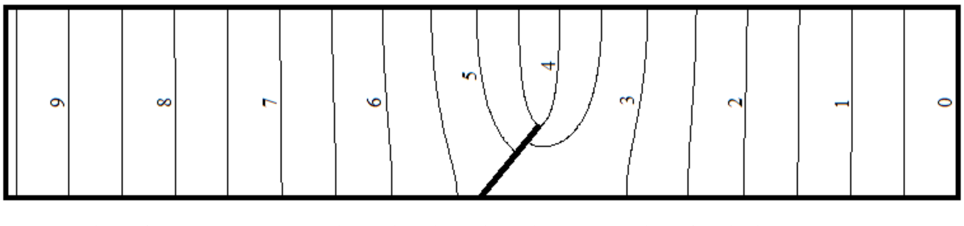

Fig. 6.13 The potential distribution in the unit of millivolt (mV) in inclined edge cracked plane with $a/W = 0.55$ and $\theta = 40°$

The values of V_C/V_0 and V_L/V_R are used to characterize the crack using the calibration curves in as shown Fig. 6.11 and Fig. 6.12, respectively. The obtained coordinate of a/W and θ are listed in Table 6.3.

Table 6.3 The obtained coordinates of crack length to specimen width ratio *a*/*W* and cracked angle θ from the calibration curves of V_C/V_0 and V_L/V_R for first case study

θ	*a*/*W*	
	V_C/V_0	V_L/V_R
7.5°	0.4946	-
15.0°	0.5011	-
22.5°	0.5103	-
30.0°	0.5236	0.6778
37.5°	0.5415	0.5740
45.0°	0.5638	0.5114

The value of *a*/*W* and θ from the calibration curve of V_C/V_0 can be fitted to fourth-order polynomial equation as

$$\frac{a}{W} = -1.119\times10^{-8}\theta^4 + 1.386\times10^{-6}\theta^3 - 2.253\times10^{-5}\theta^2 + 8.969\times10^{-4}\theta + 4.886 \qquad (6.3)$$

At the value of $V_L/V_R = 2.007$, only 3 coordinates of *a*/*W* and θ can be found out by the calibration curves in Fig. 6.12. Thus, the curve of V_L/V_R is represented by second-order polynomial equation as

$$\frac{a}{W} = 3.660\times10^{-4}\theta^2 - 3.854\times10^{-2}\theta + 1.505 \qquad (6.4)$$

By solving Eq.(6.3) and Eq.(6.4), the intersection in Fig.6.14 is obtained at $a/W = 0.5486$ and $\theta = 40.04°$. That is, the percentage error of the obtained *a*/*W* and θ are 0.11 and 0.25 respectively.

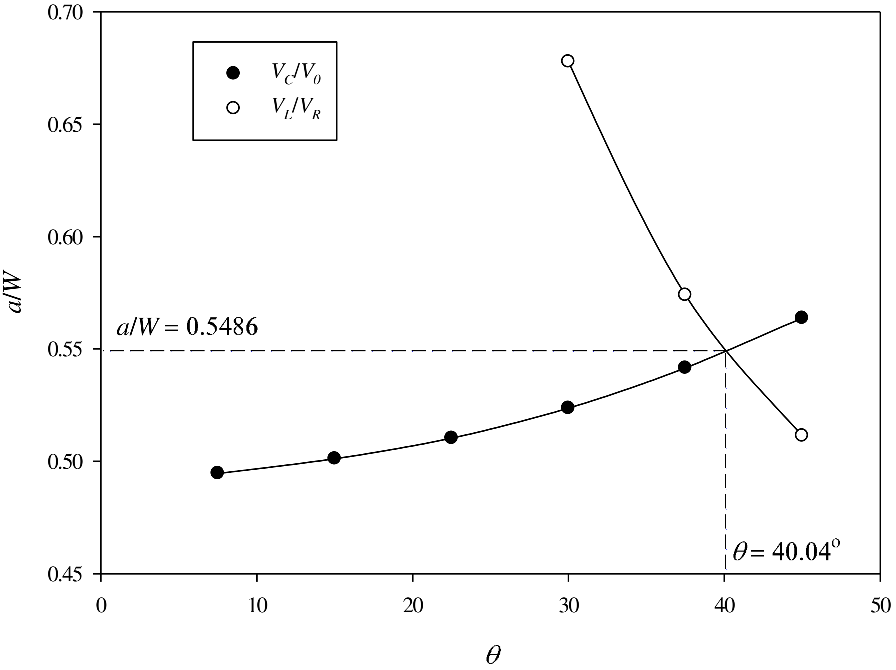

Fig.6.14 The relationship between a/W and θ from the calibration curve of V_C/V_0 and V_L/V_R for first case study

For the second case study, the inclined crack with crack size to specimen width ratio a/W = 0.35 and inclined angle θ = 10°. The numerical potential distribution result is shown in Fig.6.15. The calculated V_C/V_0 and V_L/V_R are 1.818 and 1.081 respectively.

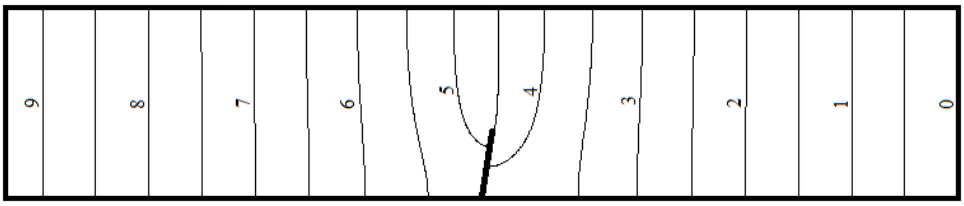

Fig.6.15 The potential distribution in the unit of millivolt (mV) in inclined edge cracked plane with a/W = 0.35 and θ = 10°

The obtained coordinates of a/W and θ are listed in Table 6.4 after the calibrating process with their calibration curves in Fig. 6.11 and Fig. 6.12.

Table 6.4 The obtained coordinates of crack length to specimen width ratio *a*/*W* and cracked angle θ from the calibration curves of V_C/V_0 and V_L/V_R for second case study

θ	*a*/*W*	
	V_C/V_0	V_L/V_R
7.5°	0.3479	0.4097
15.0°	0.3515	0.2861
22.5°	0.3583	0.2404
30.0°	0.3677	0.2162
37.5°	0.3799	0.2063
45.0°	0.3961	0.2010

The value of *a*/*W* and θ from the calibration curve of V_C/V_0 can be fitted to fourth-order polynomial equation as

$$\frac{a}{W} = 1.165\times10^{-8}\theta^4 - 1.129\times10^{-6}\theta^3 + 6.310\times10^{-5}\theta^2 - 5.704\times10^{-4}\theta + 0.349 \qquad (6.5)$$

while the relationship between *a*/*W* and θ from the calibration curve of V_L/V_R can be represented as

$$\frac{a}{W} = 3.086\times10^{-7}\theta^4 - 4.093\times10^{-5}\theta^3 + 2.063\times10^{-3}\theta^2 - 4.857\times10^{-2}\theta + 0.674 \qquad (6.6)$$

Solving Eq.(6.5) and Eq.(6.6) to find the intersection in Fig.6.16, the obtained *a*/*W* = 0.3488 and θ = 10.45° which the percentage error of the obtained *a*/*W* and θ are 0.34 and 4.5 respectively.

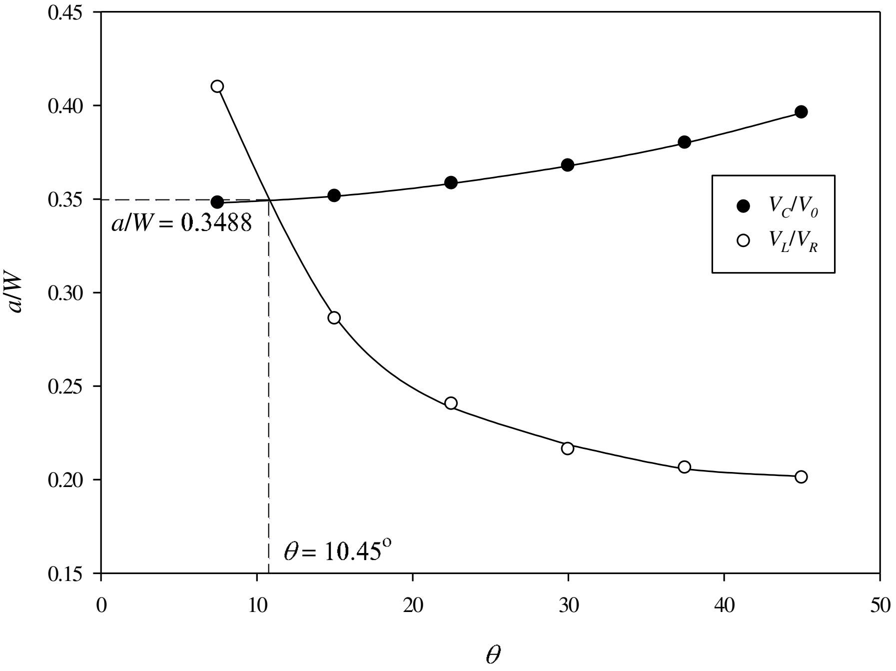

Fig.6.16 The relationship between *a*/*W* and θ from the calibration curve of V_C/V_0 and V_L/V_R for second case study

6.4 Conclusions

This chapter presents the application of the finite volume method for more complicate crack problems, i.e. the inclined edge crack. The simulation was done and calibration curve was constructed for a crack having its length to specimen width *a*/*W* equal to 0.1 to 0.8 at 0.1 intervals and inclination angle θ equal to 7.5° to 45° at 7.5° intervals.

Next, a proposed methodology for characterizing an inclined edge crack was described. The position of crack mouth is assumed to be known before measuring the potential. The method requires the potential difference at the position symmetrically to a crack mouth and two adjacent positions.

The last part shows the 2 case studies of inclined edge cracked specimen in order to verify the described method. There is slight error of the obtained result for the first case study at 0.11% of crack length to specimen width ratio *a*/*W* and 0.25% of cracked angle θ. The percentage error for second case study is 0.34% for crack length to specimen width ratio *a*/*W* and 4.50% for cracked angle θ.

Chapter 7

Conclusions and Suggestions

After presenting the electric potential drop method, the basic electrical theorem, the finite volume theorem, the studied basic cracked specimen and the case study of a more complex cracked specimen, i.e. inclined edge cracked specimen, this chapter summarizes the previous chapters and gives the suggestions for further work.

7.1 Conclusions

The objective of this thesis is to develop and utilize a finite volume method with C++ code to simulate the electric potential distribution within through-thickness cracked plates. Then, the calibration curve is generated to identify crack length and the angle of crack in cases of inclined cracks.

This work employs the cell-centered unstructured quadrilateral grid to discretize the problem domain into a partitioning set of control volumes. This grid type is flexible enough to fit the complex model and can be generated conveniently by a free mesh generator software, Automesh2D [32]. By applying the least square fit method [33] and truncating the Taylor series, the steady state electric potential equation in the partial differential form can be approximated into simultaneous algebraic equation. Moreover, due to the unstructured quadrilateral cell shape, the orthogonal correction approach [29] is also employed to improve the accuracy of the solution.

To verify the written C++ program, the distributions of electric potential within 2 basic cracked planes, i.e. single edge cracked plane and central cracked plane with crack length to specimen width ratio a/W from 0.1 to 0.8 at 0.1 intervals, are simulated. Then, with the grid independent solutions - the numerical calibration curves, the relationship between the potential difference across the crack and crack size - are established and compared with the analytical solutions. The maximum percentage error of the numerical results is 1.15% for the single edge crack case at $a/W = 0.4$ and 1.69% for central crack case at $a/W = 0.8$.

This thesis also simulates the distribution of potential within inclined edge cracked planes at crack length to specimen width ratio a/W from 0.1 to 0.8 at 0.1 intervals and the crack angles of 7.5° to 45° at 7.5° intervals and presents the method to calibrate the inclined edge crack shape in terms of crack length a and the angle of inclination θ. The adjacent potential differences V_L and V_R are added to calculate the another calibration curve in addition to the curve of potential different across the crack V_c. The adjacent potential differences ratio V_L/V_R at different crack length a and angle θ are monitored in order to build the calibration curve.

To examine a test body, the measured potential different across the crack V_c and the adjacent potential differences ratio V_L/V_R are used to find the coordinate of a/W and θ from the calibration curves of each case. Then, the relationship between

a/W and θ of both cases are plotted in the same graph. The intersection of two curves represents the appearance of inclined crack within the test specimen. To verify this method, two case studies are simulated, the inclined edge cracked specimens with crack length to specimen width ratio $a/W = 0.55$ and cracked angle $\theta = 40°$ and the specimens with crack length to specimen width ratio $a/W = 0.35$ and cracked angle $\theta = 10°$. The percentage error of the numerical result of a/W is 0.11% while that of θ is 0.25% for the first case while the percentage error of a/W is 0.34% and that of θ is 4.5% for the second.

The proposed inclined edge crack characterizing method can predict a crack size and inclination angle by measuring the potential difference at only three position pairs, i.e. the potential difference across the crack V_c, the adjacent potential differences V_L and V_R.

The method was accurate when compared with the previous method of Spitas *et al.* [14] which studied crack length to specimen width ratio a/W up to 0.4 in which the effect of orientations. However the proposed method considers the effect of crack orientation on the potential drop across the crack while the work of Spitas *et al.* did not. Nonetheless, the limitation of this method is that the position of crack mount must be known before measuring the potential.

7.2 Suggestions

The mesh generating process in this thesis simply utilizes a free license computer software, Automesh2D. The grid independency is ensured by increasing control volume (CV) number with some restrictions due to the limitation of the grid generator. The grid shapes and alignment are difficult to control. By developing C++ computer codes, the adaptive mesh refinement would provide more accurate results with less CV numbers and computational cost.

The numerical calibration curves for basic cracked planes are established with the range of crack length to specimen width ratio a/W from 0.1 to 0.8 and agree well with the analytical calibration curves. However, the extreme value of crack length to specimen width ratio a/W less than 0.1 and more than 0.8 are also interesting to calculate especially in terms of the sensitivity of the small crack size calibration.

Similarly, for inclined crack case, this work only calculates the calibration curve for crack degree angle 7.5° to 45°. The sensitivity of this method for small angle and the calibration curve for high degree angle especially for almost 90° should be studied. The negative crack angle is of concern values about the difference of calibration curve compared with the positive angle.

The distance from inclined edge crack for potential measurement used in this work is equal to 5 mm. This value should be optimized to find the best positions of potential probes which provide the best calibration curves in terms of accuracy, sensibility, reproducibility and measurability.

The electric current input in this numerical process is assumed to be constant along the specimen boundary. For real inspection tools, the electric current input should be considered as a point source. Thus, the numerical current input should be adjusted to be coping with real equipment.

The obtained calibration of inclined edge crack from the method presented in this thesis is conducted by numerical techniques only. In order to ensure the validity of numerical solutions, experiments should be done to compare the results.

The most interesting and challenge target is to improve the ability of this presented program to solve nonlinear problems because in real situations, the non-uniform temperature distributed within the component directly affects the changes of the electric conductivity within the specimen, the obtained results are probably more similar to the real operating component.

This work presents the alternative method for characterizing inclined crack which there are another methods as described in Chapter 2. This method still should be developed and studied in details in many aspects such as the grid generating process, the wider range of the characterizing crack length and inclination angle, the proper potential measurement position and the validation process etc., moreover, it should be improved to be coping with real equipment and operating component, especially, in terms of current input and the effect of the non-uniform temperature distribution.

REFERENCES

1. H. A. Richard, M. Sander, B. Schramm, G. Kullmer, and M. Wirxel, *Fatigue crack growth in real structures.* International Journal of Fatigue, 2013. **50**: p. 83-88.
2. T. L. Anderson, *Fracture Mechanics: Fundamentals and Applications, Third Edition*. 2005: Taylor & Francis.
3. R. P. Wei and R. L. Brazill, *An assessment of AC and DC potential systems for monitoring fatigue crack growth.* Fatigue crack growth measurement and data analysis, ASTM STP, 1981. **738**: p. 103-119.
4. ASM International. Handbook Committee, *Fatigue and Fracture*. 1996: ASM International.
5. N. Merah, *Detecting and measuring flaws using electric potential techniques.* Journal of Quality in Maintenance Engineering, 2003. **9**(2): p. 160-175.
6. K. -H. Schwalbe and D. Hellmann, *Application of the electrical potential method to crack length measurements using Johnson's formula.* Journal of Testing and Evaluation, 1981. **9**(3): p. 218-221.
7. R. O. Ritchie and K. J. Bathe, *On the calibration of the electrical potential technique for monitoring crack growth using finite element methods.* International Journal of Fracture, 1979. **15**(1): p. 47-55.
8. D. W. J. Pulle, *Crack length measurement: Analysis of the electropotential method using a finite element method.* The Journal of Strain Analysis for Engineering Design, 1986. **21**(3): p. 127-134.
9. W. K. Wilson, *On the electrical potential analysis of a cracked fracture mechanics test specimen using the finite element method.* Engineering Fracture Mechanics, 1983. **18**(2): p. 349-358.
10. G. H. Aronson and R. O. Ritchie, *Optimization of the electrical potential technique for crack growth monitoring in compact test pieces using finite element analysis.* Journal of Testing and Evaluation, 1979. **7**(4): p. 208-215.
11. L. Gandossi, S. A. Summers, N. G. Taylor, R. C. Hurst, B. J. Hulm, and J. D. Parker, *The potential drop method for monitoring crack growth in real components subjected to combined fatigue and creep conditions: application of FE techniques for deriving calibration curves.* International Journal of Pressure Vessels and Piping, 2001. **78**(11–12): p. 881-891.
12. L. Doremus, Y. Nadot, G. Henaff, C. Mary, and S. Pierret, *Calibration of the potential drop method for monitoring small crack growth from surface anomalies – Crack front marking technique and finite element simulations.* International Journal of Fatigue, 2015. **70**(0): p. 178-185.
13. Tanawut Kornchamruskul, *A study on electrical potential distribution in rectangular plate with an inclined crack by finite element method*. Master's thesis. 2005, Chulalongkorn University.
14. V. Spitas, C. Spitas, and P. Michelis, *A three-point electrical potential difference method for in situ monitoring of propagating mixed-mode cracks at high temperature*. Measurement, 2010. **43**(7): p. 950-959.
15. L. Saint-Sulpice, M. Lakrit, S. Arbab Chirani, and S. Calloch, *Variation in electric resistivity in metastable alloys during thermomechanical loading:*

Effects of temperature, elasticity, plasticity and phase transformation. Mechanics of Materials, 2014. **71**: p. 1-9.

16. S. Patankar, *Numerical Heat Transfer and Fluid Flow*. 1980: Taylor & Francis.
17. S. J. Findlay and N. D. Harrison, *Why aircraft fail.* Materials Today, 2002. **5**(11): p. 18-25.
18. J. L. Otegui, *Fatigue damage leads to a serious traffic accident.* Engineering Failure Analysis, 2002. **9**(1): p. 109-122.
19. R.J.H. Wanhill, N. Symonds, A. Merati, T. Pasang, and S.P. Lynch, *Five helicopter accidents with evidence of material and/or design deficiencies.* Engineering Failure Analysis, 2013. **35**: p. 133-146.
20. ASTM International, *ASTM E647-08 Standard Test Method for Measurement of Fatigue Crack Growth Rates*. 2008.
21. N. Fleck, *Compliance methods for measurement of crack length*. Fatigue Crack Measurement: Techniques and Applications. 1991, UK: Engineering Materials Advisory Services Ltd. 69-93.
22. R. H. VanStone and T. L. Richardson, *Potential-drop monitoring of cracks in surface-flawed specimens.* Automated Test Methods for Fracture and Fatigue Crack Growth, 1985: p. 148-166.
23. Hiroyuki Abé and Yutaka Kanoh, *An Inverse Problem in Nondestructive Inspection of a Crack in a Plate with an Inhomogeneity by Means of the Electrical Potential Method*, in *Micromechanics and Inhomogeneity: The Toshio Mura 65th Anniversary Volume*, G. J. Weng, M. Taya, and H. Abé, Editors. 1990, Springer New York: New York, NY. p. 1-15.
24. Wen-Hwa Chen, Jen-Shiung Chen, and Huei-Lu Fang, *A theoretical procedure for detection of simulated cracks in a pipe by the direct current–potential drop technique.* Nuclear Engineering and Design, 2002. **216**(1–3): p. 203-211.
25. T. Lertsurayut and K. Maneeratana. *The utilisation of delaunay triangulation in finite volume modelling*. in *ME-NETT 16*. 2002.
26. W. Wattananukulchai and K. Maneeratana. *Local Grid Refinement by Residual Error Estimation for Heat Conduction Simulation with Finite Volume Method*. in *ME-NETT 18*. 2004.
27. R. Prapainop and K. Maneeratana, *Simulation of ice formation by the finite volume method.* Songklanakarin Journal of Science and Technology, 2004. **26**(1): p. 56.
28. Wang Li, Bo Yu, Xinran Wang, Peng Wang, and Shuyu Sun, *A finite volume method for cylindrical heat conduction problems based on local analytical solution.* International Journal of Heat and Mass Transfer, 2012. **55**(21): p. 5570-5582.
29. H. Jasak, *Error analysis and estimation for the finite volume method with applications to fluid flows*, in *Department of Mechanical Engineering*. 1996, Imperial College, University of London.
30. H.D. Young, R.A. Freedman, and A.L. Ford, *University Physics with Modern Physics*. 2012: Pearson Education.
31. Y.H. Lee, *Introduction to Engineering Electromagnetics*. 2013: Springer.

32. X. W. Ma, G. Q. Zhao, and L. Sun, *AUTOMESH-2D/3D: robust automatic mesh generator for metal forming simulation.* Materials Research Innovations, 2011. **15**(s1): p. s482-s486.
33. S. Muzaferija, *Adaptive finite volume method for flow prediction using unstructured meshes and multigrid approach*, in *Department of Mechanical Engineering*. 1994, Imperial College, University of London.
34. ASM International. Handbook Committee, *Properties and Selection: Irons, Steels, and High-performance Alloys*. 1990: ASM International.

APPENDIX

Appendix A

Grid Independent Test

This appendix shows the process of grid independent test to find the grid independent solutions in order to generate the calibration curves of single edge and central cracked specimens in Chapter 5.

Firstly, the coarse meshes are used to solve a problem. Then, finer meshes would be generated to determine the solution of the same problem. If there is no significant differences between the solutions from the coarse meshes and the finer meshes, it can be supposed that the coarse meshes can provide the grid independent solution.

For this potential distribution problem, the grid modeling is conducted in various numbers of grids containing approximately 1000 to 12000 cells. The solutions of electric potential at measured positions of each grid model are compared with the solution of the finest grid model. The percentage difference is calculated by

$$\text{Percentage difference} = \frac{|V_1 - V_2|}{(V_1 + V_2)/2} \times 100\% \tag{A.1}$$

where V_1 is the potential solution from the first grid model and V_2 is from the second which is the finest grid model. In this work, the grid independence is achieved if the percentage difference of the solutions from the coarse meshes compared with those of the finest meshes is less than 0.5%.

This appendix shows the various grid models for grid independent testing for each cracked specimen and crack size in Chapter 5. The obtained grid independent solutions of the normalized potential drop across the crack are also compared with the Johnson's solution.

A.1 Single Edge Cracked Specimen

In this case, the grid independence is checked from the potential results along $Y = 0$ mm. Because the potential results at the right side of crack ($X > 50$ mm) do not significantly change following the addition of control volume (CV) number; thus, this appendix shows the grid independency checking only in the left side of crack within the range of 25 mm $< X <$ 50 mm.

For the single edge cracked specimen's domain with $a/W = 0.1$, the mesh number used is 1044, 2054, 4046, 8201 and 12055 as shown in Fig. A.1. The potential results along $Y = 0$ mm of each grid model are also displayed in Fig. A.2. By comparing these values of each grid model, the grid model of 4046 CVs can provide the grid independent solution.

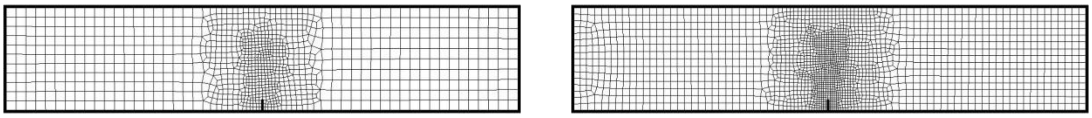

(a) 1044 CVs (b) 2054 CVs

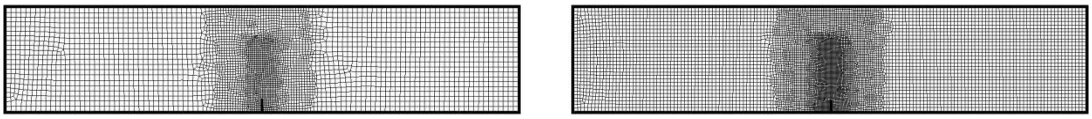

(c) 4046 CVs (d) 8201 CVs

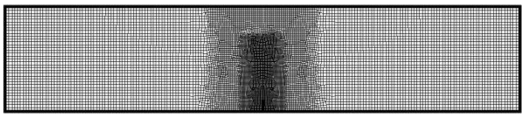

(e) 12055 CVs

Fig. A.1 Different number of control volume generating used of single edge cracked specimen with crack length to specimen width ratio $a/W = 0.1$

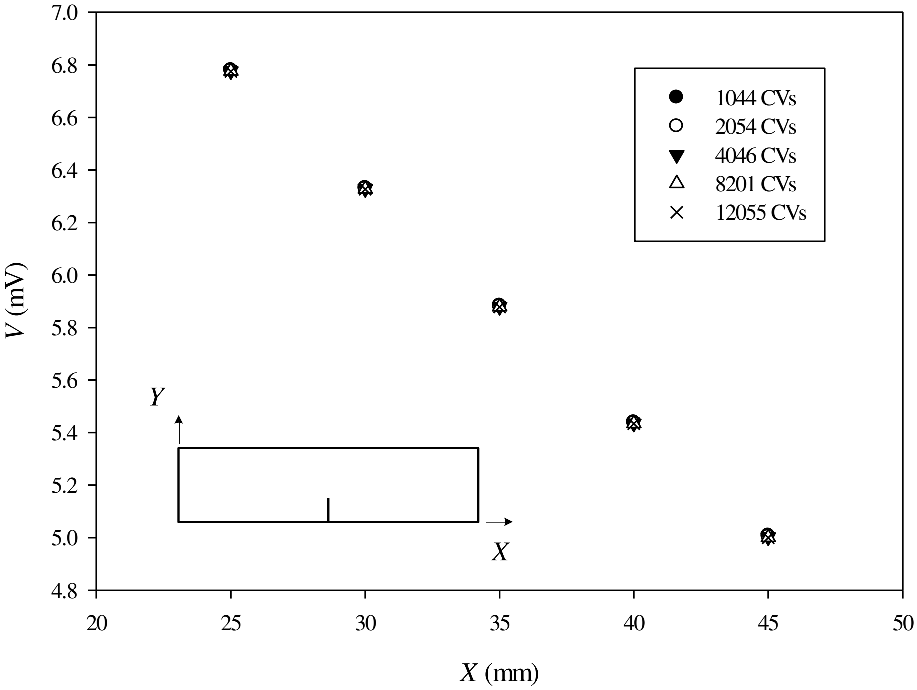

Fig. A.2 Potential results along $Y = 0$ mm in single edge cracked plane with $a/W = 0.1$

For $a/W = 0.2$, the CV number used is consisted of 1041, 2082, 4062, 8061 and 12146 as shown in Fig. A.3. The potential results along $Y = 0$ mm are also shown in Fig. A.4. By comparing these values of each grid model, the grid model of 4062 CVs can provide the grid independent solution.

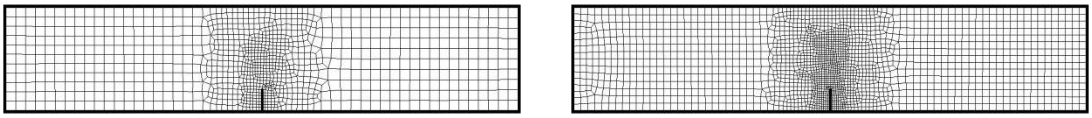

(a) 1041 CVs (b) 2082 CVs

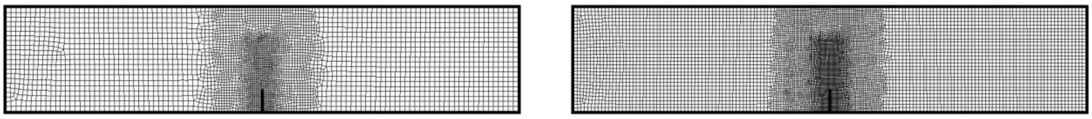

(c) 4062 CVs (d) 8061 CVs

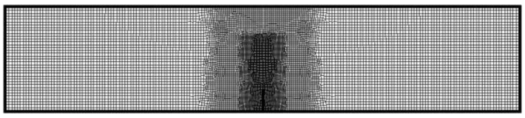

(e) 12146 CVs

Fig. A.3 Different number of control volume generating used of single edge cracked specimen with crack length to specimen width ratio $a/W = 0.2$

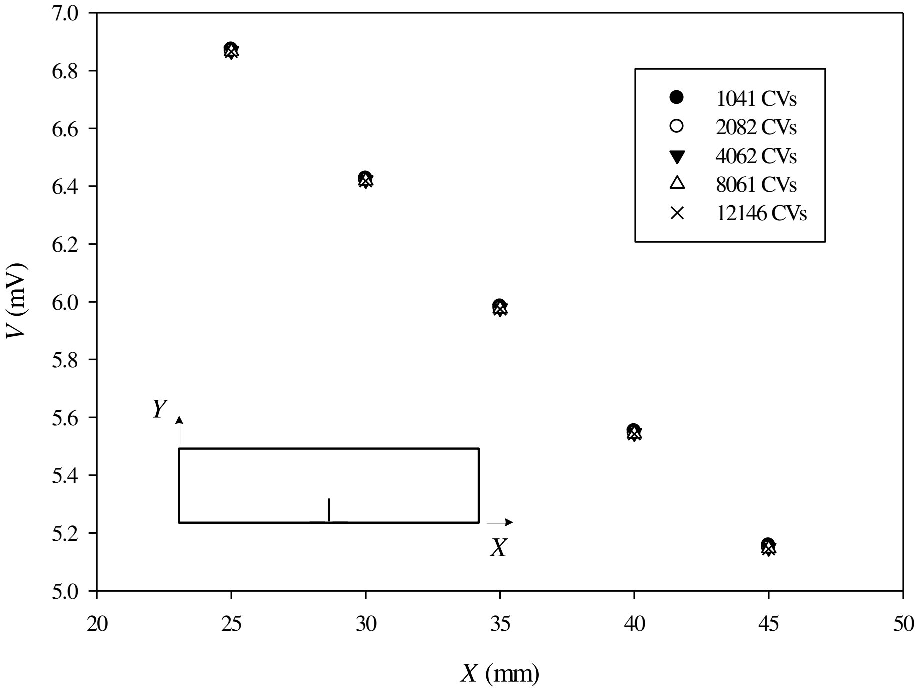

Fig. A.4 Potential results along $Y = 0$ mm in single edge cracked plane with $a/W = 0.2$

For $a/W = 0.3$, the cell number used is consisted of 1051, 2059, 4088, 8091 and 12106 as shown in Fig. A.5. The potential results along $Y = 0$ mm are also shown in Fig. A.6. By comparing these values of each grid model, the grid model of 8091 CVs can provide the grid independent solution.

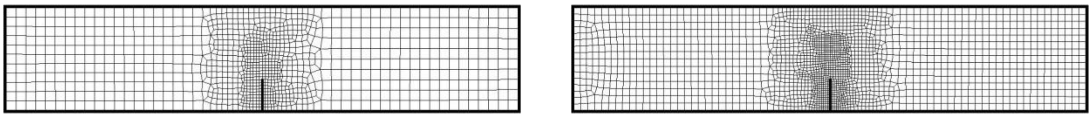

(a) 1051 CVs (b) 2059 CVs

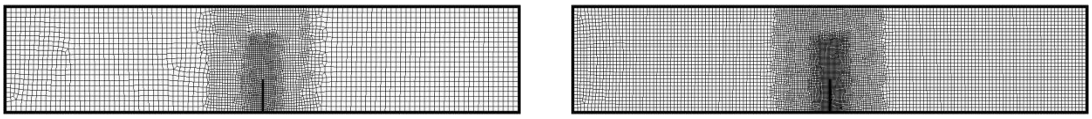

(c) 4088 CVs (d) 8091 CVs

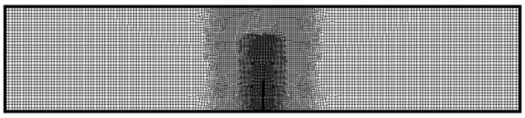

(e) 12106 grids

Fig. A.5 Different number of control volume generating used of single edge cracked specimen with crack length to specimen width ratio $a/W = 0.3$

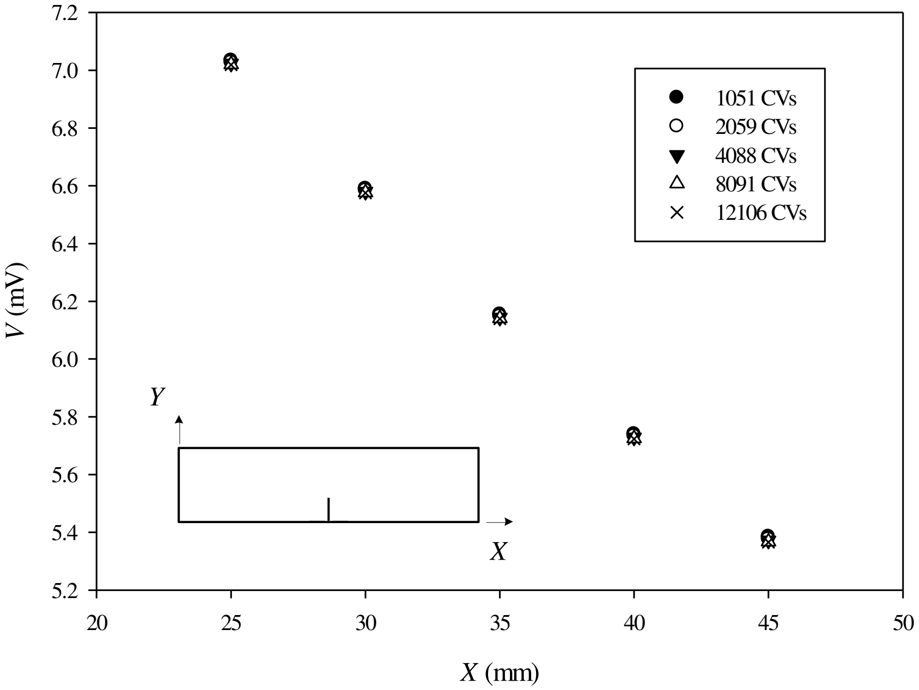

Fig. A.6 Potential results along $Y = 0$ mm in single edge cracked plane with $a/W = 0.3$

For $a/W = 0.4$, the CV number used is consisted of 1050, 2066, 4075, 8085 and 11970 as shown in Fig. A.7. The potential results along $Y = 0$ mm are also shown in Fig. A.8. By comparing these values of each grid model, the grid model of 4075 CVs can provide the grid independent solution.

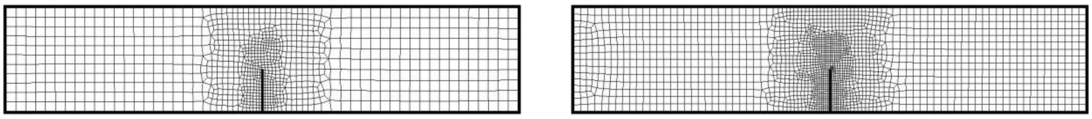

(a) 1061 CVs (b) 2067 CVs

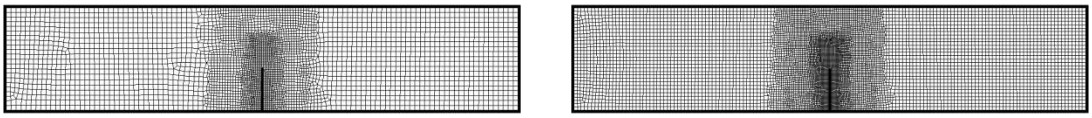

(c) 4054 CVs (d) 8113 CVs

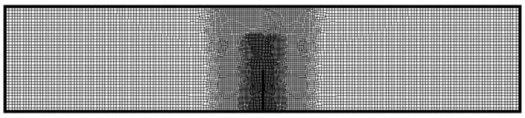

(e) 11942 CVs

Fig. A.7 Different number of control volume generating used of single edge cracked specimen with crack length to specimen width ratio $a/W = 0.4$

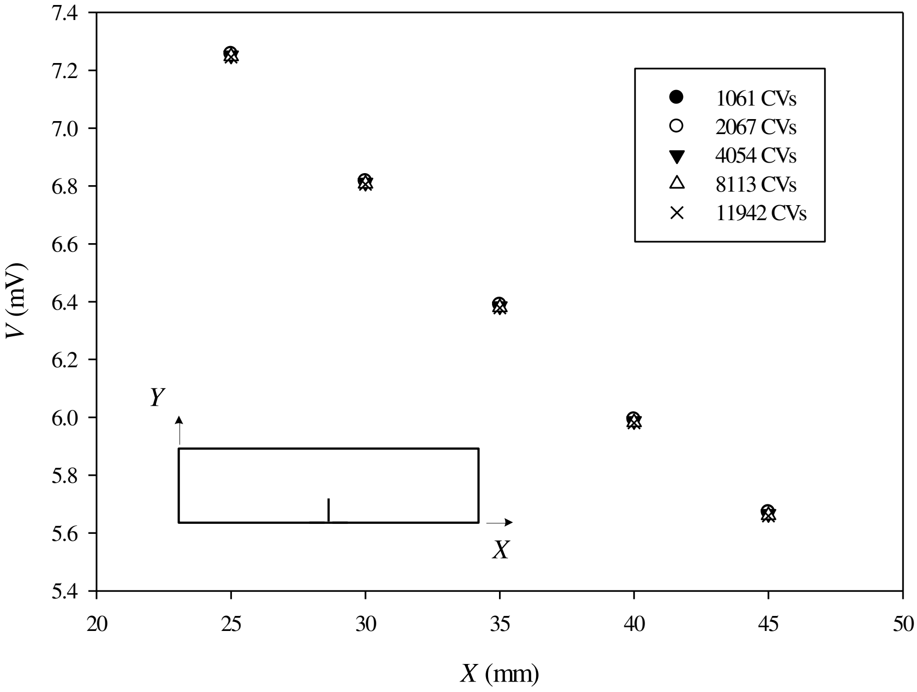

Fig. A.8 Potential results along $Y = 0$ mm in single edge cracked plane with $a/W = 0.4$

For $a/W = 0.5$, the CV number used is consisteded of 1050, 2066, 4075, 8085 and 11970 as shown in Fig. A.9. The potential results along $Y = 0$ mm are also shown in Fig. A.10. By comparing these values of each grid model, the grid model of 4075 CVs can provide the grid independent solution.

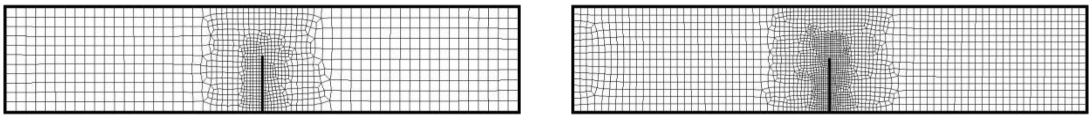

(a) 1050 CVs (b) 2066 CVs

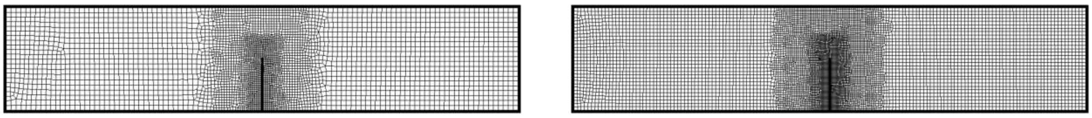

(c) 4075 CVs (d) 8085 CVs

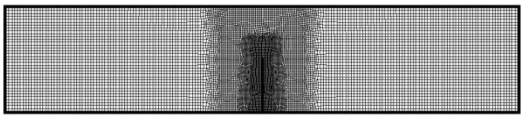

(e) 11970 CVs

Fig. A.9 Different number of control volume generating used of single edge cracked specimen with crack length to specimen width ratio *a*/*W* = 0.5

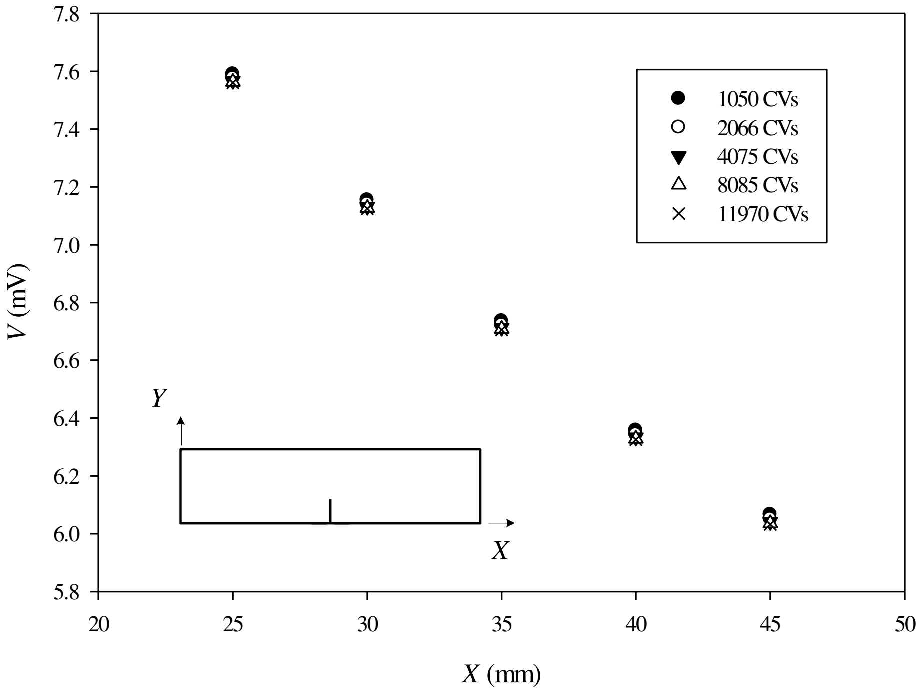

Fig. A.10 Potential results along $Y = 0$ mm in single edge cracked plane with *a*/*W* = 0.5

For *a*/*W* = 0.6, the CV number used is consisteded of 1057, 2080, 4055, 8113 and 12059 as shown in Fig. A.11. The potential results along Y = 0 mm are also shown in Fig. A.12. By comparing these values of each grid model, the grid model of 4055 CVs can provide the grid independent solution.

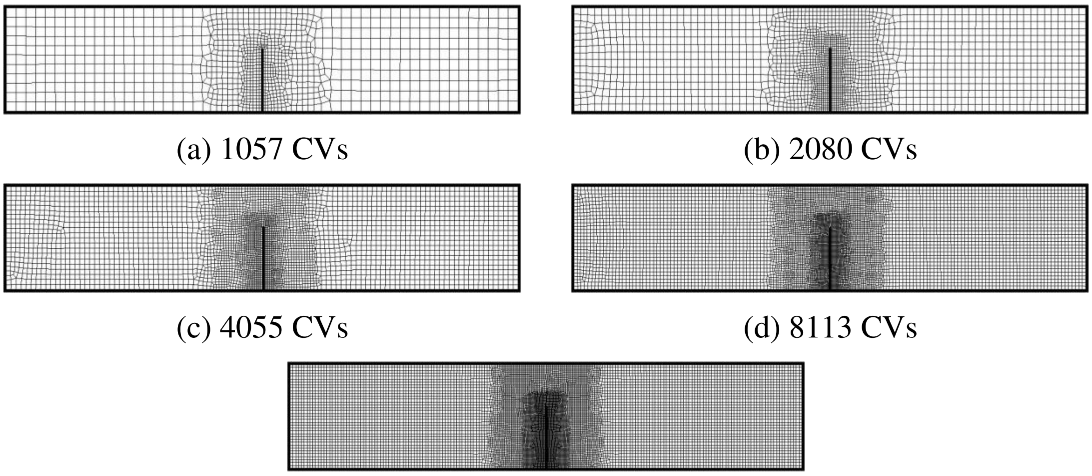

(a) 1057 CVs
(b) 2080 CVs
(c) 4055 CVs
(d) 8113 CVs
(e) 12059 CVs

Fig. A.11 Different number of control volume generating used of single edge cracked specimen with crack length to specimen width ratio $a/W = 0.6$

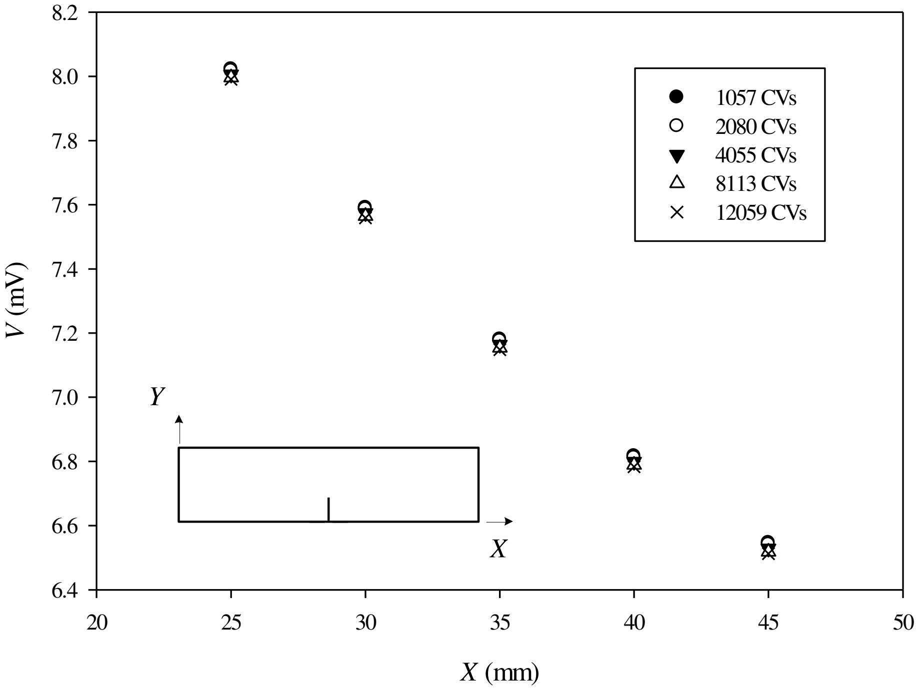

Fig. A.12 Potential results along $Y = 0$ mm in single edge cracked plane with $a/W = 0.6$

For $a/W = 0.7$, the CV number used is consisteded of 1042, 2112, 4085, 8145 and 12037 as shown in Fig. A.13. The potential results along $Y = 0$ mm are also shown in Fig. A.14. By comparing these values of each grid model, the grid model of 8145 CVs can provide the grid independent solution.

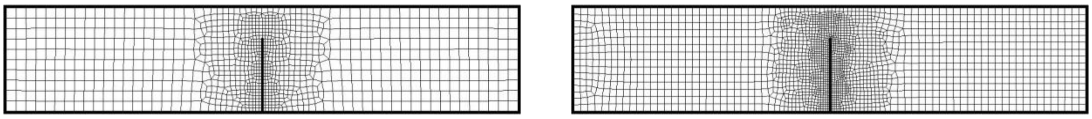

(a) 1042 CVs (b) 2112 CVs

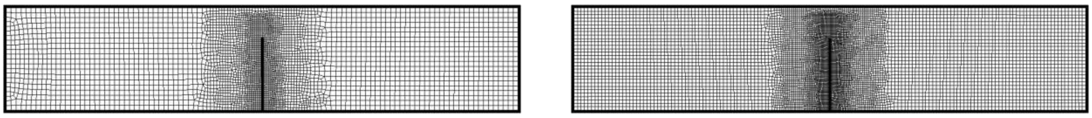

(c) 4085 CVs (d) 8145 CVs

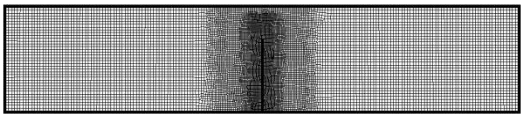

(e) 12037 CVs

Fig. A.13 Different number of control volume generating used of single edge cracked specimen with crack length to specimen width ratio $a/W = 0.7$

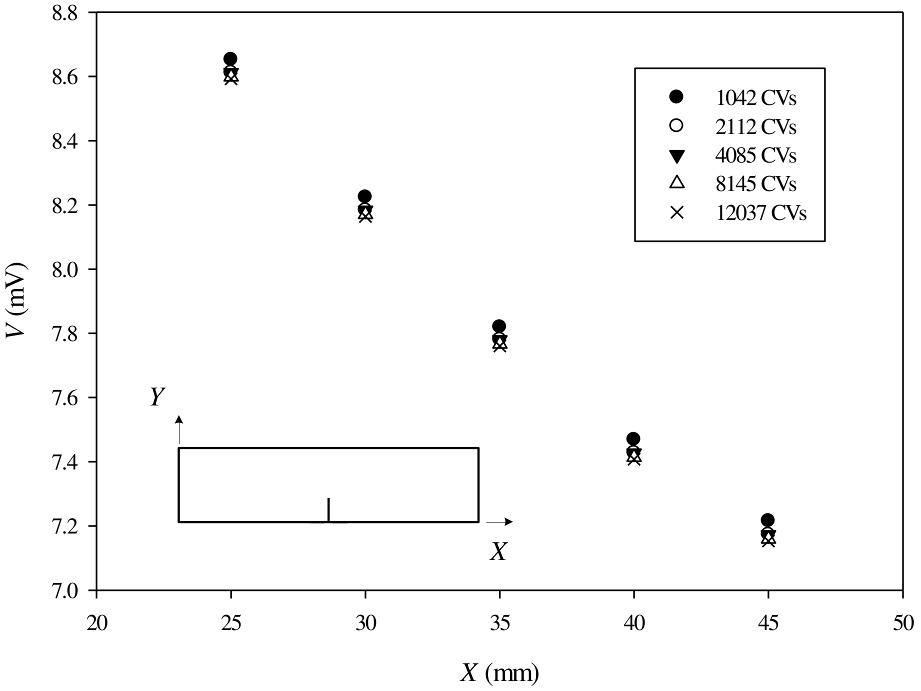

Fig. A.14 Potential results along $Y = 0$ mm in single edge cracked plane with $a/W = 0.7$

For $a/W = 0.8$, the CV number used is consisted of 1061, 2064, 4072, 7874 and 12106 as shown in Fig. A.15. The potential results along $Y = 0$ mm are also shown in Fig. A.16. By comparing these values of each grid model, the grid model of 7874 CVs can provide the grid independent solution.

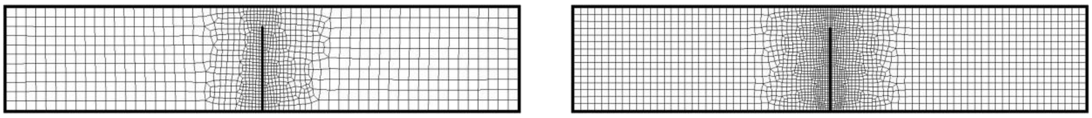

(a) 1061 CVs (b) 2064 CVs

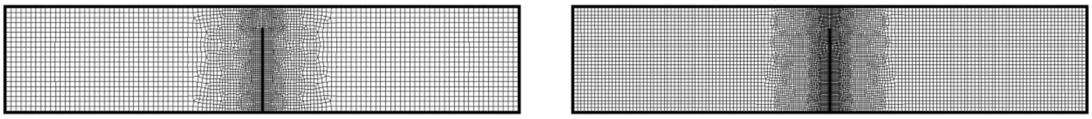

(c) 4072 CVs (d) 7874 CVs

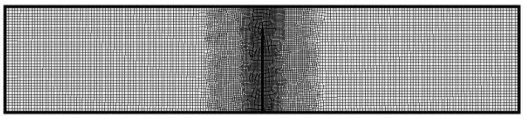

(e) 12106 grids

Fig. A.15 Different number of control volume generating used of single edge cracked specimen with crack length to specimen width ratio $a/W = 0.8$

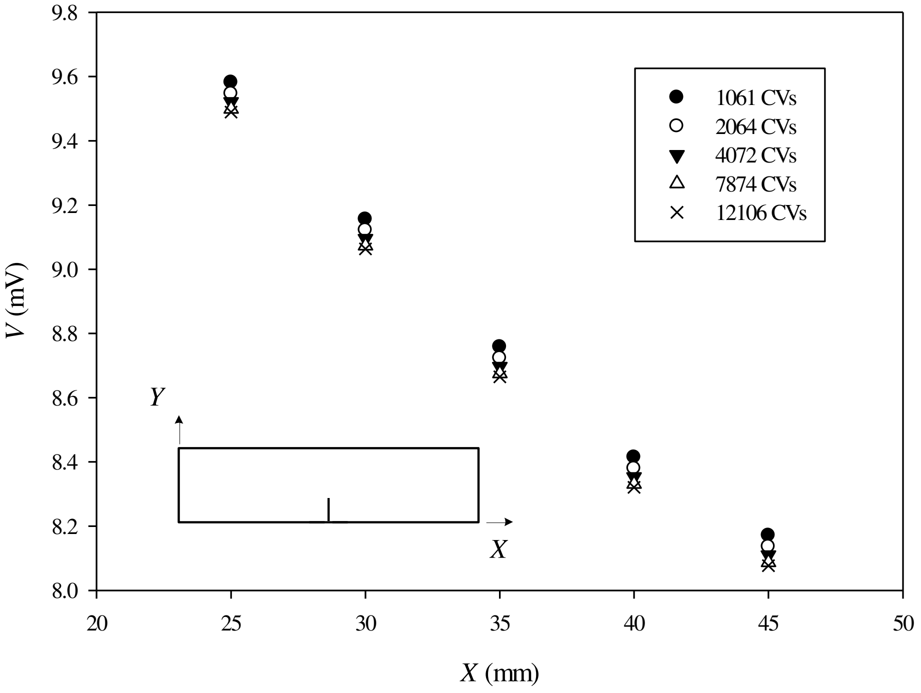

Fig. A.16 Potential results along $Y = 0$ mm in single edge cracked plane with $a/W = 0.8$

The number of CV used for single edged cracked specimen with different crack length to specimen width ratio a/W is concluded in Table A.1 to Table A.5. These tables also compare the numerical normalized potential different across the crack V/V_0 at various measured distance from $y = 5$ to 25 mm with Johnson's solution in Eq.(5.1).

Table A.1 The normalized potential drop (V/V_0) across the single edged crack compared with analytical solution at potential probe y = 5 mm

a/W	No. of CV	V/V_0		Percentage Error
		Johnson Eq.	FVM	
0.1	4046	1.090	1.081	0.815
0.2	4062	1.316	1.302	1.103
0.3	8091	1.636	1.623	0.822
0.4	4054	2.046	2.023	1.142
0.5	4075	2.533	2.506	1.055
0.6	4055	3.129	3.095	1.101
0.7	8145	3.881	3.846	0.908
0.8	7874	4.945	4.893	1.060

Table A.2 The normalized potential drop (V/V_0) across the single edged crack compared with analytical solution at potential probe y = 10 mm

a/W	No. of CV	V/V_0		Percentage Error
		Johnson Eq.	FVM	
0.1	4046	1.026	1.024	0.257
0.2	4062	1.099	1.094	0.453
0.3	8091	1.215	1.210	0.423
0.4	4054	1.380	1.370	0.723
0.5	4075	1.591	1.579	0.757
0.6	4055	1.866	1.849	0.888
0.7	8145	2.224	2.207	0.761
0.8	7874	2.744	2.718	0.944

Table A.3 The normalized potential drop (V/V_0) across the single edged crack compared with analytical solution at potential probe y = 15 mm

a/W	No. of CV	V/V_0		Percentage Error
		Johnson Eq.	FVM	
0.1	4046	1.014	1.013	0.136
0.2	4062	1.054	1.051	0.254
0.3	8091	1.119	1.116	0.260
0.4	4054	1.215	1.209	0.477
0.5	4075	1.343	1.335	0.541
0.6	4055	1.514	1.504	0.691
0.7	8145	1.744	1.733	0.624
0.8	7874	2.084	2.067	0.816

Table A.4 The normalized potential drop (V/V_0) across the single edged crack compared with analytical solution at potential probe y = 20 mm

a/W	No. of CV	V/V_0		Percentage Error
		Johnson Eq.	FVM	
0.1	4046	1.010	1.009	0.092
0.2	4062	1.037	1.035	0.177
0.3	8091	1.081	1.079	0.186
0.4	4054	1.149	1.145	0.359
0.5	4075	1.240	1.235	0.425
0.6	4055	1.364	1.356	0.574
0.7	8145	1.532	1.524	0.525
0.8	7874	1.785	1.772	0.710

Table A.5 The normalized potential drop (V/V_0) across the single edged crack compared with analytical solution at potential probe $y = 25$ mm

a/W	No. of CV	V/V_0		Percentage Error
		Johnson Eq.	FVM	
0.1	4046	1.007	1.007	0.069
0.2	4062	1.028	1.027	0.136
0.3	8091	1.062	1.061	0.146
0.4	4054	1.115	1.111	0.287
0.5	4075	1.186	1.182	0.347
0.6	4055	1.283	1.277	0.489
0.7	8145	1.416	1.410	0.449
0.8	7874	1.617	1.607	0.624

A.2 Central Cracked Specimen

Due to the symmetrical potential distribution, the numerical simulation is conducted only the upper half of the domain including to grid generating process. The grid independence is checked from the potential results along $Y = W$ in the left side of crack within the range of potential measured location, 20 mm < X < 36 mm, where there is the obvious difference between potential result of coarse and fine grid model.

For the central cracked specimen's domain with $a/W = 0.1$, the CV number is 1038, 2009, 4024, 8031 and 11864 as shown in Fig. A.17. The potential results along $Y = W$ of each grid model are also displayed in Fig. A.18. By comparing these values of each grid model, the grid model of 4024 CVs can provide the grid independent solution.

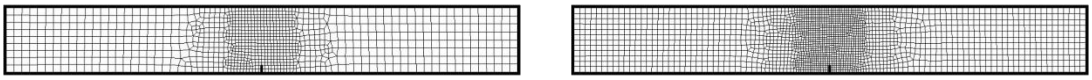

(a) 1038 CVs (b) 2009 CVs

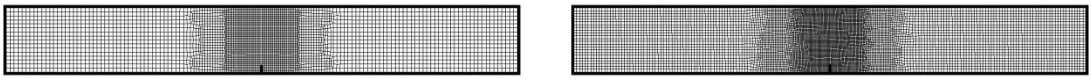

(c) 4024 CVs (d) 8031 CVs

(e) 11864 CVs

Fig. A.17 Different number of control volume generating used of central cracked specimen with crack length to specimen width ratio $a/W = 0.1$

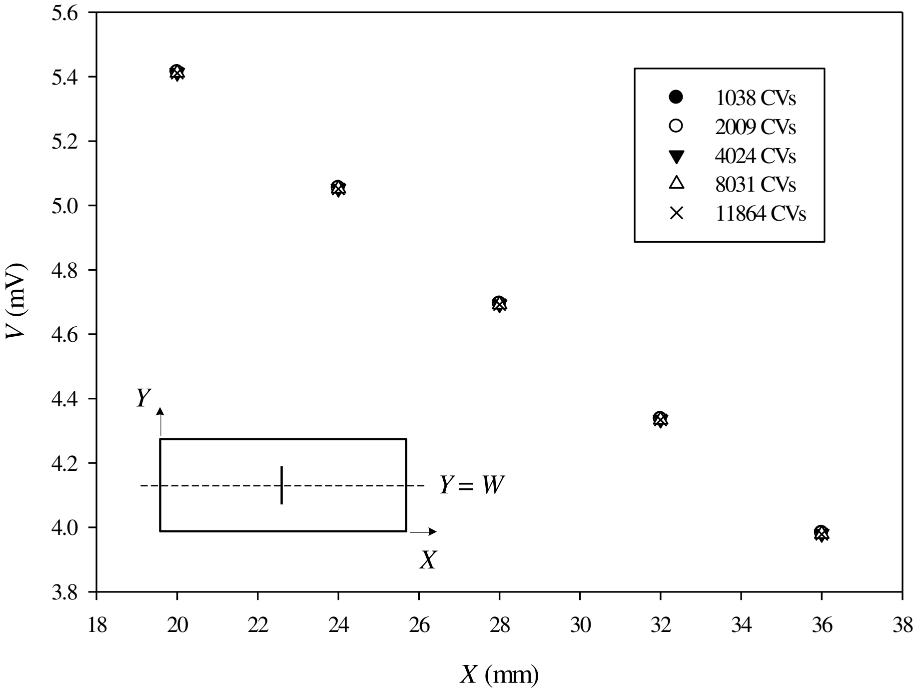

Fig. A.18 Potential results along $Y = W$ in central cracked plane with $a/W = 0.1$

For $a/W = 0.2$, the CV number used is consisted of 1034, 2009, 4024, 8019 and 11980 as shown in Fig. A.19. The potential results along $Y = W$ are also shown in Fig. A.20. By comparing these values of each grid model, the grid model of 4024 CVs can provide the grid independent solution.

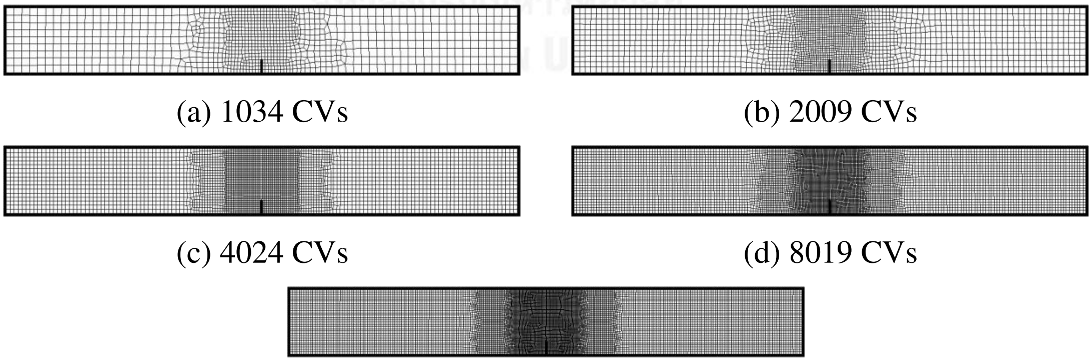

(a) 1034 CVs

(b) 2009 CVs

(c) 4024 CVs

(d) 8019 CVs

(e) 11980 CVs

Fig. A.19 Different number of control volume generating used of central cracked specimen with crack length to specimen width ratio $a/W = 0.2$

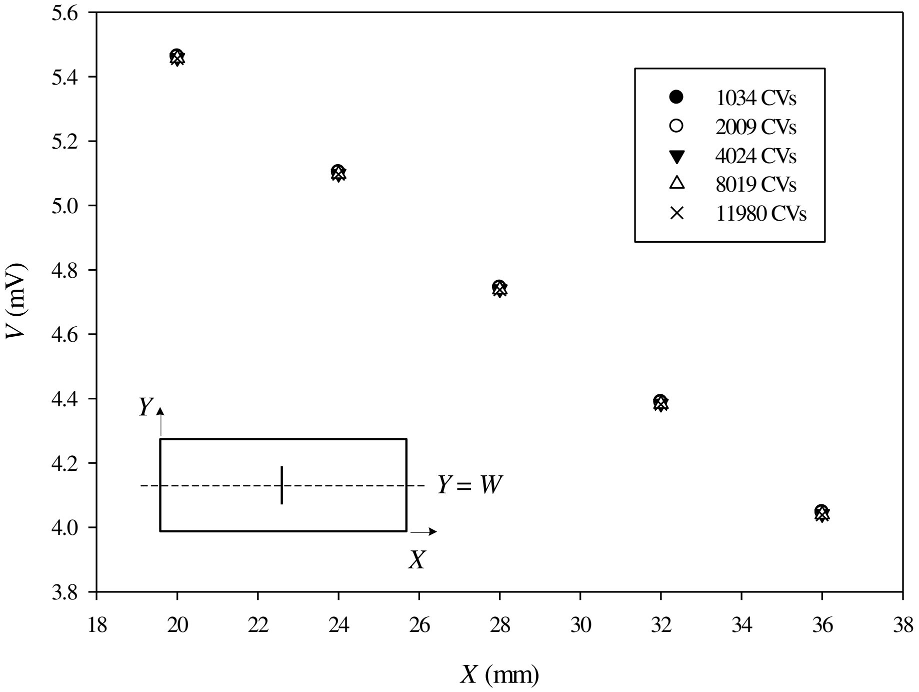

Fig. A.20 Potential results along $Y = W$ in central cracked plane with $a/W = 0.2$

For $a/W = 0.3$, the CV number used is consisted of 1033, 2004, 4024, 8018 and 11953 as shown in Fig. A.21. The potential results along $Y = W$ are also shown in Fig. A.22. By comparing these values of each grid model, the grid model of 8018 CVs can provide the grid independent solution.

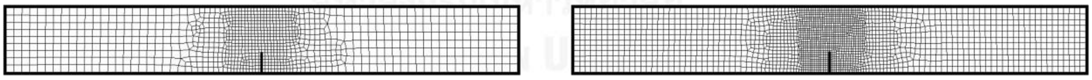

(a) 1033 CVs (b) 2004 CVs

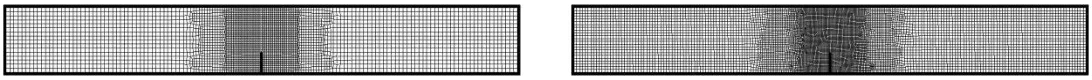

(c) 4024 CVs (d) 8018 CVs

(e) 11953 CVs

Fig. A.21 Different number of control volume generating used of central cracked specimen with crack length to specimen width ratio $a/W = 0.3$

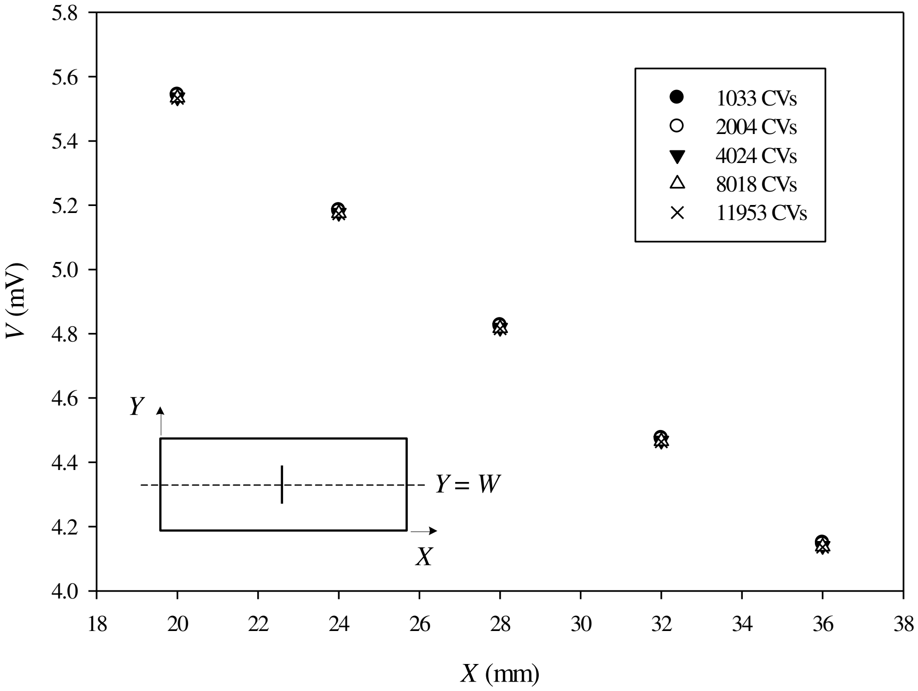

Fig. A.22 Potential results along $Y = W$ in central cracked plane with $a/W = 0.3$

For $a/W = 0.4$, the CV number used is consisted of 1034, 2014, 4024, 7990 and 11953 as shown in Fig. A.23. The potential results along $Y = W$ are also shown in Fig. A.24. By comparing these values of each grid model, the grid model of 7990 CVs can provide the grid independent solution.

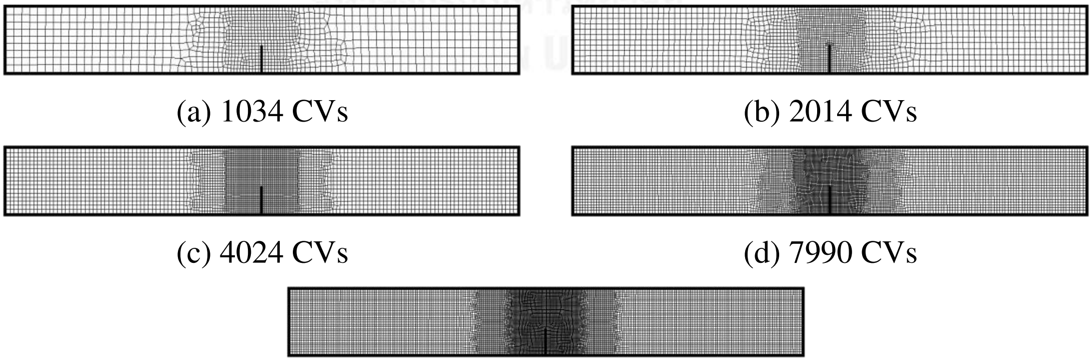
(a) 1034 CVs

(b) 2014 CVs

(c) 4024 CVs

(d) 7990 CVs

(e) 11953 CVs

Fig. A.23 Different number of control volume generating used of central cracked specimen with crack length to specimen width ratio $a/W = 0.4$

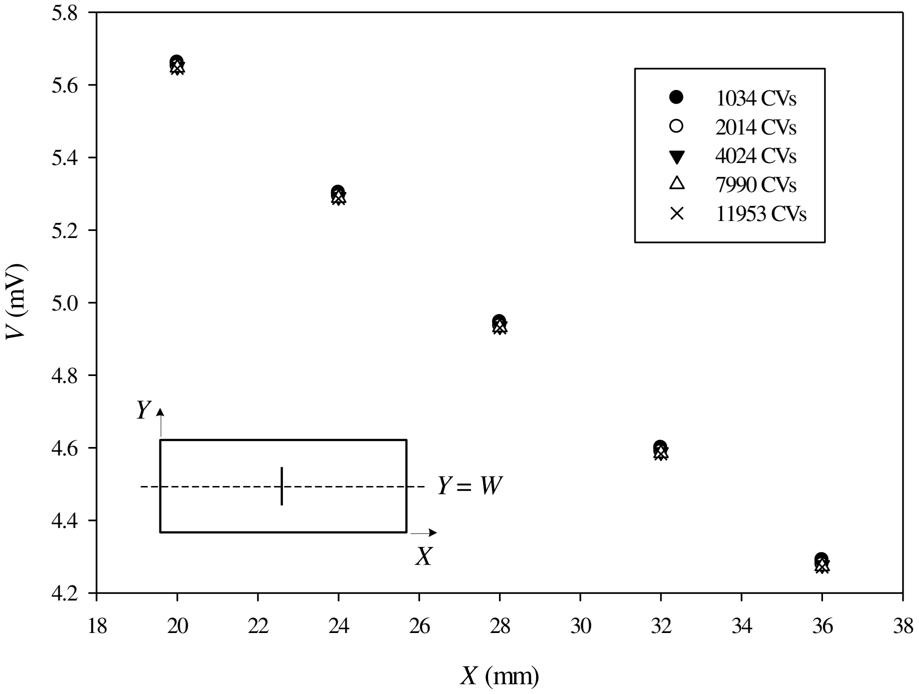

Fig. A.24 Potential results along $Y = W$ in central cracked plane with $a/W = 0.4$

For $a/W = 0.5$, the CV number used is consisted of 1038, 2019, 4024, 8031 and 11897 as shown in Fig. A.25. The potential results along $Y = W$ are also shown in Fig. A.26. By comparing these values of each grid model, the grid model of 8031 CVs can provide the grid independent solution.

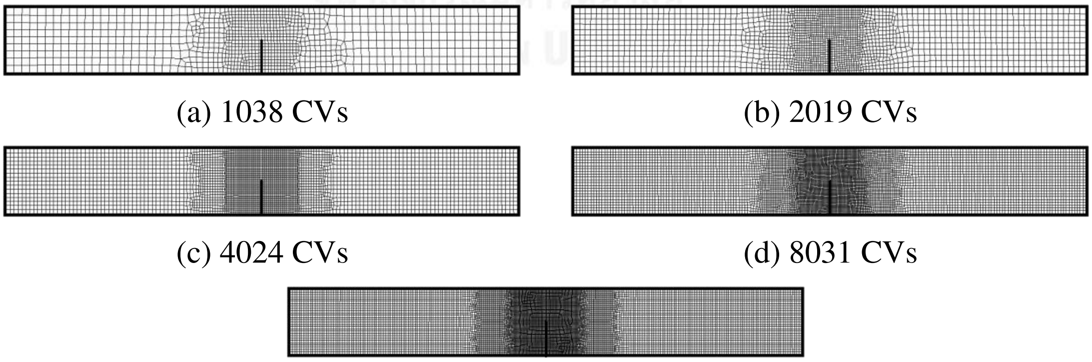
(a) 1038 CVs
(b) 2019 CVs
(c) 4024 CVs
(d) 8031 CVs
(e) 11897 CVs

Fig. A.25 Different number of control volume generating used of central cracked specimen with crack length to specimen width ratio $a/W = 0.5$

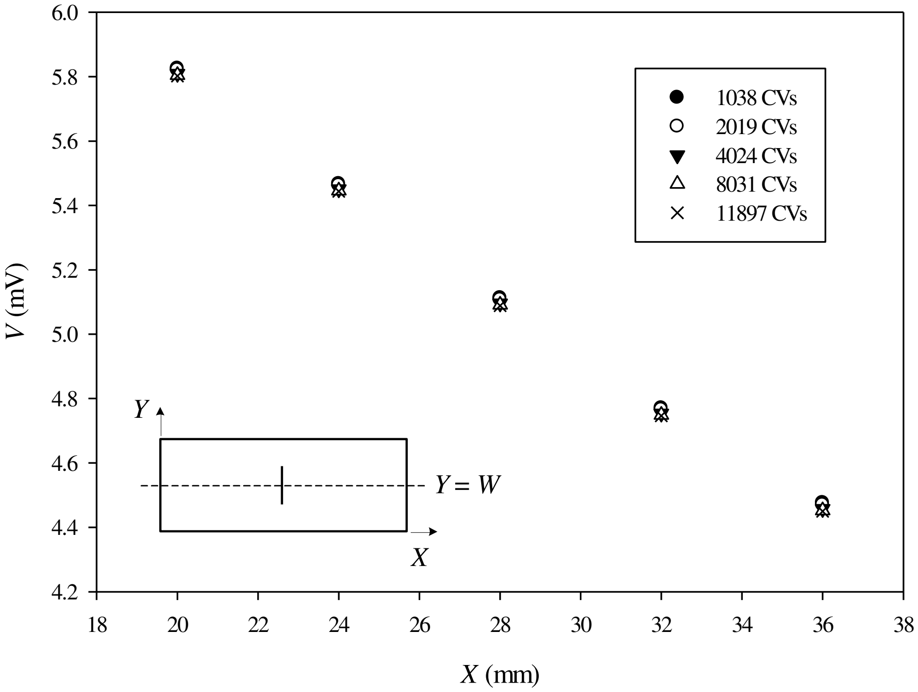

Fig. A.26 Potential results along $Y = W$ in central cracked plane with $a/W = 0.5$

For $a/W = 0.6$, the CV number used is consisted of 1029, 2027, 4024, 8036 and 11897 as shown in Fig. A.27. The potential results along $Y = W$ are also shown in Fig. A.28. By comparing these values of each grid model, the grid model of 8036 CVs can provide the grid independent solution.

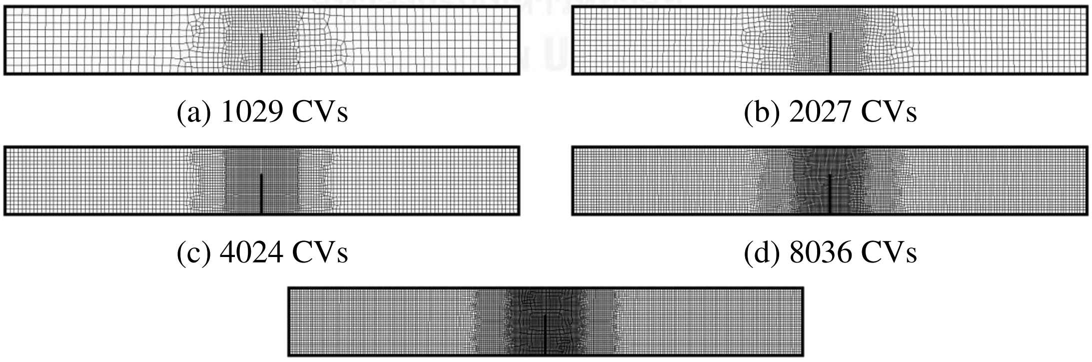

(a) 1029 CVs

(b) 2027 CVs

(c) 4024 CVs

(d) 8036 CVs

(e) 11897 CVs

Fig. A.27 Different number of control volume generating used of central cracked specimen with crack length to specimen width ratio $a/W = 0.6$

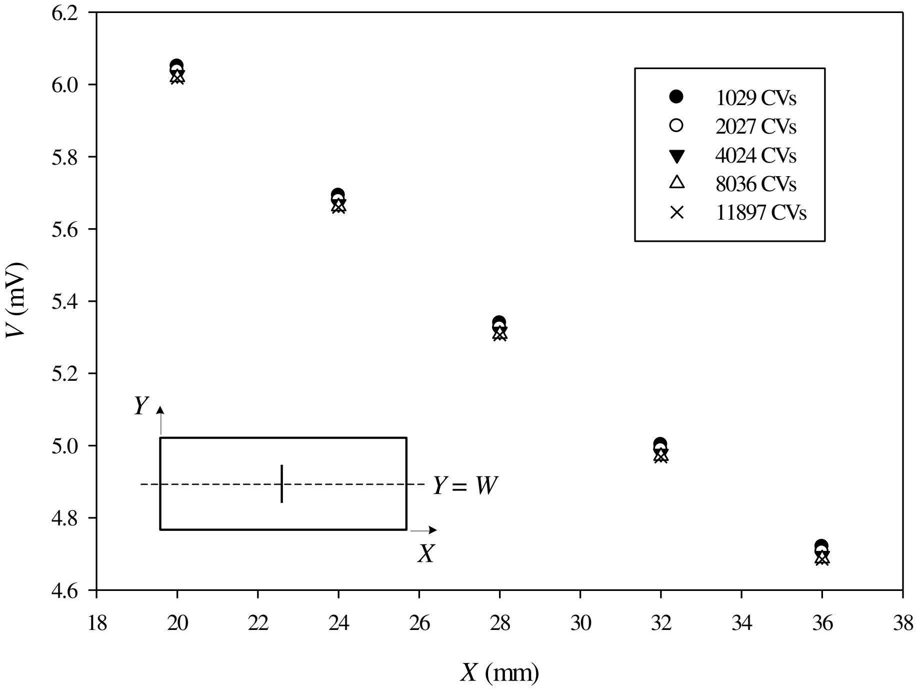

Fig. A.28 Potential results along $Y = W$ in central cracked plane with $a/W = 0.6$

For $a/W = 0.7$, the CV number used is consisted of 1041, 2027, 3984, 7985 and 11962 as shown in Fig. A.29. The potential results along $Y = W$ are also shown in Fig. A.30. By comparing these values of each grid model, the grid model of 7985 CVs can provide the grid independent solution.

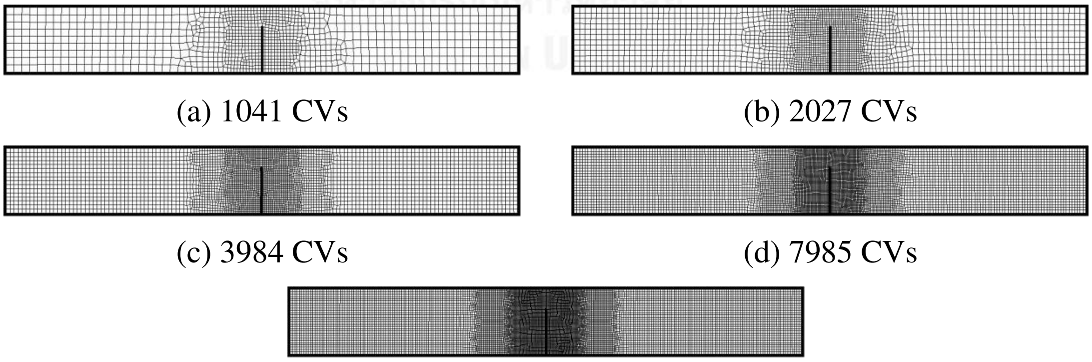

(a) 1041 CVs

(b) 2027 CVs

(c) 3984 CVs

(d) 7985 CVs

(e) 11962 CVs

Fig. A.29 Different number of control volume generating used of central cracked specimen with crack length to specimen width ratio $a/W = 0.7$

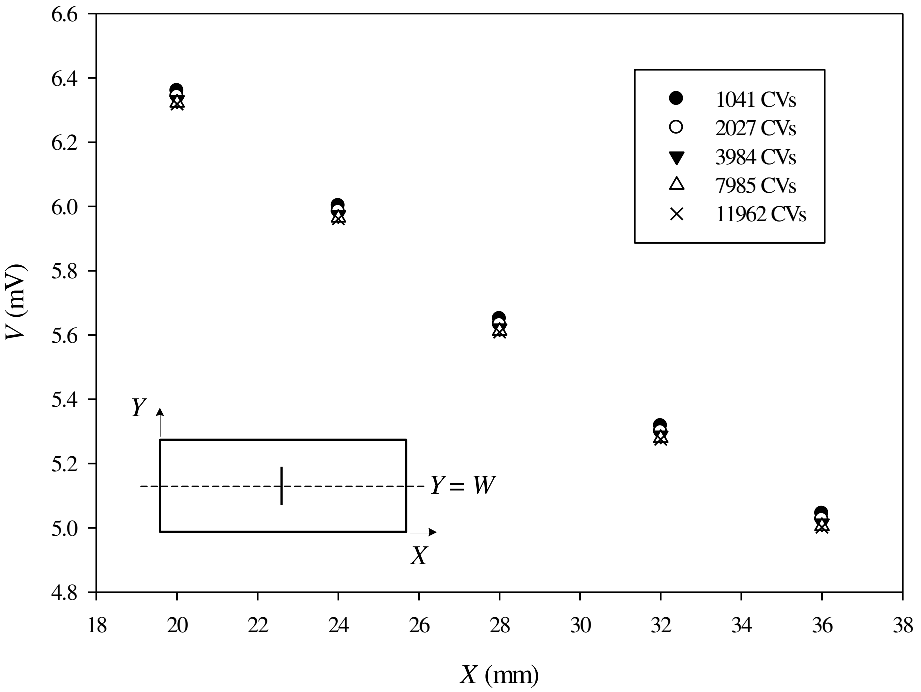

Fig. A.30 Potential results along $Y = W$ in central cracked plane with $a/W = 0.7$

For $a/W = 0.8$, the CV number used is consisted of 1037, 2027, 3976, 7958 and 12018 as shown in Fig. A.31. The potential results along $Y = W$ are also shown in Fig. A.32. By comparing these values of each grid model, the grid model of 7958 CVs can provide the grid independent solution.

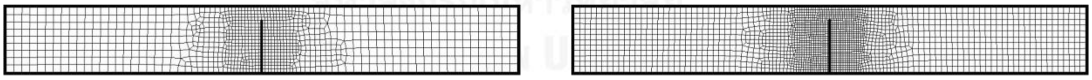

(a) 1037 CVs

(b) 2027 CVs

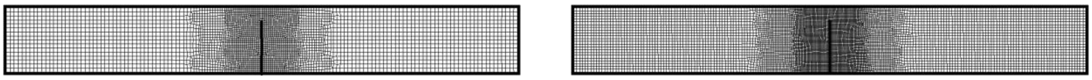

(c) 3976 CVs

(d) 7958 CVs

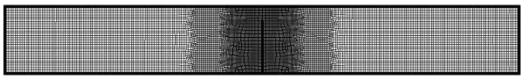

(e) 12018 grids

Fig. A.31 Different number of control volume generating used of central cracked specimen with crack length to specimen width ratio $a/W = 0.8$

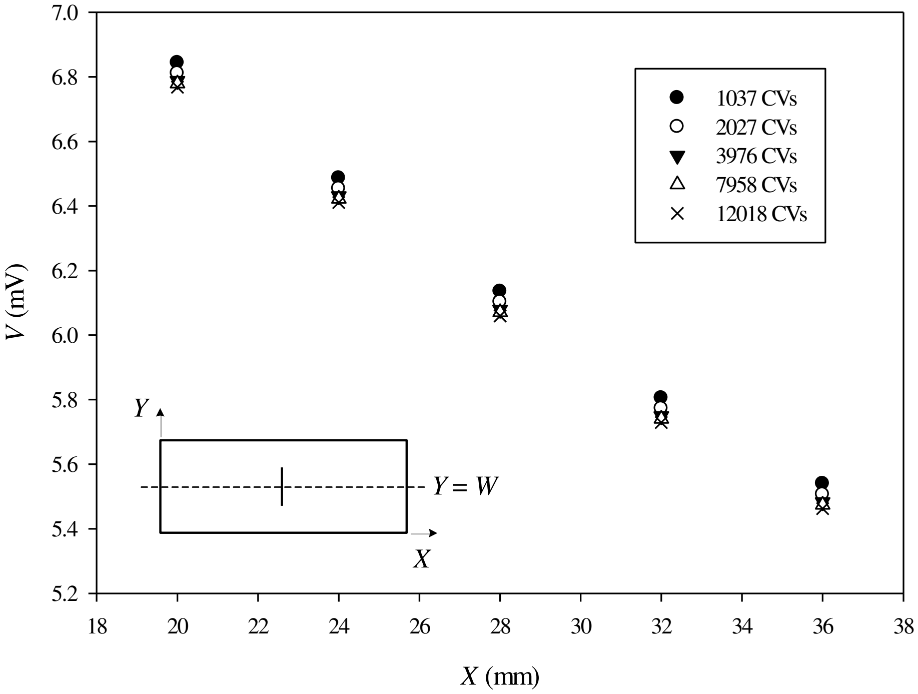

Fig. A.32 Potential results along $Y = W$ in central cracked plane with $a/W = 0.8$

The number of CV used for central cracked specimen with different crack length to specimen width ratio a/W is concluded in Table A.6 to Table A.10. These tables also compare the numerical normalized potential drop across the crack V/V_0 at various calculated position from $y = 4$ to 20 mm with Johnson's solution.

Table A.6 The normalized potential drop (V/V_0) across the central crack compared with analytical solution at potential probe $y = 4$ mm

a/W	No. of CV	V/V_0		Percentage Error
		Johnson Eq.	FVM	
0.1	4024	1.035	1.041	0.603
0.2	4024	1.136	1.148	1.042
0.3	8018	1.298	1.310	0.924
0.4	7990	1.515	1.530	1.012
0.5	8031	1.791	1.810	1.079
0.6	8036	2.140	2.163	1.111
0.7	7985	2.596	2.629	1.299
0.8	7958	3.241	3.296	1.693

Table A.7 The normalized potential drop (V/V_0) across the central crack compared with analytical solution at potential probe $y = 8$ mm

a/W	No. of CV	V/V_0		Percentage Error
		Johnson Eq.	FVM	
0.1	4024	1.012	1.014	0.205
0.2	4024	1.047	1.051	0.399
0.3	8018	1.106	1.110	0.413
0.4	7990	1.192	1.198	0.525
0.5	8031	1.309	1.317	0.643
0.6	8036	1.465	1.476	0.743
0.7	7985	1.679	1.695	0.953
0.8	7958	1.991	2.018	1.349

Table A.8 The normalized potential drop (V/V_0) across the central crack compared with analytical solution at potential probe $y = 12$ mm

a/W	No. of CV	V/V_0		Percentage Error
		Johnson Eq.	FVM	
0.1	4024	1.007	1.008	0.123
0.2	4024	1.028	1.030	0.244
0.3	8018	1.064	1.067	0.262
0.4	7990	1.117	1.121	0.349
0.5	8031	1.190	1.195	0.448
0.6	8036	1.290	1.297	0.543
0.7	7985	1.429	1.439	0.728
0.8	7958	1.634	1.652	1.085

Table A.9 The normalized potential drop (V/V_0) across the central crack compared with analytical solution at potential probe y = 16 mm

a/W	No. of CV	V/V_0		Percentage Error
		Johnson Eq.	FVM	
0.1	4024	1.005	1.006	0.089
0.2	4024	1.020	1.022	0.179
0.3	8018	1.046	1.049	0.196
0.4	7990	1.085	1.088	0.264
0.5	8031	1.139	1.143	0.346
0.6	8036	1.213	1.218	0.429
0.7	7985	1.316	1.324	0.586
0.8	7958	1.470	1.483	0.902

Table A.10 The normalized potential drop (V/V_0) across the central crack compared with analytical solution at potential probe y = 20 mm

a/W	No. of CV	V/V_0		Percentage Error
		Johnson Eq.	FVM	
0.1	4024	1.004	1.005	0.071
0.2	4024	1.016	1.017	0.143
0.3	8018	1.037	1.038	0.157
0.4	7990	1.068	1.070	0.213
0.5	8031	1.111	1.114	0.283
0.6	8036	1.170	1.174	0.354
0.7	7985	1.252	1.258	0.489
0.8	7958	1.374	1.385	0.770

Appendix B

Data of Normalized Potential Across the Crack and the Adjacent Potential Ratio

This appendix shows the data of normalized potential across the crack V_C/V_0 and the adjacent potential ratio V_L/V_R for the inclined edge crack calibration curves in Chapter 6.

The potential measured distance from crack y is 5 mm. Thus, the distance between 2 potential measured probes of V_C, V_L and V_R equals to $2y = 10$ mm. The data of normalized potential across the crack V_C/V_0 at the potential measured distance between 2 measured probes $2y = 10$ mm is shown in Table B.1 while the data of the adjacent potential ratio V_L/V_R at the same potential measured distance is in Table B.2.

Table B.1 The normalized potential drop V/V_0 across the inclined edge crack at potential measured probes distance $2y = 10$ mm

a/W	V_C/V_0					
	$\theta = 7.5°$	$\theta = 15°$	$\theta = 22.5°$	$\theta = 30°$	$\theta = 37.5°$	$\theta = 45°$
0.1	1.0863	1.0903	1.0789	1.0773	1.0628	1.0551
0.2	1.3098	1.3037	1.2879	1.2721	1.2465	1.2174
0.3	1.6316	1.6208	1.5994	1.5718	1.5338	1.4910
0.4	2.0343	2.0182	1.9837	1.9482	1.8987	1.8342
0.5	2.5151	2.4866	2.4438	2.3785	2.3040	2.2231
0.6	3.1252	3.0515	2.9783	2.8814	2.7681	2.6470
0.7	3.8501	3.7632	3.6343	3.4858	3.3077	3.1339
0.8	4.8815	4.7179	4.4917	4.2266	3.9476	3.6755

Table B.2 The adjacent potential ratio V_L/V_R of the inclined edge crack specimen at potential measured probes distance $2y = 10$ mm

a/W	V_L/V_R					
	$\theta = 7.5°$	$\theta = 15°$	$\theta = 22.5°$	$\theta = 30°$	$\theta = 37.5°$	$\theta = 45°$
0.1	1.0032	1.0064	1.0081	1.0117	1.0106	1.0094
0.2	1.0179	1.0353	1.0513	1.0661	1.0733	1.0779
0.3	1.0444	1.0897	1.1357	1.1782	1.2171	1.2502
0.4	1.0777	1.1614	1.2488	1.3442	1.4416	1.5344
0.5	1.1136	1.2412	1.3882	1.5500	1.7333	1.9483
0.6	1.1506	1.3266	1.5385	1.7961	2.1134	2.5229
0.7	1.1846	1.4096	1.6969	2.0708	2.5654	3.2747
0.8	1.2144	1.4869	1.8528	2.3585	3.0942	4.2251

VITA

Mr. Ni-Asri Cheputeh was born on February 8, 1989 in Yala Province, Thailand. He received his bachelor degree in Mechanical Engineering from Kasetsart University in 2011. After graduation, he was employed in the Department of Body Engineering, Toyota Motor Asia Pacific Engineering & Manufacturing, based in Thailand. He continued his education in master degree in the Department of Mechanical Engineering, Faculty of Engineering, Chulalongkorn University in 2012.